

University of Alberta

**A Programmable Pulsed Electromagnetic Field Generation System for
Osteoarthritis Research**

by

Matthew Edward Jahns



A thesis submitted to the Faculty of Graduate Studies and Research in partial fulfillment
of the requirements for the degree of Master of Science

Department of Electrical and Computer Engineering

Edmonton, Alberta

Spring 2008



Library and
Archives Canada

Published Heritage
Branch

395 Wellington Street
Ottawa ON K1A 0N4
Canada

Bibliothèque et
Archives Canada

Direction du
Patrimoine de l'édition

395, rue Wellington
Ottawa ON K1A 0N4
Canada

Your file Votre référence
ISBN: 978-0-494-45826-6
Our file Notre référence
ISBN: 978-0-494-45826-6

NOTICE:

The author has granted a non-exclusive license allowing Library and Archives Canada to reproduce, publish, archive, preserve, conserve, communicate to the public by telecommunication or on the Internet, loan, distribute and sell theses worldwide, for commercial or non-commercial purposes, in microform, paper, electronic and/or any other formats.

The author retains copyright ownership and moral rights in this thesis. Neither the thesis nor substantial extracts from it may be printed or otherwise reproduced without the author's permission.

AVIS:

L'auteur a accordé une licence non exclusive permettant à la Bibliothèque et Archives Canada de reproduire, publier, archiver, sauvegarder, conserver, transmettre au public par télécommunication ou par l'Internet, prêter, distribuer et vendre des thèses partout dans le monde, à des fins commerciales ou autres, sur support microforme, papier, électronique et/ou autres formats.

L'auteur conserve la propriété du droit d'auteur et des droits moraux qui protègent cette thèse. Ni la thèse ni des extraits substantiels de celle-ci ne doivent être imprimés ou autrement reproduits sans son autorisation.

In compliance with the Canadian Privacy Act some supporting forms may have been removed from this thesis.

Conformément à la loi canadienne sur la protection de la vie privée, quelques formulaires secondaires ont été enlevés de cette thèse.

While these forms may be included in the document page count, their removal does not represent any loss of content from the thesis.

Bien que ces formulaires aient inclus dans la pagination, il n'y aura aucun contenu manquant.

■ ■ ■
Canada

ABSTRACT

This thesis examined the development and application of a programmable pulsed electromagnetic field (PEMF) generation system for use in osteoarthritis research. The use of electric and magnetic fields is an active area of research involving the exposure of many cell types. Application towards treatments for osteoarthritis involves the exposure of chondrocytes to regenerate cartilage tissue. Laboratory experiments have demonstrated the potential for PEMF exposure to alter the morphology of *in vitro* cultured human chondrocytes. To assist the future laboratory research, a programmable PEMF generation system has been designed, built and tested to produce a user-specified ramp magnetic field. An electromagnetic model of a coil set was developed to provide a theoretical basis for this proposed system. Lastly, the programmable PEMF generation system was applied to the testing of calcium ion resonance in transmembrane channels and its regulation of chondrocyte morphology.

ACKNOWLEDGEMENT

The completion of this thesis would not be possible without the support and help from many people of whom I am thankful.

I owe a great deal of thanks to my co-supervisor Dr. Edmond Lou for his guidance and expertise throughout the work of this thesis.

I also thank my other co-supervisor Dr. Nelson Durdle for his support throughout the completion of this degree.

I extend thanks to the Glenrose Research Hospital for providing a research lab. Their collaboration with this research is greatly appreciated.

I thank Dr. John Cinats for providing this research project with cartilage specimens.

I also thank Dr. Keith Bagnall's laboratory for assistance in the chondrocyte experiments. In particular, I would like to thank Randy, David, Charlie and Henry who prepared the chondrocyte cultures and made the execution of my experiments possible.

The funding provided by the University of Alberta, Natural Sciences and Engineering Research Council of Canada (NSERC), iCORE, and the Edmonton Orthopaedic Research Society made this work financially possible.

I am indebted to my family and friends for their support and motivation throughout this research. Without their presence during the hard times, completion of this thesis would not be possible.

Lastly, I owe the ultimate thanks to God for his guidance at all times throughout the completion of this thesis.

TABLE OF CONTENTS

<i>Chapter 1</i>	1
1. Introduction.....	1
1.1. Osteoarthritis.....	1
1.2. Application and Significance of a Programmable Pulsed Electromagnetic Field Generation System to Osteoarthritis Research.....	2
1.3. Objectives.....	3
1.4. Scope of Work.....	3
1.5. Thesis Overview.....	5
 <i>Chapter 2</i>	 7
2. Literature Review.....	7
2.1. Anatomy.....	7
2.1.1. Joints.....	7
2.1.2. Cartilage.....	8
2.1.3. Chondrocytes.....	11
2.2. Cartilage Repair and Osteoarthritis.....	14
2.2.1. Natural Repair of Cartilage.....	14
2.2.2. Treatments for Osteoarthritis.....	16
2.3. Cellular Exposure to Electric and Magnetic Fields.....	18
2.3.1. Exposure to DC Electric Fields.....	18
2.3.2. Exposure to DC Magnetic Fields.....	21
2.3.3. Exposure to Electromagnetic Fields.....	23
2.3.3.1. Exposure to Pulsed Electric Fields.....	23
2.3.3.2. Exposure to Pulsed Magnetic Fields.....	25
2.4. Theory of Ion Resonance.....	30
 <i>Chapter 3</i>	 33
3. Effect of PEMF Exposure on Chondrocyte Morphology.....	33
3.1. Objectives.....	33
3.2. Materials and Methods.....	33
3.2.1. Chondrocyte Culture.....	33
3.2.2. Experimental Setup.....	34
3.3. Results.....	37
3.4. Discussion.....	42
 <i>Chapter 4</i>	 45
4. Electromagnetic Modelling.....	45
4.1. On-Axis Magnetic Field Produced at the Midpoint Between a Coil Pair.....	45
4.2. Off-Axis Magnetic Field Produced by Two Coils.....	49
4.3. Electric Field Induced by On-Axis Magnetic Field Model.....	56
4.4. Electric Field Induced by Off-Axis Magnetic Field Model.....	57

Chapter 5.....	58
5. System Design.....	58
5.1. Literature Review.....	58
5.2. System Overview.....	60
5.3. Coil Set.....	61
5.3.1. Magnetic Field Limitation.....	61
5.3.2. Simulation of Current Flow through a Coil Set.....	64
5.4. Coil Driver.....	69
5.4.1. Power Management Module.....	70
5.4.2. Voltage-to-Current Conversion.....	72
5.5. Programmable Waveform Generator.....	75
5.5.1. Hardware.....	75
5.5.1.1. USB Interface.....	76
5.5.1.2. Power Regulation.....	77
5.5.1.3. Microcontroller.....	79
5.5.1.4. AC Signal Generation Circuit.....	80
5.5.1.5. DC Signal Generation Circuit.....	84
5.5.1.6. Dual Channel Voltage Output.....	86
5.5.2. Firmware.....	87
5.5.2.1. Main Program Initialization.....	87
5.5.2.2. Connected to USB Subprogram.....	88
5.5.2.2.1. EEPROM Access Module.....	89
5.5.2.2.2. USART Communication Module.....	90
5.5.2.2.3. Calculate Timer Values Module.....	92
5.5.2.2.4. Calculate Resister Values Module.....	95
5.5.2.3. Disconnected from USB Subprogram.....	99
5.5.2.3.1. System Initialization Module.....	99
5.5.2.3.2. Waveform Generation Module.....	102
5.5.2.4. Interrupt Service Routine.....	105
5.6. Magnetic Field Sensor.....	106
5.7. Current Consumption Analysis.....	108
5.7.1. Programmable Waveform Generator.....	108
5.7.2. Coil Driver.....	109
5.8. System Verification.....	110
5.8.1. Coil Driver.....	110
5.8.2. Programmable Waveform Generator.....	111
5.8.2.1. Verification of Computer Interface.....	111
5.8.2.2. Verification of 16-bit Timer.....	112
5.8.2.3. Implemented Circuit Conditions.....	113

<i>Chapter 6</i>	114
6. System Testing and Results.....	114
6.1. Objectives.....	114
6.2. Methodology	114
6.2.1. Calibration of AC Waveform.....	114
6.2.2. Verification of AC Field Operating Range	117
6.2.3. Verification of DC Field Operating Range	118
6.3. Results	119
6.3.1. AC Field Operating Range.....	119
6.3.2. DC Field Operating Range.....	124
6.4. Discussion	125
 <i>Chapter 7</i>	 131
7. Application of the Programmable PEMF Generation System	131
7.1. Objectives.....	131
7.2. Methodology	131
7.2.1. Previous Laboratory Evidence	131
7.2.2. Experimental Setup	132
7.3. Results.....	134
7.4. Conclusion.....	138
 <i>Chapter 8</i>	 139
8. Conclusion and Future Recommendations.....	139
8.1. Conclusion.....	139
8.2. Future Recommendations.....	142
 <i>References</i>	 145
 <i>Appendix A: Coil Driver Schematics</i>	 154
 <i>Appendix B: Programmable Waveform Generator Schematics</i>	 156
 <i>Appendix C: Magnetic Field Sensor Schematics</i>	 161

LIST OF TABLES

Table 3-1: PEMF settings and results for part one and part two trials performed on cultured human chondrocytes.....	37
Table 3-2: Morphological assessment of cultured human chondrocytes exposed to PEMFs	41
Table 3-3: Change in surface contact area with a culture dish for cultured human chondrocytes exposed to PEMFs	42
Table 5-1: Categorized listing of the settings stored within the EEPROM	89
Table 5-2: Valid range for the five PEMF user settings	91
Table 5-3: Effect of prescaler on maximum timer count and resolution	93
Table 5-4: Configuration of the timer registers for mode 0 and mode 1	94
Table 5-5: Programmable waveform generator temporal settings for the four timer prescaler modes	113
Table 6-1: Experimental results before calibration using pulse widths of 35msec and 15msec.....	115
Table 6-2: Experimental results after calibration using a pulse width of 35msec	116
Table 6-3: Experimental results after calibration using a pulse width of 15msec	116
Table 6-4: Analysis of experimental waveform magnitude configured for an AC magnetic field setting of $0.5mT_{PP}$	121
Table 6-5: Analysis of experimental waveform magnitude configured for an AC magnetic field setting of $1.5mT_{PP}$	121
Table 6-6: Analysis of experimental waveform magnitude configured for an AC magnetic field setting of $2.5mT_{PP}$	121
Table 6-7: Analysis of ramp and reset times for an experimental magnetic field configured with an AC magnitude of $0.5mT_{PP}$	122
Table 6-8: Analysis of ramp and reset times for an experimental magnetic field configured with an AC magnitude of $1.5mT_{PP}$	122
Table 6-9: Analysis of ramp and reset times for an experimental magnetic field configured with an AC magnitude of $2.5mT_{PP}$	122

Table 6-10: Experimental results for the duty cycle and pulse train verification using the shortest and longest PEMF waveforms	123
Table 6-11: Experimental results for the DC bias produced by the programmable PEMF generation system during the off-time portion of the waveform duty cycle.....	124
Table 6-12: Experimental results for the DC bias produced by the programmable PEMF generation system during the active portion of the waveform duty cycle	125
Table 7-1: Desired magnetic field settings for the investigation of ion parametric resonance.....	133
Table 7-2: Implemented user settings for the programmable PEMF generation system to achieve experimental conditions A, B and C	135

LIST OF FIGURES

Figure 1-1: A comparison of (a) healthy and (b) osteoarthritic cartilage tissue prepared with trichrome staining.....	1
Figure 2-1: Composition of a human joint.....	8
Figure 3-1: Placement of cultured human chondrocytes in the coil set.	34
Figure 3-2: Theoretical models of the (a) magnetic and (b) electric fields in the plane of the dish, taken at the midpoint separation distance between the small coil pair, for a $3.14\text{mT}_{\text{peak}}$, 100Hz exposure.	35
Figure 3-3: Example of ramp magnetic field used in experimental trials.....	36
Figure 3-4: Microscope images of chondrocytes in part one control dish (no PEMF) taken (a) before and (b) after a six hour period	38
Figure 3-5: Microscope images of chondrocytes in experimental dish (PEMF exposure) for (a) experimental trial A taken after a six hour period and (b) experimental trial C taken after a three hour period.....	39
Figure 3-6: Microscope images of chondrocytes in part two control dish (no PEMF) taken (a) before and (b) after a six hour period	40
Figure 3-7: Microscope images of chondrocytes in experimental dish (PEMF exposure) for experimental trial G taken after a six hour period	40
Figure 4-1: A single coil carrying current I, with specified on-axis point P.....	45
Figure 4-2: A coil pair carrying current I, with specified on-axis point P	47
Figure 4-3: Off-axis magnetic field modeling of a single coil.....	50
Figure 4-4: Off-axis magnetic field modeling of a coil pair	53
Figure 4-5: Theoretical magnetic field strength throughout a vertical plane of a coil pair	54
Figure 5-1: Block diagram of the programmable PEMF generation system	60
Figure 5-2: Arrangement of the coil set with the culture dish	62
Figure 5-3: Magnetic field in the plane of the culture dish for the (a) small and (b) large coil set	63

Figure 5-4: Circuit model of the coil driver connected to a coil set.....	64
Figure 5-5: Coil simulation using a 35msec ramp pulse width for (a) the small coil and (b) the large coil	66
Figure 5-6: Coil simulation using a 1msec ramp pulse width for (a) the small coil and (b) the large coil	67
Figure 5-7: The coil driver	69
Figure 5-8: Overview of the coil driver power management module	70
Figure 5-9: Overview of the coil driver voltage-to-current conversion circuit.....	72
Figure 5-10: The programmable waveform generator	75
Figure 5-11: Block diagram of the programmable waveform generator	75
Figure 5-12: Overview of programmable waveform generator power regulation.....	77
Figure 5-13: Overview of programmable waveform generator microcontroller	79
Figure 5-14: Overview of programmable waveform generator AC signal generation circuit.....	80
Figure 5-15: Overview of AC signal generation circuit resistance selection.....	83
Figure 5-16: Overview of DC signal generation circuit.....	84
Figure 5-17: Comparison of (a) the original ramp waveform and (b) the DC equalized waveform.....	85
Figure 5-18: Overview of main program firmware.....	87
Figure 5-19: Overview of “Connected to USB” subprogram firmware.....	88
Figure 5-20: Overview of “Disconnected from USB” subprogram firmware	99
Figure 5-21: Overview of the “Waveform Generation” subroutine.....	102
Figure 5-22: Overview of the “Waveform Deactivated” subroutine	103
Figure 5-23: Overview of the “Waveform Activated” subroutine.....	104
Figure 5-24: Overview of the “Pulse Train Regulation” subroutine.....	104

Figure 6-1: Magnetic waveform measurements for a 100% duty cycle, 35msec pulse width signal configured for an AC magnetic field strength of (a) 0.5mT _{PP} and (b) 2.5mT _{PP}	117
Figure 6-2: Experimental magnetic field waveform configured for a 2.5mT _{PP} AC magnetic field with a 1msec pulse width and 100% duty cycle.....	120
Figure 6-3: Magnetic field waveforms of (a) the shortest pulse train and (b) the longest pulse train	123
Figure 6-4: Magnetic waveform measurement showing DC bias during both the active and off-time portions of the waveform duty cycle.....	125
Figure 6-5: AC voltage error of the programmable waveform generator versus pulse width.....	127
Figure 6-6: AC magnetic field error by the coil set versus pulse width.....	128
Figure 7-1: Microscope pictures of the chondrocytes prior to PEMF exposure for (a) the control dish and (b) the experimental dish.....	135
Figure 7-2: Microscope pictures of the chondrocytes after three hours of PEMF exposure for (a) the control dish and (b) the experimental dish.....	136
Figure 7-3: Microscope pictures of the chondrocytes after six hours of PEMF exposure for (a) the control dish and (b) the experimental dish.....	137
Figure 7-4: Microscope pictures of the chondrocytes twenty-four hours after removal from the PEMF exposure for (a) the control dish and (b) the experimental dish	137

LIST OF ABBREVIATIONS

A	Ampere
AC	Alternating Current
Ahr	Ampere-Hour
ATP	Adenosine Triphosphate
DC	Direct Current
F	Farad
H	Henry
hr	Hour
Hz	Hertz
IC	Integrated Circuit
I/O	Input/Output
LC	Inductor-Capacitor
LED	Light Emitting Diode
Ω	Ohm
PEMF	Pulsed Electromagnetic Field
PES	Pulsed Electrical Stimulation
PP	Peak-to-Peak
PST	Pulsed Signal Therapy
RMS	Root-Mean-Square
sec	Second
SNR	Signal-to-Noise Ratio
SPI	Serial Peripheral Interface
T	Tesla
USB	Universal Serial Bus
V	Volt
W	Watt

Chapter 1

1. Introduction

1.1. Osteoarthritis

Osteoarthritis is a joint disease where the surface layer of articular cartilage breaks down and wears away. As the disease progresses, joints may lose their normal shape, develop bone spurs and bits of bone or cartilage can break off and float within the joint space. As a result, bones rub together resulting in pain, swelling and loss of motion in the joint. Images of healthy (figure 1-1a) and osteoarthritic (figure 1-1b) cartilage tissue prepared with trichrome staining emphasise these characteristics. Unlike other forms of arthritis, osteoarthritis only affects joints and not internal organs [1]. According to Canadian statistics, osteoarthritis affects 1 in 10 Canadians [2]. In the United States, 46 million people are affected with some form of arthritis [3]. Of those cases, osteoarthritis is the most prevalent affecting almost 21 million [4]. It is estimated that by 2030 there will be 65 million Americans affected with arthritis [5]. Generally, osteoarthritis is more common in women over the age of 45 affecting common target areas such as the hands, knees, hip or spine [1]. Osteoarthritis is the leading cause of disability in Americans [6]. Therefore, it is not surprising that osteoarthritis causes an annual financial burden of \$86.2 billion to the United States economy [7].

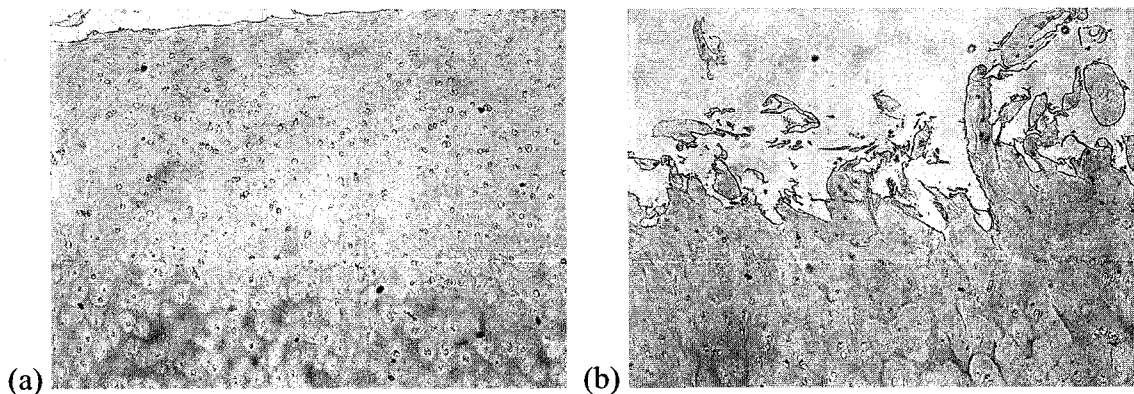


Figure 1-1: A comparison of (a) healthy and (b) osteoarthritic cartilage tissue prepared with trichrome staining.

1.2. Application and Significance of a Programmable Pulsed Electromagnetic Field Generation System to Osteoarthritis Research

Pulsed electromagnetic field (PEMF) exposure has been used to treat various musculoskeletal disorders. Since approval was obtained by the Food and Drug Administration in 1979, PEMF exposure has treated non-union bone fractures with an average success rate of 75% [8]. PEMFs have recently been used to treat patients with osteoarthritis. Treatment centers have been developed worldwide that utilize a methodology known as Pulsed Signal Therapy (PST). The theory proposes that electromagnetic fields act as the signal that triggers regenerative processes within cartilage tissue, thereby stimulating chondrocytes to produce the components of cartilage and repairing damaged tissue [9,10]. Whereas the above treatments apply a pulsed magnetic stimulation using a coil system, other clinical systems have used implanted electrodes to create a pulsed electrical stimulation. Patients have reported improvements in knee pain, function, flexion and active daily living [11,12]. However, the use of electromagnetic fields is the preferred method of treatment since it is non-invasive. As a result, issues regarding the surgical implantation and removal of electrodes [13], limited stimulatory tissue area [14] and electrode corrosion [15] can be avoided during treatment sessions. Although the results from these clinical trials are promising, the mechanism by which PEMF exposure alters cartilage tissue and the repair of injury still remains largely unknown.

Since the mechanisms by which PEMF exposure remedies osteoarthritis are not understood, there exists the need for further research. This will be achieved through a series of studies exposing *in vitro* cultured human chondrocytes to PEMFs. Understanding the effect of PEMF exposure on chondrocyte behaviour is the first step in modelling the repair process of cartilage tissue.

1.3. Objectives

There are two objectives to the work performed in this thesis:

The primary objective of this thesis is to design, build, and test a programmable PEMF generation system.

The secondary objective of this thesis is to demonstrate the application of the programmable PEMF generation system on *in vitro* cultured human chondrocytes. This application is demonstrated through the investigation of calcium ion resonance in transmembrane channels, as a possible mechanism used by PEMFs to alter chondrocyte morphology.

1.4. Scope of Work

The primary objective is to design, build, and test a programmable PEMF generation system. Several requirements must be met in order to meet this objective.

In the laboratory, electromagnetic field generation was originally a manual process using an extensive array of expensive electrical components. Configuration of these individual components required knowledge of an electrical and electronics background. To ease the task of generating electromagnetic fields, a programmable PEMF generation system is proposed by this thesis. This calibrated instrument can generate ramping magnetic fields with a configurable peak-to-peak ramp magnetic field strength, magnetic field bias, ramp pulse duration, pulse train length, and duty cycle. Use of this system reduces the amount of equipment and automates the process of generating electromagnetic fields for the *in vitro* cultured human chondrocyte exposure studies performed in the laboratory. As a result, the biologist and lab technician can focus on the chondrocyte tests relevant to their study, rather than how the PEMF is developed.

From a review of the literature, the following specifications were determined for the programmable PEMF generation system. The system will allow the user to configure

both the magnitude and timing aspects of the overall ramp magnetic field. The system can generate an alternating current (AC) magnetic field ranging from $0.5\text{mT}_{\text{peak-to-peak (PP)}}$ to 2.5mT_{PP} . The user can add a direct current (DC) magnetic field ranging from 0mT to 1.25mT . The width of a single ramp pulse can range from 1msec to 35msec . The waveform can either be a continuous pulse train or be divided into packets ranging from 1 to 25 pulses. The duty cycle of this pulse train can range from 10% to 95%.

The design of this system requires both hardware and firmware strategies. A microcontroller is used to control the operation of the hardware components required to generate the desired waveform. Custom firmware is required to convert the desired PEMF configuration, as specified by the user, into the settings for the hardware components. It is these hardware components that physically produce the signal sent to the coil set for the generation of PEMFs.

Lastly, the specified operating range must be verified once the system has been fabricated. A comprehensive testing procedure will determine the accuracy of the system across its specified operating range. The verification of this system has a process of checks and balances. There must be agreement between theoretical values, the voltage output of the programmable waveform generator, and the magnetic field output of the coil set.

A secondary objective is to demonstrate the application of the system for exposing *in vitro* cultured human chondrocytes to PEMFs. Prior laboratory results indicated that specific PEMF exposure conditions are required to alter chondrocyte morphology. The application of this system will investigate a hypothesis regarding ion resonance in transmembrane channels, specifically the calcium ion, as a mechanism used by PEMFs to alter the morphology of chondrocytes.

Three PEMF conditions are used to test the hypothesis of calcium ion resonance in transmembrane channels according to the following procedure: (1) a resonant condition for the calcium ion is applied to the chondrocytes, (2) two different non-resonant

conditions are applied to the chondrocytes. These two non-resonant conditions test the requirements for the pulse width and magnetic ramp magnitude respectively.

Although the requirements have been stated, there are also several limitations to the fulfillment of the secondary thesis objective. With regards to the investigation of ion resonance, there is an operating window in which resonance occurs. The intent of this preliminary investigation is to determine if the mechanism of calcium ion resonance regulates chondrocyte morphology. A more intensive investigation will look specifically at the width of the operating window that promotes resonance. This operating window could be influenced by the AC magnetic field strength, DC magnetic field strength, duration of the ramp pulse, duty cycle of the waveform, and length of the stimulating pulse train.

1.5. Thesis Overview

This thesis consists of eight chapters. These chapters encompass a literature review, a discussion of PEMF exposure affecting chondrocyte morphology, the development of a programmable PEMF generation system, and its application to osteoarthritis research.

Chapter 1 provides the introduction to this work. Awareness of the problems associated with osteoarthritis justifies the development of research to resolve these issues. The introduction also justifies the development of a programmable PEMF generation system to assist the laboratory's research on *in vitro* cultured human chondrocyte exposure to PEMFs. As well, the objective and scope of the work in this thesis are presented.

Chapter 2 provides a literature review of topics relevant to this thesis. Biological background concerning joints, cartilage and chondrocytes is provided. This knowledge is further expanded with an overview of the current treatments available for patients with osteoarthritis. The chapter then discusses the studies performed by other research groups exposing cells, mainly chondrocytes, to static electric, static magnetic, and electromagnetic fields respectively. Lastly the theory of ion resonance in transmembrane channels is introduced as a mechanism to control chondrocyte behaviour.

Chapter 3 discusses previous laboratory results of exposing *in vitro* cultured human chondrocytes to electromagnetic fields. These served as motivation for the development of a programmable PEMF generation system for the execution of further studies. These results demonstrated that PEMF exposure could alter the morphology of chondrocytes.

Chapter 4 provides an overview of electromagnetic theory. A theoretical model is presented for the magnetic and electric field produced by a coil pair.

Chapter 5 describes the design of a programmable PEMF generation system. This process includes the selection of hardware for the programmable waveform generator, coil driver, coil set and magnetic field sensor. It also provides an outline of the firmware written for the system.

Chapter 6 describes the testing and verification of the programmable PEMF generation system. The test results are used to verify the voltage signal from the programmable waveform generator and the magnetic field produced by the coil set.

Chapter 7 demonstrates the application of this programmable PEMF generation system for exposing *in vitro* cultured human chondrocytes to PEMFs. This investigation tests a hypothesis of calcium ion resonance in transmembrane channels as a possible mechanism by which PEMF exposure affects chondrocyte morphology.

Chapter 8 is a summary of the thesis work. It provides concluding statements on the success of the programmable PEMF generation system and its application to *in vitro* cultured human chondrocyte exposure studies. Future recommendations are made to discuss the next steps of this research.

Chapter 2

2. Literature Review

2.1. Anatomy

The long-term objective of this research is to develop a non-invasive treatment for osteoarthritis using exposure to PEMFs. This treatment would target the joints of patients affected with osteoarthritis. As a result, an understanding of the physiology of a common joint is required for the awareness of issues that may immerge in future experimentation. Hence this chapter has been written to provide an overview of joints, cartilage, and chondrocytes. There are shortcomings in the natural repair of cartilage that lead to the development of osteoarthritis. The current treatments available for osteoarthritis only reduce the severity of the symptoms; hence a novel treatment that addresses the repair of cartilage is of significant importance to the advancement of medicine.

2.1.1. Joints

The purpose of a joint is to allow smooth and controlled movement between bones and to absorb the shock from repetitive movements. As shown in figure 2-1, there are five basic components to a joint: bone, cartilage, joint capsule or synovium, synovial fluid, and other connective tissues (ligaments, tendons and muscles) [1]. The joint capsule is a tough membrane sac that contains all the components of the joint. On the inside surface of the joint capsule is a thin membrane called the synovium. Within this capsule is synovial fluid that lubricates the joint. Ligaments, tendons and muscles stabilize the joint, allowing it to bend and move. As mentioned, osteoarthritis targets articular cartilage which is the hard and slippery coating on the end of each bone. The degradation of cartilage from osteoarthritis impedes the smooth movement between the bones, compromising the functionality of the joint.

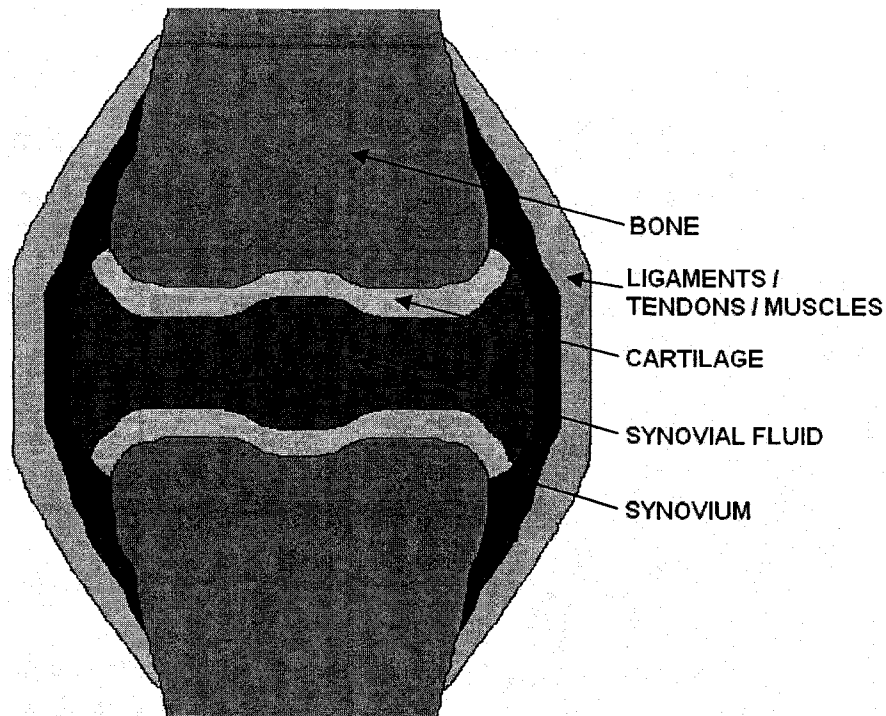


Figure 2-1: Composition of a human joint

2.1.2. Cartilage

Articular cartilage, also known as hyaline cartilage, covers the ends of all bones in synovial joints. It is characterized by outstanding lubricating properties and a low coefficient of friction. Cartilage is different from other types of tissue because it does not have intrinsic blood vessels, nerves or lymph vessels. The lack of a blood supply along with a limited number of chondrocytes impedes the repair capability of cartilage tissue [16].

There are two distinct components to the structure of cartilage. The first component is a fluid composed of water and electrolytes. The second is a solid composed of collagen fibrils, proteoglycans and other glycoproteins. According to weight, the composition of articular cartilage is 65-80% water, 15-25% type II collagen, and 5-10% proteoglycans [17]. Collagen is a fibrous protein and proteoglycan is a combination of protein and glycosaminoglycan (sugar); they interweave to form the cartilage matrix [1]. Within this matrix is a limited supply of chondrocytes, less than 10% of cartilage volume, that manufacture collagen and proteoglycans [16].

The organization of cartilage matrix varies according to three depth zones. In the superficial zone, the cartilage contains fine collagen fibrils arranged parallel to the surface. In the mid-zone, the collagen fibrils have random arrangement. Lastly, in the deep zone the collagen fibrils are aligned perpendicular to the articulating surface [18,19]. The typical thickness of cartilage, such as on the human patella, is 1.5mm. As subjects mature the thickness of their cartilage decreases, along with an increase in collagen content and decrease in proteoglycan concentration [16].

During cartilage loading proteoglycans are under tension as they attempt to restrain water flow. A property of proteoglycans is that they are hydrophilic; repelling each other if forced together. There is also an electrostatic attraction between the positive charges along the collagen fibrils and the negative charges of the glycosaminoglycans. The compressive aggregate modulus for human articular cartilage correlates inversely with water content and directly with proteoglycan content [16]. Early signs of osteoarthritis are increased tissue hydration and loss of proteoglycans [17]. When cartilage tissue is placed under compressive stress, fluid flows out of the tissue. When the stress is removed, the fluid returns. This synovial fluid contains a mixture of ions, both positive and negative. The compression of the tissue causes a separation of charge between these free ions in the synovial fluid and the fixed negative charges on the proteoglycans; hence the development of an electric field [20,21]. It is believed that the presence of this electromagnetic field in cartilage tissue stimulates chondrocyte synthesis of matrix components [22].

An understanding of these naturally occurring electric fields requires the development of cartilage models. Lai et al. [23,24] proposed a cartilage model considering both the chondrocyte and the extracellular matrix according to a triphasic theory. Their model determines the electric field in and around a chondrocyte inside a layer of cartilage tissue in one-dimensional confined compression. The triphasic theory computes the current density at any point as the vector sum of the convection, diffusion, and conduction currents. Convection current is driven by the pressure gradient, causing fluid flow that

convects cations and anions. Diffusion current is driven by the concentration gradient between cations and anions moving at different speeds and directions. Lastly, conduction current is driven by the non-zero electric potential gradient, causing the movement of ions. The presence of these three different currents induces two types of potentials. A “streaming potential” or fluid flow within charged tissue is caused by a pressure gradient. On the other hand, a diffusion potential is caused by a concentration gradient of the fixed charges within the tissue; either strain-induced or naturally occurring. Since they have opposite polarity, these two potentials compete against each other [17]. Depending upon the loading conditions, they may be of the same order of magnitude. Hence the resulting net potential will ultimately affect the generation of electric fields within cartilage.

As cartilage ages, changes occur to cellularity, glycosaminoglycans and proteoglycans. Chondrocyte death occurs in many adult permanent cartilages, causing them to be less cellular than immature tissues. However, changes in cellularity depend on the location of the cartilage in the body and the probability for the development of fibrillation [25]. For example, cartilage from the femoral head showed as much as a 35% decrease in cellularity over a 30-100 year period [26], while no changes were noted in cartilage from the humeral head [25,27]. Although there is little reduction in the total glycosaminoglycan content of normal articular cartilage during adult life [18], the proportions of glycosaminoglycans does vary. The majority of changes occur in the deep zone of the cartilage where keratansulphate content will change from very low at birth to as much as 55% of total glycosaminoglycan in adults [28].

2.1.3. Chondrocytes

The chondrocytes are the maintenance cells responsible for the development of healthy cartilage. Although the cell boundaries are difficult to determine *in situ*, the diameter of chondrocytes in articular cartilage ranges from 10 μ m to 40 μ m [18,29,30]. The physical characteristics of chondrocytes are largely dependant on factors such as the type of cartilage, the position of the cell within the tissue, tissue cellularity, and the age of the tissue [18].

The morphology of chondrocytes can be characterized according to the three depth zones of articular cartilage. The superficial zone of articular cartilage is located at the surface. Here, the cells are flattened, discoidal or spindle shaped. Their long axes are parallel to the joint surface and aligned with the collagen fibrils [18,19]. Chondrocytes in the superficial zone have many more vesicles, than deeper cells, used for the uptake of synovial fluid rich in nutrients [31]. Chondrocytes in this region are subject to greater levels of cell deformation, requiring a denser cytoskeleton to maintain structural stability [32]. In the mid zone, the cells are more rounded, with random distribution through the tissue. In the deep zone, the chondrocytes form columns with the collagen fibrils that are perpendicular to the joint surface. Notably, the size of chondrocytes is larger in the deeper zones than at the articular surface [18,19].

As chondrocytes mature, they experience an increase in size [33], accompanied by a decrease in their density within the cartilage sample [34]. Chondrocytes may also possess a single cilium, but its presence becomes less frequent with age [18]. Since chondrocytes are considered to be non-motile, the cilium could possibly function as a chemoreceptor [34].

In situ chondrocytes of the human tibial plateau cartilage have been analyzed using confocal scanning laser microscopy. Approximately 40% of chondrocytes demonstrated processes up to 20 μ m long [35] and the majority of cells within all cartilage zones had fine cytoplasmic processes of varying dimension [19]. Occasionally, chondrocytes had a

relatively smooth membrane surface, but these cases were limited to 10% of the population. Interestingly, chondrocytes located in the superficial zone of degenerate cartilage possessed relatively long processes. Although the functional importance of cytoplasmic processes is unclear, they appear to develop into defects of the pericellular matrix. Since chondrocytes in damaged tissue possess longer processes, this may make them more vulnerable to mechanical stresses exerted on cartilage [19]. Increased chondrocyte death is typical in cartilage samples affected by osteoarthritis [18].

Like other types of biological cells, chondrocytes possess a nucleus, various tubular and membranous organelles, as well as glycogen and lipid droplets.

The cytoplasm of chondrocytes contains different types of tubules and filaments: centrioles, microtubules and microfilaments and intermediate filaments. Immature chondrocytes possess either one or two centrioles, due to their relatively high mitotic index. However when mitosis ceases in adult chondrocytes, the centrioles are absent [36]. Microtubules form a loose mesh spanning throughout the cytoplasm [32]. They are found in immature cartilage cells, and occasionally in adult cells as short lengths [37,38]. They play a role in the maintenance and regulation of cell shape, as well as intracellular organization and the movement of materials. Since microtubules are important to the process of collagen secretion, this may explain why they are scarce in adult cells [18]. Actin microfilaments are localized just inside the cell membrane. This network may provide structural protection to the chondrocyte against shear stresses present in cartilage tissue [39]. Although they provide structural rigidity, they are considered a sign of cell deterioration when present in large quantities throughout the cytoplasm [40]. Intermediate filaments are organized in a tighter mesh than microfilaments and span the extent of the cytoplasm from outer membrane to the nucleus [32]. They are believed to contribute to intracellular messenger ribonucleic acid (mRNA) transport as well as the mechanical signal transduction system in chondrocytes [41]. This idea is supported by studies showing that changes to cell morphology also deformed the nucleus through these intermediate filaments, thereby altering the production of proteoglycans [42].

Chondrocytes possess four membranous organelles: endoplasmic reticulum (ER), Golgi complex, lysosomes and mitochondria. The presence of a granular ER indicates that the cell has rich protein synthetic activity. Its outer surface is covered with ribosomes that contain RNA and proteins to produce polypeptide chains. These polypeptide chains are sent to the Golgi apparatus where the completion of polysaccharide synthesis occurs. This entire process is accentuated in the chondrocyte since it is important for the production of proteoglycans. The Golgi apparatus also functions to package materials for secretion by the chondrocyte and to produce lysosomes. Lysosomes are vesicles containing degradative enzymes. Although used in cell maintenance, in the case of chondrocytes, lysosomes may be important to the normal degradation and turnover of the cartilage matrix [18]. The mitochondria are the powerhouse of the chondrocyte responsible for the production of adenosine triphosphate (ATP) used to drive chemical reactions. As chondrocytes age, the increasingly poor development of their mitochondria leads to the low respiratory activity that is characteristic of ageing cartilage [18,43].

The cytoplasm of chondrocytes also possesses inclusions such as glycogen and lipid. Glycogen is abundant in chondrocytes, playing a possible role as a raw material for matrix synthesis [44]. Chondrocytes also usually contain one or more lipid droplets. The amount varies with the type and age of cartilage and the position of the cell in the tissue [45,46]; being most prominent in the chondrocytes in the middle zone of articular cartilage [18]. It is not known why lipids are so prominent in chondrocytes, where the lipid droplets can have diameters up to 10 μ m [18].

2.2. Cartilage Repair and Osteoarthritis

2.2.1. Natural Repair of Cartilage

Articular cartilage has a very limited capacity for repair due to the lack of a blood supply and a limited number of chondrocytes within the tissue. Injury to cartilage can result from a single traumatic load or the accumulation of microtrauma over an extended period of time [16]. Due to the metabolically inert nature of the collagen network, the tensile stress applied to the surface of cartilage may rupture this network. The failure point could be classified as either abnormally high stresses acting on normal cartilage or normal stresses acting on defective cartilage [18].

Extrinsic processes are vital to the repair of discrete cartilage lesions. These lesions can be either partial or full thickness defects. Partial lesions are restricted within the confines of cartilage tissue, thereby restricting access to blood-bone cells, macrophages or mesenchymal stem cells located within the bone-marrow. Full thickness lesions penetrate to the subchondral bone marrow allowing access to cells residing in the bone marrow [47]. Although partial lesions do not initiate a repair process, full thickness lesions will develop a repair tissue lasting for six to twelve months before degeneration [47,48]. Even though some good results can be obtained [49], often lesions fail to heal and will enlarge with time [47].

Spontaneous repair occurs in full thickness cartilage lesions, despite an end result of degeneration. The repair begins in the first 48 hours, by developing a fibrin clot organized with parallel strands across the wound. Within five days, mesenchymal cells penetrate this fibrin clot, differentiate into fibroblasts and replace it with collagen fibres. After two weeks, the fibroblasts differentiate into chondrocytes and lay down a proteoglycan rich extracellular matrix. Although after eight weeks this matrix resembles cartilage, it is mostly fibrous in nature, due to the presence of type I collagen, and eventually shows signs of degeneration after 48 weeks. It is believed that this

degeneration occurs because of a lack of integration between the repair and native articular cartilage [47,48].

Cartilage repair following acute trauma is believed to be an intrinsic process by which the chondrocytes repair the tissue. Although ineffective in advanced lesions, intrinsic cartilage repair does possess the two necessary elements of cell multiplication and matrix secretion. Since cartilage is avascular there is no phase of acute inflammation, which is important to the delivery of repair substances. Instead, there are only phases of necrosis and proliferation [50]. In both partial and full thickness lesions, the bordering 50µm to 100µm of cartilage undergoes necrosis for a two week period. This constant width of the necrosis zone suggests a mechanism dependant on the diffusion of substances into the tissue. After approximately three weeks, cell clusters of chondrocytes are present adjacent to the necrotic zone. It is believed that these cell clusters are due to cell proliferation rather than a redistribution of existing chondrocytes [18]. It is possible that proteoglycans have direct control over chondrocyte proliferation in their immediate vicinity [51]. There is also an indirect effect of matrix changes on diffusion of nutrients. Fissured cartilage would provide easier access to nutrients, supporting a greater amount of chondrocytes. However this phase of proliferation is short lived. Initially the chondrocytes are highly active, but eventually their synthetic activity subsides [52] and the cells degenerate [53]. Unfortunately the intrinsic repair process contributes no more to wound healing than some reorganization of the necrosis zone [50].

2.2.2. Treatments for Osteoarthritis

Individuals affected with osteoarthritis have available various treatments such as basic exercise and joint care, medicines, and surgical methods. However, there is presently no cure for osteoarthritis and these treatments only serve to reduce the severity of its symptoms.

There are various non-medicinal treatments available that are successful in reducing the symptoms of osteoarthritis. Treatments such as exercise and weight control help to strengthen the joint and reduce the daily impact that it normally receives from the body. Sometimes people require the use of splints or canes for stability and to reduce the loads placed on the joint during daily activities. Similarly, there are various non-drug techniques, such as heat and cold packs, which are employed by many people to reduce the swelling, inflammation and pain of affected joints [1].

Alternatively, there are also several medicinal treatments for osteoarthritis. The most basic form is the use of acetaminophen, or Tylenol, to relieve pain. Alternatively, non-steroidal anti-inflammatory drugs (NSAIDs), such as aspirin and ibuprofen, can be used to block the production of prostaglandins that trigger inflammations [16]. However, the regular use of NSAIDs brings forth the risks of side effects, such as the development of stomach ulcers [1]. In addition aspirin, has been shown in animal studies to inhibit proteoglycan synthesis and cartilage repair processes in animals [54]. Specific to patients with osteoarthritis, hyaluronic acid injections replace any lost fluid in the joint and help to suppress inflammation. Hyaluronic acid is a normal component of the joint that is involved in joint lubrication and nutrition. Dietary supplements such as glucosamine and chondroitin sulphate can also be administered to patients with osteoarthritis. Glucosamine stimulates the production of glycosaminoglycans, the sugar component of proteoglycans. Chondroitin sulphate is a type of glycosaminoglycan and hence a primary building block of cartilage [1,16].

When other treatment methods are unsuccessful in reducing the symptoms of osteoarthritis, surgical methods can be mediated. Surgical methods span a variety of techniques such as tissue grafting, matrix suspensions, and joint replacements.

There are several grafting methods used in the surgical treatments. Perichondrial tissue has excellent repair promoting properties. However, when grafted into the damaged area, long term stability has not been achieved because the transplanted material tends to detach. Osteochondral grafts, as in mosaicplasty, do not integrate with the native tissue resulting in degeneration of the transplanted tissue. Matrix embedded procedures require a culture of the patient's chondrocytes. The matrix used by this procedure must be biocompatible, mechanically stable and promote integration with the native cartilage tissue. The matrix serves as a scaffold that optimizes the density and immobilization of the chondrocytes. The critical size limit of a spontaneous healing response can be overcome by the bridging action of a proper matrix. Similarly, chondrocyte matrix suspensions can be contained at the lesion using a periosteal flap, which helps to organize and assist the repair response. Unfortunately, treatments using these techniques have been unpredictable. These failures can be attributed to the hypertrophy of chondrocytes, poor matrix properties, and the stability of the surgical procedure [47].

If the joint damage is too severe, the only solution will be a total joint replacement. However, artificial joints only have an average lifetime of 15 to 20 years, requiring future surgical procedures depending upon the age of the patient [1].

2.3. Cellular Exposure to Electric and Magnetic Fields

2.3.1. Exposure to DC Electric Fields

As will be discussed, DC electric fields can alter the behaviour of biological cells through electric field induced migration and shape change by mimicking the electric fields naturally produced at the site of traumatized tissue. At the local site of injury the surrounding cells have damaged cell membranes. The ion flux through these leaky membranes produces a wound current. Studies have shown that lateral electric fields of strengths 1V/cm to 2V/cm form across the site of injury [55]. This wound current flows through the low resistance of the wound pathway. As a result the voltage at the center of the wound is more negative than surrounding areas [56]. It is estimated that during human development in the womb the body experiences electric fields of 5V/cm [57]. Similarly, joint loading produces electric fields in cartilage tissue of strengths up to 15V/cm [58].

In vitro studies using cultured chondrocytes have demonstrated that exposure to a DC electric field, in the range of 1V/cm to 6V/cm, increased their motility with a unified direction towards the cathode of the field [59,60]. In experiments performed at Columbia University [59], chondrocytes possessed a control speed of $5.5 \pm 4.65 \mu\text{m/hr}$. However, with a directed velocity of only $0.95 \pm 5.3 \mu\text{m/hr}$, the direction of chondrocyte movement was highly random. A threshold electric field strength of 0.8V/cm was found to significantly increase the directed velocity of chondrocyte migration. Under these conditions the speed of migration was $8.17 \pm 6.92 \mu\text{m/hr}$, with an increased directed velocity of $1.81 \pm 8.1 \mu\text{m/hr}$. Further experimentation revealed that the migratory effect became dose dependant for field strengths exceeding 4V/cm. Chondrocytes exposed to a 10V/cm electric field possessed a speed of $23.54 \pm 11.03 \mu\text{m/hr}$, with a drastically increased directed velocity of $17.59 \pm 15.35 \mu\text{m/hr}$ towards the cathode of the electric field. It has been suggested that the general speed and directed velocity of cell motility are controlled by independent signalling pathways [56]. Electric fields affect the immediate behaviour of chondrocyte cells, as there was no observed latency time before the initiation of the field-induced migration [59].

Exposure to electric fields causes the reorganization of cell surface receptors with the actin cytoskeleton. Chondrocytes migrate by projecting broad actin-filled lamellipodia. They establish pseudopodia and lamellipodia at their leading edge and ruffled borders at their trailing edge [61]. After one hour of exposure, the chondrocytes began to elongate perpendicular to the applied electric field [59]. This perpendicular alignment of the cell may be an attempt to minimize the electric field gradient across the cell [62].

Electric fields can similarly affect the behaviour of cell types other than chondrocytes, such as epithelial cells [63,64,65,66], endothelial cells [67], and fibroblasts [68,69]. A threshold 1V/cm electric field applied to corneal epithelial cells and keratinocytes caused their migration towards the cathode at an average speed of $30\pm 2\mu\text{m/hr}$ and $34\pm 2\mu\text{m/hr}$ respectively [66]. The directional migration of endothelial cells could be increased in speed under high electric field strengths of 10V/cm. This process was partially self sustaining once the cell became polarized. Asymmetric distribution of lamellipodia persisted with the removal of the electric field and random orientation gradually returned over a one hour period [67].

Actin organization within the cell is responsible for the extension and retraction of lamellipodia and other locomotive protrusions. DC electric fields can suppress the protrusive activity from anode-facing surfaces of the cell while stimulating those facing the cathode [67]. Exposure to electric fields disrupts the cytoskeletal actin network and increases intracellular calcium concentration. It is believed that lamellar extension is regulated by calcium concentration within the cytoplasm, since cellular response was inhibited when calcium flux across the membrane was blocked [70,69]. At the cathode facing side, calcium will activate actin-binding proteins such as gelsolin, thereby creating more actin filaments [67]. This will cause the lamella to swell, due to either osmotic pressure or hydrostatic pressure from the actin network. Hence the cell will move forward and form new attachment sites. Calcium entry near the cell body will activate the actomyosin contractile system, pulling the cell forward. Consequently, increased tension within the cell will cause the retraction of the anode facing side [69]. Electric field

exposure also induced a transient 80% increase in the total actin content of cytoplasm. During exposure, actin filaments became asymmetrically distributed, favouring the cathode facing side of the cell [67]. These filaments were orientated perpendicular to the applied electric field [65]. At high field strengths of 10V/cm, the endothelial cell was stretched completely perpendicular to the orientation of the field [67].

The perpendicular alignment to an electric field was observed in many cell types. Myoblasts placed in electric fields as low as 0.36V/cm developed a bipolar axis [63]. Fibroblasts were sensitive to a threshold DC electric field of 1.5V/cm, orienting their long axes perpendicular to the field lines after ninety minutes of exposure [68,69]. When fibroblasts are exposed to 10V/cm electric fields, the occurrence of spindle shaped cells increased dramatically during a one hour period [69]. It was demonstrated in epithelial cells, that these behavioural alterations were not permanent effects as both cell shape and orientation usually relaxed within an hour of field removal [65]. When the conductance differs on opposite sides of the cell, the initial response of many cells is to withdraw their anode and cathode facing protrusions. Hence cells elongate perpendicular to the field in order to minimize voltage drop across the cell. Those portions of the cell periphery that retract are the locations most strongly perturbed from the resting potential [71].

Electric fields target the plasma membrane, since it is site of the most electrical resistance in the cell [68]. There are various signalling pathways, such as membrane polarization or electro-osmosis, by which electric field exposure could modify the behaviour of cells [72]. Electric fields depolarize the cathode facing sections of the cell membrane and hyperpolarize anode facing sections, resulting in a differential opening of voltage-regulated ion channels on opposite sides of the cells [73]. A perturbation of 2mV to 6mV in the resting membrane potential of a cell, possible with electric fields of 1V/cm, would be sufficient to influence local ion permeabilities and cell behaviour [68]. This limits ion entry to certain areas of the cell.

Alternatively, electro-osmosis may redistribute cell surface receptors towards the cathodal face of the cell membrane. Since the membrane has high impedance this lateral

mobility of cell proteins may be due to current flowing around the cell [59]. In spherical cells, this lateral flow of current can locally increase the electric field by 50% [73]. Therefore, increased forces from the electric field can move charged lipids and glycoproteins towards one end of the cell [56].

2.3.2. Exposure to DC Magnetic Fields

Several studies have demonstrated that magnetic field exposure has the ability to alter the development of biological organisms. The use of permanent magnetic fields has shown promising results in the treatment of canine osteoarthritis [74]. The transected knees of mature mongrel canines were exposed to magnetic fields ranging from 0.5mT to 20mT, depending upon whether the animal was sitting or standing on the mattress placed in their cage. After an exposure period of 12 weeks there were significant improvements in histological reports of the osteoarthritic knee. The immunohistochemical results of the osteoarthritic knee were the same as in the normal knee after the magnetic therapy, indicating a restoration of normal protein expression in the cartilage tissue. Exposing sea urchin embryos to a 30mT static magnetic field caused significant developmental changes. In terms of cellular development, there was a notable increase in the length of time between cell divisions. During the development of the organism, magnetic field exposure promoted birth defects such as exogastrulation and collapsed embryos [75].

Several studies have been performed on cell cultures exposed to static magnetic fields. After exposing *F. culmorum* cultures to a 300mT magnetic field for one week, the cell walls were shrivelled, possessed disorganized organelles in the cytoplasm and had an increase in the amount of vacuoles and lipid bodies. In addition, the exposure reduced the concentration of proteins within the cell, inhibited germination and exposed cells were unable to use calcium from their intracellular stores [76]. Lymphocytes exposed to a 6mT static magnetic field, for up to five days, also experienced several changes. Their shape changed from rounded to an irregularly elongated morphology. They also experienced a decreased apoptotic rate accompanied by an increase in intracellular calcium concentration [77]. Contrastingly, when Hep G2 cells were exposed to a 6mT magnetic field for twenty-four hours, they changed from a flat polyhedric shape to a round

morphology with lamellar microvilli. As well, these cells experienced a transient increase in calcium concentration, accompanied by an increase in apoptosis. Following removal from the magnetic field, these effects on cell morphology and apoptosis remained for more than an hour [78].

This phenomenon regarding intracellular calcium has been examined in several other studies. Exposing U937 monocytic cells to a 6mT magnetic field revealed that rather than calcium being released from the intracellular stores of the endoplasmic reticulum, the calcium influx occurred through the cell membrane from the extracellular environment [79]. This magnetic field induced change occurred in less than 100 seconds. Calcium plays an important role in the reorganization of cytoskeletal elements, initiation of apoptosis, and as a mediator of intracellular signalling [78]. It is thought that magnetic fields have a general effect on the molecular structure of excitable membranes. Morphological and structural changes to cell membrane will interfere with the function of ion channels [80]. Exposing a cellulose membrane to a 240mT magnetic field enhanced the rate of ion transport. Interestingly, the transport rate did not return to initial levels after being removed from the field [81]. It is suggested that static magnetic fields may have stabilized a hydration layer on the cellulose surface reducing the electrostatic attraction to ions [82].

Other studies indicated that static magnetic fields alter cell membranes because of the diamagnetic properties of membrane phospholipids. Experiments using 123mT magnetic fields were able to inhibit the potentials created in presynaptic membranes of nerve cells after 50 seconds of exposure [83]. Once the magnetic fields were removed, the nerve cells required 135 seconds to recover normal functionality. These time requirements comply with a slow reorientation of diamagnetic molecular domains within the membrane following exposure to a magnetic field. Similar effects were observed on the kinetics of voltage activated sodium channels in GH3 cells when placed in a 125mT magnetic field [84]. In a homogeneous magnetic field diamagnetic anisotropic molecules will reorient towards a minimum free energy state if the magnetic anisotropic energy exceeds the thermal energy of the system [85]. In biological membranes these

diamagnetic molecules are highly organized. Hence the anisotropies can be summed, allowing for this orientation to occur at lower magnetic field strengths [84]. This reorientation of the membrane is capable of distorting imbedded ion channels to alter their function [86].

2.3.3. Exposure to Electromagnetic Fields

2.3.3.1. Exposure to Pulsed Electric Fields

Pulsed electrical stimulation (PES) has shown promising results in the treatment of osteoarthritis. PES is delivered through surface electrodes placed on the skin of the patient. In one study, a group of patients requiring total knee arthroplasty were treated with the BioniCare Stimulator System, 8.5 hours per day for the duration of an entire year. Interestingly, 62% of patients treated with PES were able to defer surgery for four years, as compared to only 7% of patients in the control group [12]. As a result of this study, PES is a potential non-invasive treatment for patients. Another study exposed osteoarthritic knees to a 100Hz pulsed electric field delivered at night for a four week duration. Results indicated improvements in knee pain, function, knee flexion and duration of morning stiffness. Specifically, the duration of morning stiffness was reduced by at least fifteen minutes in 47% of the exposed patients, while in only 25% of the control patients. Similarly, the flexion of the knee improved by at least five degrees in 45% of the exposed patients, while in only 18% of the control patients [11]. These improvements in patients with osteoarthritis can partially be explained with the following animal study. When PES treatments were applied to defects in rabbit knee cartilage, the repair tissue more resembled hyaline than fibrous cartilage. Closer examination revealed that PES exposure increased chondrocyte proliferation as well as glycosaminoglycan and type II collagen synthesis [87]. A potential drawback of PES treatments is that 24% to 31% of patients received mild skin reactions to the electrode gel used to improve electrode contact with the skin [11].

The effect of PES on chondrocyte behaviour has also been investigated. Wang et al [88] exposed bovine chondrocytes to a capacitively coupled sinusoidal electric field. Their

intent was to determine optimal electric field parameters of duty cycle, stimulus duration, field amplitude and frequency for the production of proteoglycan and type II collagen. Production of proteoglycans by chondrocytes was optimized with a 10mV/cm, 60kHz, 50% duty cycle electric field. At these settings, proteoglycan synthesis was increased eight-fold after a 0.5 hour treatment. Interestingly, the maximal production did not occur until 3.5 hours after removal from the electric field. In terms of type II collagen production, the optimal electric field parameters were found to be a 20mV/cm, 60Hz, 8.3% duty cycle signal. Use of these settings increased type II collagen production five-fold following a 0.5 hour treatment. Similar to the case with proteoglycans, the maximal production of collagen did not occur until 5.5 hours after removal from the electric field. Unlike proteoglycan production, there was not a progressive increase in collagen production with successive exposure repetitions. The rate of collagen production remained constant at that set by the initial application. These promising results on chondrocyte metabolism enforce the development of PES as a technique to positively affect cartilage metabolism in patients with osteoarthritis.

Lastly, the effect of pulsed electrical stimulation on cell physiology and function has been investigated with other cell types. Exposing HT-1080 tumour cells to a 20V/cm electric field pulsed at 0.05Hz, caused either the resonance or cancellation of nicotinamide adenine dinucleotide (NAD(P)H) oscillations naturally occurring in the cell, depending if the two signals were in or out of phase. NAD(P)H is important for catabolic and biosynthetic reactions as well as intracellular signal transduction. During NAD(P)H resonance, enhanced proteolytic activity is linked to the metastatic potential of tumour cells. In addition, metabolic resonance increased the production of oxygen radicals, leading to deoxyribonucleic acid (DNA) damage after as little as five minutes of exposure. Since the electric field threshold for behavioural response was only 1mV/cm it is possible that environmental electric fields could also influence cell physiology [89].

2.3.3.2. Exposure to Pulsed Magnetic Fields

Pulsed magnetic field exposure has been used clinically since 1977 to treat non-union bone fractures. Bassett [8,90] developed a system using quasi-rectangular, 0.3msec magnetic pulses applied to patients facing amputation. After a treatment of 10hrs/day to 12hrs/day for an average of 5.5months, there was an overall success rate of 77% in the healing of these fractures.

This technique had several benefits over other healing alternatives, such as direct electrode implantation used in PES. Pulsed magnetic field exposure, referred to from now on as PEMF, doesn't require surgical procedures to install and remove the electrodes [13] because it is completely non-invasive. Whenever surgical procedures are used there is always the risk of infection [13] occurring at the site of electrode implantation. In addition, electrodes are subject to corrosion and electrolysis [15] while implanted, causing possible complications. PEMF uses wire coils placed around the outside of the target area to generate a time-varying magnetic field. Hence the site of tissue stimulation is not limited [14] while using PEMF treatments, as it is with direct electrode implantations. As a result, treatments using PEMF exposure are preferred over direct electrode implantation.

Further investigation into this phenomenon on bone healing looked at the exposure of osteoblasts and osteoclasts to electromagnetic field exposure. Osteoblasts have been exposed to quasi-rectangular waveforms of varying magnetic field strength (0.1mT to 7mT), pulse width (0.15msec to 1.3msec), and repetition frequency (15Hz to 75Hz). These studies all reported an increased rate of osteoblast proliferation as a result of the PEMF exposure [91-93]. Rats were exposed to quasi-rectangular magnetic fields for 8hrs/day for thirty days. The magnetic field strength had a range of 0.4mT_{RMS} to 0.8mT_{RMS}, with a pulse width of 0.3msec, repeated at a frequency of 7.5Hz. Results indicated preventative effects on trabecular bone loss [94]. Further investigation exposed rat bone marrow cells for seven days. Using the same temporal characteristics in a quasi-rectangular waveform revealed that PEMF exposure had varied inhibitory effects on the

recruitment of osteoclast cells depending upon the magnetic field strength ($0.13\text{mT}_{\text{RMS}}$ to $0.32\text{mT}_{\text{RMS}}$) and the duration of the exposure period (0.5hrs/day to 8hrs/day) [95].

PEMF exposure has also been used clinically to treat osteoarthritis. This is a more recent application than that of the bone healing systems. These osteoarthritis systems use a quasi-rectangular or otherwise pulsating waveform with a range of magnetic field strength (0.04mT to 2.5mT), pulse width (0.25msec to 80msec) and duty cycle (15% to 80%) delivered using a unique pulse train system [22,96-99]. These techniques are based upon the knowledge of electric fields induced within the tissue of interest. The characteristics of these induced electric fields are designed to mimic the “streaming potentials” that naturally occur when cartilage is compressed. It is believed that these “streaming potentials” stimulate the repair mechanisms of chondrocytes within cartilage tissue [96]. These clinical trials exposed patient’s knees, affected with osteoarthritis, to PEMFs for session durations lasting up to thirty minutes per day for as many as eighty-four sessions. The general consensus from these clinical treatments was that PEMF exposure reduced the severity of symptoms up to 36% when compared to non-treatment. The criteria for these tests were based on knee pain and stiffness, and the effect on active daily living. [22,96-99]

Clinical trials using a treatment known as PST have been performed on over 100,000 patients in Europe, the USA and Canada [10]. PST generally uses a quasi-rectangular waveform with a magnetic field strength of 1.25mT , frequencies from 1Hz to 30Hz, and duty cycles greater than 50% [9,10] for the treatment of osteoarthritis. After exposure for 1hr/day for nine days, 73% of patients responded positively to PST, based upon a 20% improvement in the Lequesne Knee Arthritis Index, severity of pain, and difficulties in performing daily activities [9]. Following treatment in the deteriorative cytokine IL-1B, exposing cultured chondrocytes to three hours of PST per day restored proteoglycan production and cellular structures [100,101].

Several animal studies have investigated the effects of PEMF exposure on cartilage. Hartley guinea pigs were monitored according to the morphology of cartilage following

exposure to PEMFs. One study used a ramping magnetic field of $0.1\text{mT}_{\text{peak}}$, a pulse width of 30msec, and a repetition frequency of 1.5Hz [102]; another study used a magnetic field strength of 1.6mT, a pulse width of 1.3msec, and a repetition frequency of 75Hz [103]. The animals were exposed for 1hr/day for six months and 6hrs/day for three months, in each of the studies respectively. In both studies, examination of the cartilage revealed that PEMF treatment preserved the morphology of articular cartilage, reversed the development of osteoarthritic lesions, and increased the thickness of cartilage [102,103]. Rats were exposed to a ramp magnetic field of $1.6\text{mT}_{\text{peak}}$, with a 4.5msec pulse burst repeated at 15Hz, for 8hrs/day for eight days. The exposure increased the content of proteoglycan and type II collagen in the cartilage matrix [104].

A multitude of experiments have also been performed exposing *in vitro* cultured chondrocytes to a range of PEMF characteristics. These studies analyzed various parameters such as serum concentration, coil orientation, and magnetic field strength on the resulting behaviour of chondrocytes. One study exposed chondrocytes to a magnetic field strength of 2.3mT with a pulse duration of 1.3msec at a 75Hz repetition rate. The results of the experiments demonstrated that an increase in cellular proliferation in response to eighteen hours PEMF exposure required the presence of 10% serum in the dish [105]. Hence, growth factors are important to PEMF stimulation. Another experiment exposed chondrocytes to a quasi-rectangular magnetic field of $3.5\text{mT}_{\text{peak}}$ with a pulse duration of 0.38msec at a 72Hz repetition rate [106]. These results demonstrated that chondrocyte proliferation in medium containing 3% serum could be decreased after six days of PEMF exposure if the coil orientation was changed from horizontal to vertical. As a result, the presence of electromagnetic vectors in the plane of cell adhesion affected the rate of cellular proliferation. Studies have also demonstrated that up to forty-eight hours of PEMF exposure can increase the rate of proteoglycan synthesis in cultured chondrocytes. These studies utilized a pulsating waveform with varying magnetic field strength (0.2mT to 1.5mT), pulse duration (0.2msec to 1.3msec) and repetition rate (15Hz to 75Hz) [107,108]. PEMF exposure also enhanced chondrogenic differentiation and phenotypic maturation. When chondrocytes are grown in a monolayer they typically

adopt properties of fibroblasts. However, exposure to PEMFs preserved their typical round morphology and synthesis of type II collagen [108,109].

Other cell types such as keratinocytes [110], fibroblasts [111] and rat bone marrow (RBM) [112] have been exposed to PEMFs. When keratinocytes were exposed to a 2mT_{RMS} sinusoidal magnetic field at 50Hz for ninety-six hours, there was increased proliferation and expression of actin at apical sites of the cell membrane [110]. When fibroblasts were exposed to a ramping magnetic field of $1.88\text{mT}_{\text{peak}}$ with a pulse duration of 1.34msec at a 50Hz repetition rate, there was significant clustering of intramembrane proteins after two hours compared to the control cultures [111]. Hence PEMFs have the ability to modify morphology and cytoskeletal elements. PEMF also has the ability to affect the adhesion of RBM cells. Exposure of RBM cells to a 0.5mT_{PP} sinusoidal magnetic field at 1000Hz, caused the detachment of pre-attached cells after four days, as well as prevented the attachment of cells not pre-attached. As the cells detached from the dish they changed from a stellate to a spherical morphology [112].

Most researchers believe that electromagnetic fields are able to alter cellular behaviour through interactions at the cell membrane. The cell membrane serves as the gateway to the cell interior. The biological membrane is a phospholipid bilayer that acts as an electrical insulator. Since the conductance of the cell membrane is five orders of magnitude less than either the extracellular medium or the cytoplasm low frequency electric fields do not penetrate into the interior of cells [113]. Instead the electric field is converted into a surface membrane current [114]. On the other hand, low frequency magnetic fields are unattenuated by cell membranes. However, since cell dimensions are small the induced electric fields within the cytoplasm are also small [115]. Tenforde [113] states that by regarding the cell as a dielectric shell surrounding a spherical conductor, there is an amplification of the extracellular electric field density across the membrane according to the factor $1.5R/d$, where R is the cell radius and d is the membrane thickness. If the average chondrocyte radius is $25\mu\text{m}$ [18] and membrane thickness is 5nm [113] then the amplification factor is approximately 7500. Although there is an amplification of the electric field across the membrane, electrical noise makes

it difficult to achieve a sufficient signal-to-noise ratio (SNR). The sources of this noise are Johnson-Nyquist thermally-generated electrical noise, ion current flows, shot noise, and endogenous biological background fields [113]. In fact the minimum induced electric field strength within the extracellular medium ranges between 1mV/cm and 10mV/cm, depending upon cell geometry, in order to achieve unity SNR across the membrane [116]. As a result, the induced electric fields from the majority of therapeutic devices using electromagnetic fields are too small to directly depolarize cell membranes [9,117]. The generation of an electric field by a time-varying magnetic field is also very inefficient in regards to energy transfer [118].

Instead the effectiveness of electromagnetic field exposure relies upon signal amplification by transmembrane receptors [117]. A possible signal transmission pathway at the cell membrane begins with the modulation of calcium binding at the cell surface by electromagnetic fields. This signal is transmitted along strands of receptor proteins. It becomes amplified since one receptor strand can activate many molecules of G protein to stimulate or inhibit ATP [119,120]. Through these signal transduction pathways of enzymatic amplification, electromagnetic stimuli can elicit a cellular response. This methodology of transmembrane receptors depends upon the ability of electromagnetic fields to interact with ions at charged interfaces. It is believed that there are combinations of amplitude and frequency of the electromagnetic field that can invoke the optimal cellular response [114].

2.4. Theory of Ion Resonance

According to the electrochemical information transfer hypothesis, low level electromagnetic fields interact with cell membranes by enhancing the binding rate of ions with enzymes and receptors [121,122]. There are several models that attempt to explain how electromagnetic fields interact with the flux of ions across biological membranes. These models include theories of ion cyclotron resonance, ion parametric resonance, and ion-molecular orbital procession [123]. In fact the theory of ion parametric resonance [124,125] can be considered an expansion of ion cyclotron resonance [126,127] in transmembrane channels. These two models will be explained in detail since they form the basis of further experimentation performed in this thesis.

Ion cyclotron resonance requires specific magnitudes of parallel AC and DC magnetic fields operating at a specific frequency in order to invoke the resonance of a particular ion in a transmembrane channel. This theory is derived from the knowledge that ions are weakly bound within a protein molecule. The resulting complex is a charged oscillator that vibrates at the frequency of thermal motion. When this complex is placed within a static magnetic field a Lorentz force is exerted on the moving ion charge. The Zeeman effect occurs and these oscillations will degenerate into two oscillation frequencies. The difference between these frequencies is known as the cyclotron resonance frequency f and is predicted by equation 2-1. As long as the AC magnetic field is at the resonant frequency the ion will gain energy as it moves in circular orbits. [118,123,126,127,128,] Collisions between ions will dampen the energy gain on the target ion. Resonant effects will not occur unless the effective collision frequency is smaller than the frequency of the applied field [129].

$$f = \frac{qB_{DC}}{m2\pi n} \quad (2-1)$$

Where q/m is the charge to mass ratio of the target ion and B_{DC} is the magnitude of the DC magnetic field, and n is the frequency index

There is an operating window to which an ion in a transmembrane channel will resonate when placed in an electromagnetic field. This operating window is specified by the frequency index n . An ion will be in resonance when the frequency index of the applied electromagnetic field is within 10% of an integer value [130].

Different interpretations of equation 2-1 will affect the calculated resonant frequency for the ion complex. Often researchers are unsure of the proper q/m ratio for the target ion. Since there is a high probability that the ions will be hydrated, m should include the mass of the attached water molecules [118]. However, in the theory of ion parametric resonance, an unhydrated ionic state is assumed [130].

Ion parametric resonance further specifies the parameters of the electromagnetic field by creating a resonance dependence on the magnitude of the applied AC and DC magnetic field. Lednev [124,125] stated that the ratio of the AC and DC magnetic field magnitudes will affect the transition probability p of an ion from an excited vibrational state frequency to the ground state frequency [118,123] and hence the occurrence of a resonant event. This work was revised by Blackman et. al [130,131] into the relation shown in equation 2-2. Different from the original Lednev formulation, their equation introduced a $(-1)^n$ term and a factor of 2 in the B_{AC}/B_{DC} ratio.

$$p = K_1 + (-1)^n K_2 J_n(2nB_{AC} / B_{DC}) \quad (2-2)$$

Where K_1 and K_2 are constants, J_n is the n th order Jacobian, B_{AC} is the peak-to-peak magnitude of the AC magnetic field, and B_{DC} is the magnitude of the DC magnetic field

Divalent ions are more likely to cause a biological effect since they have a longer lifetime than monovalent ions [128]. For resonance to occur the residence time of the ion in the excited vibrational state must be at least as long as the period of the applied AC magnetic field. [118,123,128]

There exists some controversy over the use of equation 2-2 which relates to whether peak-to-peak (PP), peak, or root-mean-square (RMS) values should be used for the AC

magnetic field. Although this formula is designed for peak-to-peak values of the AC magnetic field, its validity has been compromised by some studies using improper measurements [131].

Several studies have investigated the resonance of biologically important ions in transmembrane channels during exposure to electromagnetic fields [132,133,134]. Exposing a cell membrane to an AC magnetic field of $26\mu\text{T}_{\text{peak}}$ and a DC magnetic field of $37\mu\text{T}$ for thirty minutes, Barueus [132] found that ion flux deviated at frequencies of 21Hz, 24Hz, and 31Hz, corresponding to the resonant settings for Mn^{2+} , Ca^{2+} , and Mn^{3+} respectively. Expanding to single cell organisms, Smith [133] demonstrated the enhanced mobility of diatoms when exposed to an electromagnetic field calibrated for calcium ion resonance. Characteristics of the resonant electromagnetic field were equal AC and DC magnetic field components of $20.9\mu\text{T}$ at a frequency of 16Hz and 48Hz. In relation to the work of this thesis, Grande [134] exposed bovine chondrocytes to a resonant electromagnetic field for twenty-four hours to seventy-two hours. Monitoring proteoglycan synthesis, resonant conditions were found at an AC magnetic field of $40\mu\text{T}_{\text{PP}}$ and frequency of 16Hz when the DC magnetic field was set to $40.8\mu\text{T}$, $20.9\mu\text{T}$ and $12.7\mu\text{T}$, corresponding to K^+ , Ca^{2+} , and Mg^{2+} respectively. Although a slightly different q/m ratio was used between Barueus [132] and Grande [134], these experiments indicate that the resonance of ions in transmembrane channels can be predicted by equation 2-1 and has the ability to alter cellular behaviour.

Chapter 3

3. Effect of PEMF Exposure on Chondrocyte Morphology

This chapter describes a preliminary study performed by the laboratory on the effect of PEMF exposure on chondrocyte morphology. The experiments demonstrated that under certain PEMF conditions, exposure could invoke a change in chondrocyte morphology. The experimental protocol was performed on *in vitro* cultured human chondrocytes in a controlled laboratory environment. The material of this chapter was published in the Journal of Medical and Biological Engineering and Computing [135].

3.1. Objectives

The primary objective of these experiments was to investigate the effect of specific PEMFs on chondrocyte morphology.

The secondary objective of these experiments was to determine whether the initial morphological state of the chondrocytes would affect their morphological response to PEMF exposure.

3.2. Materials and Methods

3.2.1. Chondrocyte Culture

Cartilage samples were removed from femoral condyles obtained from patients undergoing total knee replacement surgery. The cartilage was minced into 1mm³ pieces and subsequently digested in a 1mg/ml collagenase 1a (Sigma) solution for six hours with shaking. The resulting chondrocytes were plated and allowed to reach confluence in chondrocyte growth medium (CGM, Cambrex) where they were incubated at 37°C in a humidified incubator containing 5% CO₂. These cells were analyzed for the presence of chondrocytic markers including collagen II and aggrecan by immunofluorescence. Prior to applying the PEMF treatment, chondrocytes were trypsinized and reseeded at the desired density (100,000 cells / 30mm dish) after which they were incubated for either

one hour or twenty-four hours. From the same batch of cultured chondrocytes, both a control and experimental dish were created for each experimental trial.

3.2.2. Experimental Setup

The experimental and control dishes were placed in a coil set (figure 3-1) at the location specified by the experimental trial (table 3-1). Depending upon the experimental conditions, either a small coil (4.25cm radius, 120turns) or large coil (6.5cm radius, 230 turns) was required to create desired magnitude of magnetic and electric fields. The coil set was positioned inside a humidified incubator at a temperature of 37°C containing 5% CO₂. A current was applied to the coil set containing the experimental dish to generate the desired PEMF. The control dish was incubated under identical conditions, but without a current applied to the coil set; hence no PEMF exposure.

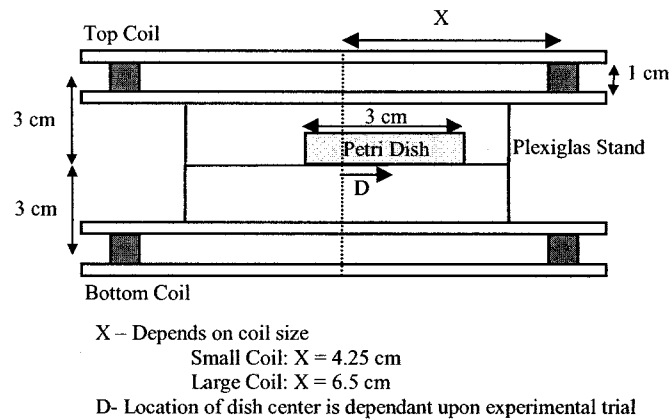


Figure 3-1: Placement of cultured human chondrocytes in the coil set.

This study was performed in two parts. In part one, the culture dishes were incubated for twenty-four hours to allow the cells to attach to the surface of the culture dish prior to PEMF exposure. As seen in figure 3-4, the cells initially possessed either a stellate or spindle morphology with extended processes. Six experimental trials (A-F), outlined in table 3-1, were performed to investigate the effects of specific electromagnetic fields on chondrocyte morphology. The general range of magnetic fields and frequencies used in these trials was based upon literature discussed in chapter 2. In conjunction with the placement of the culture dish within the coil set, experimental conditions were obtained

that tested combinations of relatively high, medium, or low magnetic and electric field strengths. Since the magnetic and electric fields are not uniform across the radius of the coil (figure 3-2), the placement of the culture dish can alter the experimental conditions. In all the experimental trials, a ramp magnetic field (figure 3-3) was applied to the cultured chondrocytes. A ramp magnetic field has been used by other studies, as reviewed in chapter 2, and induces DC electric fields on the surface of the culture dish.

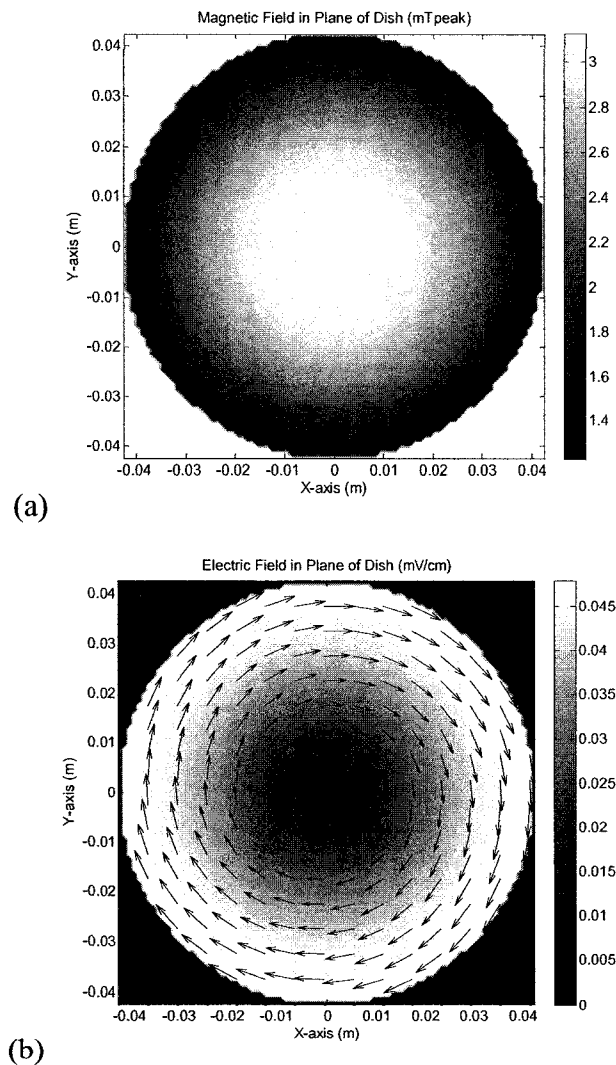


Figure 3-2: Theoretical models of the (a) magnetic and (b) electric fields in the plane of the dish, taken at the midpoint separation distance between the small coil pair, for a $3.14\text{mT}_{\text{peak}}$, 100Hz exposure

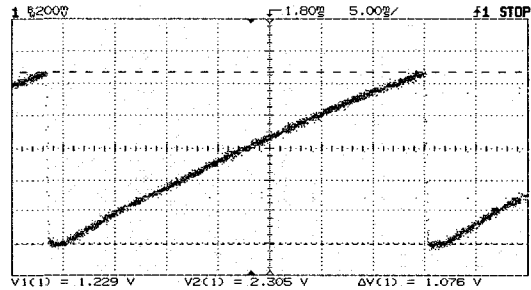


Figure 3-3: Example of ramp magnetic field used in experimental trials

Part two existed as a follow-up to the findings of part one. In part two, the cells were incubated for one hour prior to PEMF exposure, depriving them of sufficient attachment time. As seen in figure 3-6, these cells initially possessed a spherical morphology with retracted processes. Part two consisted of a single trial (G), outlined in table 3-1, that induced a morphological change in the chondrocytes for part one. Its purpose was to determine whether the initial morphological state of the cells would affect their morphological response to PEMF exposure.

The cultured chondrocytes were exposed to the PEMF for six hours. Using a Leica DMR light microscope, light micrographs at the center of both the control and experimental dish were taken before and at one hour intervals for the duration of the experiment. Images were captured and analyzed using ImageJ software and changes in cell morphology and surface contact area to the culture dish were determined. Due to mechanical restraints, the microscope lens was limited to a 2mm x 2mm viewing area in the middle of the culture dish, with each picture possessing an area of 1mm x 1mm. The exception is figure 3-5b which has an area of 2mm x 2mm. Analysis of figure 3-2 reveals that the maximal magnetic and electric field variability between pictures of the same experimental trial is less than 4% and small compared to the variability between experimental trials.

Trial	Distance from Coil Center (cm)	Frequency (Hz)	Magnetic Field (mT _{peak})	Electric Field at Dish (mV/cm)	Outcome vs. Control
PART ONE					
A	0.25	100	3.14	0.0039	Affected
B*	1.50	100	5.42	0.0407	No Effect
C	0.25	500	1.69	0.0106	Affected
D	2.25	500	0.74	0.0449	No Effect
E	0.25	370	0.85	0.0039	No Effect
F*	1.50	10	5.42	0.0041	No Effect
PART TWO					
G	0.25	100	3.14	0.0039	Affected

* Used small coil size except for in trials B and F (used large coil in these cases)

Table 3-1: PEMF settings and results for part one and part two trials performed on cultured human chondrocytes

3.3. Results

The cultured human chondrocytes were assessed for changes in their characteristic morphology after exposure to the seven PEMF conditions. The outcome of these trials is summarized in table 3-1. Changes in chondrocyte morphology, as compared to control cultures, were only induced in experimental trials A, C, & G. Quantification of the change in chondrocyte morphology during these three experimental trials is summarized in table 3-2.

In part one of this study, the chondrocytes were allowed to attach to the surface of a culture dish for twenty-four hours prior to PEMF exposure. Comparison of the control culture before (figure 3-4a) and after (figure 3-4b) a six hour period does not show a significant change in chondrocyte morphology. In both control pictures, the chondrocytes possess a mixture of stellate and spindle morphologies with extended processes since they were firmly attached to the surface of the dish. Less than 5% of the cells possessed a spherical morphology in the control cultures.

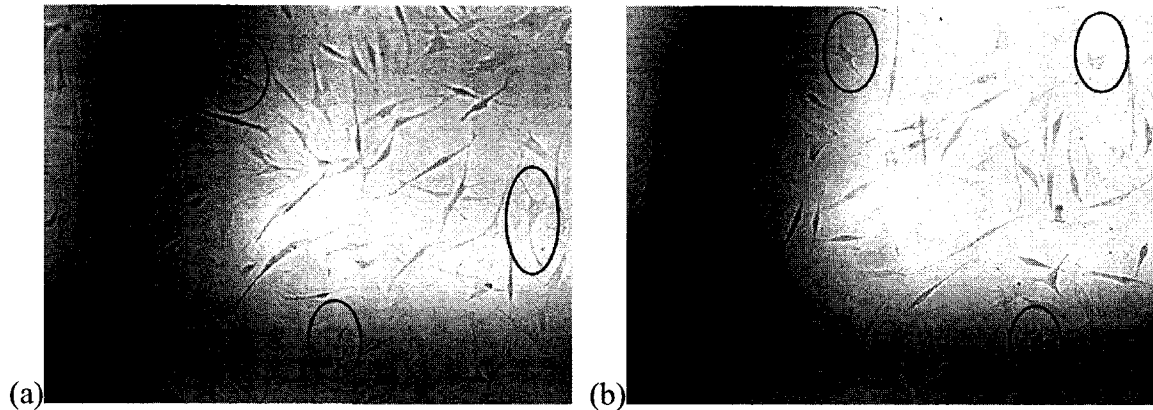


Figure 3-4: Microscope images of chondrocytes in part one control dish (no PEMF) taken (a) before and (b) after a six hour period. There is no significant change in the shape of the chondrocytes. The circled chondrocytes in both pictures possess a stellate or spindle morphology with extended processes.

In the two successful PEMF trials (A and C), a larger proportion of chondrocytes took on a spherical shape without extended processes. In trial A, approximately 35% of the chondrocytes adopted the spherical morphology (figure 3-5a). In addition, there was a 22% reduction in the number of cells present on the pre/post microscope images suggesting that as the cells adopted a spherical morphology, they detached from the surface of the dish and some were lost in the final count. In trial C, initially 73% of the cells possessed a stellate morphology, while 27% were spindle and 5% were spherical. After a three hour exposure period in trial C, approximately 30% of the cells were stellate, 38% were spindle and 32% were spherical in morphology (figure 3-5b). Although the chondrocytes of trial A were exposed to PEMF for six hours, the chondrocytes of trial C were exposed for only three hours since significant results were observed within the shorter time period. Overall, there was a significant shift in chondrocyte morphology from stellate to spherical.

The remaining four PEMF conditions in part one (trials B,D,E&F) did not significantly affect chondrocyte morphology when compared to the control cultures.

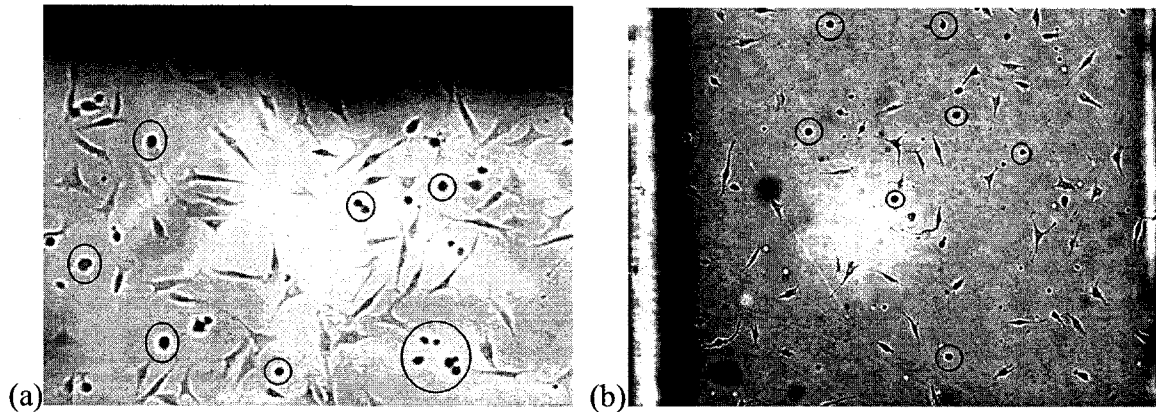


Figure 3-5: Microscope images of chondrocytes in experimental dish (PEMF exposure) for (a) experimental trial A taken after a six hour period and (b) experimental trial C taken after a three hour period. There is a significant change in the shape of the chondrocytes from stellate with extended processes to spherical with retracted processes. The circled chondrocytes in both pictures possess a spherical morphology.

In part two of this study, chondrocytes were allowed to attach to the surface of a culture dish for only one hour prior to PEMF exposure. Experimental results previously confirmed that these PEMF conditions could alter the morphology of chondrocytes. Referring to the control dish used in part two (figure 3-6a), initially 40% of the cells possessed a stellate morphology, 4% were spindle and 56% were spherical. After six hours in the control incubator, the cells continued to attach to the dish and 80% of the cells possessed a stellate morphology, 12% were spindle and 8% were spherical (figure 3-6b).

For the experimental culture of trial G, initially 48% of the cells possessed a stellate morphology, 7% were spindle and 45% were spherical. After six hours of PEMF exposure, 7% of the cells possessed a stellate morphology, 14% were spindle and 79% were spherical (figure 3-7). This morphological change was opposite to that observed in the control culture; yet this change to a spherical chondrocyte morphology was observed when using the same PEMF exposure settings as experimental trial A.

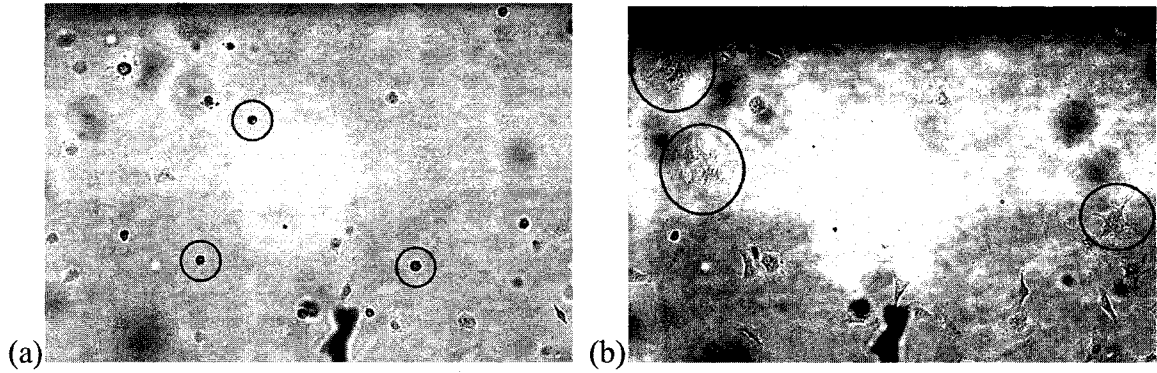


Figure 3-6: Microscope images of chondrocytes in part two control dish (no PEMF) taken (a) before and (b) after a six hour period. The chondrocytes continue to normally attach to the surface of the culture dish during this period. The circled chondrocytes in (a) possess a spherical morphology with retracted processes and in (b) possess a stellate morphology with extended processes.

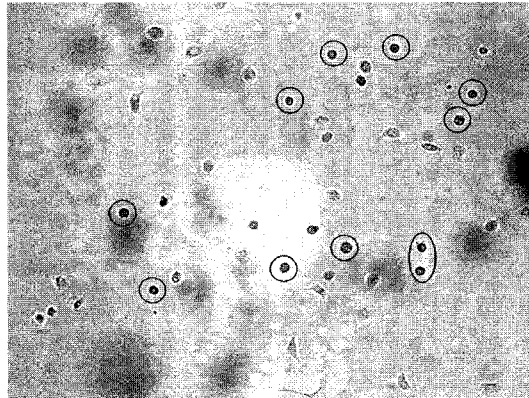


Figure 3-7: Microscope images of chondrocytes in experimental dish (PEMF exposure) for experimental trial G taken after a six hour period. The circled chondrocytes retain their spherical morphology with retracted processes.

Trial	Cell Morphology		
	Spherical	Spindle	Stellate
PART ONE			
Control	5%	n/a	n/a
A			
Post	35%	n/a	n/a
C			
Pre	5%	27%	68%
Post	32%	38%	30%
PART TWO			
Control			
Pre	56%	4%	40%
Post	8%	12%	80%
G			
Pre	45%	7%	48%
Post	79%	14%	7%

Table 3-2: Morphological assessment of cultured human chondrocytes exposed to PEMFs

The chondrocytes were also analysed for their change in surface contact area with the culture dish. The amount of surface contact area between the culture dish and the chondrocyte was measured according to the area of the cell in the captured microscope images. The results are recorded in table 3-3. In regards to cell morphology, the stellate cell morphology possessed the largest contact area. Consequently, the spherical cell morphology possessed the smallest contact area that was on average 58% smaller than the stellate morphology.

In trial C, comparison of the pre and post cell measurements indicated that the amount of surface contact by the chondrocyte decreased due to PEMF exposure. Overall, there was a 30% reduction in the average surface contact area of the cells to the culture dish. This overall reduction in contact area is large because there was a significant change from a stellate to spindle morphology. However, the average surface contact area for a particular characteristic cell morphology (stellate, spindle or spherical) was still reduced by 16% due to PEMF exposure.

In part two, both the control and experimental cultures were analysed for their change in average surface contact area with the culture dish. For the control culture, the overall

surface contact area by the chondrocytes quadrupled during the six hour period, while the average contact area for a particular characteristic cell morphology doubled. For trial G, in agreement with experimental trial C, the overall surface contact area by the chondrocytes decreased by 30%, while the surface contact area for a particular characteristic cell morphology decreased by 16%.

Trial	Change in Surface Contact Area	
	Overall	Particular Morphology
PART ONE		
C	-30%	-16%
PART TWO		
Control	214%	90%
G	-30%	-16%

Table 3-3: Change in surface contact area with a culture dish for cultured human chondrocytes exposed to PEMFs

3.4. Discussion

There are three characteristic morphologies that a cell usually displays: stellate, spindle or spherical. When a cell modifies its shape it is believed that the progression is linear passing from spherical to spindle to stellate. This process is also believed to be reversible [136]. The experimental findings of parts one and two provided preliminary evidence that, at specific conditions, PEMF exposure caused a change in the morphology of chondrocytes. Whether the initial morphology was stellate, spindle or spherical, PEMF exposure caused a change in morphology that followed a predictable path of stellate to spindle to spherical morphology.

Chondrocytes were exposed to both magnetic and electric fields for the duration of the experimental protocol. In the above experiments, PEMF exposure was able to alter chondrocyte morphology with magnetic field strength and frequency settings of $1.7\text{mT}_{\text{peak}}$ at 500Hz and $3.1\text{mT}_{\text{peak}}$ at 100Hz. Other combinations of magnetic field strength and frequency were unable to alter chondrocyte shape. The exposure time in trial C was only half that of trial A, yet similar results were obtained. Although the magnetic field strength was reduced in trial C as compared to trial A, the frequency was increased

respectively. The frequency of the ramping PEMF signal will alter the strength of the induced electric field. Additional experiments are required to dissect out the individual effects of frequency, electric field strength and magnetic field strength on chondrocyte morphology.

The electric field strengths induced in this study ranged from approximately 0.005mV/cm to 0.05mV/cm. As outlined by Tenforde [113], if the average chondrocyte radius is 25 μ m [18] and membrane thickness is 5nm [113] then the amplification factor of the environmental electric field across the cell membrane is approximately 7500. As a result, the electric fields in this study can create a voltage drop of approximately 18.75nV to 187.5nV across the cell membrane. To put this into perspective, the change in membrane potential produced by the opening of a single ion channel is approximately 0.3 μ V [137]. In fact, a minimum electric field of 0.1mV/cm is required to achieve unity SNR [113]. As is the case with other therapeutic devices, the induced electric fields are considerably weaker than the levels required to depolarize cell membranes [9,117]. These experimental results did not provide conclusive evidence that the electric field component of PEMF exposure was affecting chondrocyte morphology.

A similar change in cell morphology was also observed by Blumenthal et al [112] after exposing rat bone marrow cells to a sinusoidal magnetic field with an AC strength of 0.5mT_{PP}, a DC strength of 0.25mT and a frequency of 1000Hz. Four days of exposure caused the detachment of pre-attached cells as well as prevented the attachment of cells not pre-attached. As the cells detached from the surface of the dish they changed from a stellate to a spherical morphology.

Ions such as calcium play an important role in regulating cell shape. Calcium is responsible for regulating changes in the actin filament meshwork that is present in the cytoplasm of chondrocytes [138]. According to the experimental results, cultured chondrocytes responded only to specific electromagnetic fields. Hence ions in transmembrane channels corresponding to cytoskeleton structure may be experiencing resonance, thereby causing the change to a spherical morphology.

Tang [139] outlined a model in which the chondrocyte will be deformed due to the presence of an electromagnetic field. From the electromagnetic modeling of a Helmholtz coil, the electric field induced by PEMF is non-uniform across the radius of the coil. Hence the electro-osmotic velocity under the induced electric field inside the chondrocyte will vary with the radial location. This will create a heterogeneous convection current affecting the potential distribution inside the chondrocyte. The overall effect will generate a mechanical stress, deforming the chondrocyte due to its flexible cell membrane.

Alternatively, the change in chondrocyte morphology may be a behavioural response to being placed in a particular environment. During PEMF exposure, this change in morphology was accompanied by a reduction in the average surface contact area of the chondrocyte to the culture dish. The largest decrease in area was observed when the cells modified their morphology from stellate to spindle to spherical; although decreases in area were still evident when the cells maintained their initial morphological classification. It is possible that PEMF exposure is harmful to chondrocytes and they respond by retracting their processes; thereby minimizing contact with the external environment. On the other hand, chondrocytes may favour the PEMF environment. In order for cells to enter mitosis, they must adopt a spherical morphology. Unfortunately, at the present time this study can not determine if the chondrocytes favour the PEMF environment. In this situation, the PEMF exposure is not directly affecting morphology but rather is the secondary effect of a behavioural response.

Chapter 4

4. Electromagnetic Modelling

This chapter discusses the modelling of the electromagnetic field produced by a pair of wire coils. In each of the models, the case of a single coil is presented, followed by the expansion to a coil pair. The first model is of the on-axis magnetic field produced at the midpoint between a coil pair. Although this situation is useful for the preliminary selection of electromagnetic parameters in the programmable PEMF generation system, its functionality is quite limited. As a result, the model is expanded to include an area of interest off the main axis of the coil. This allows the calculation of the magnetic field at all points within the spatial void of the coil pair. Lastly, the electric field induced by a ramping magnetic field is modelled for both the on-axis and off-axis cases.

4.1. *On-Axis Magnetic Field Produced at the Midpoint Between a Coil Pair*

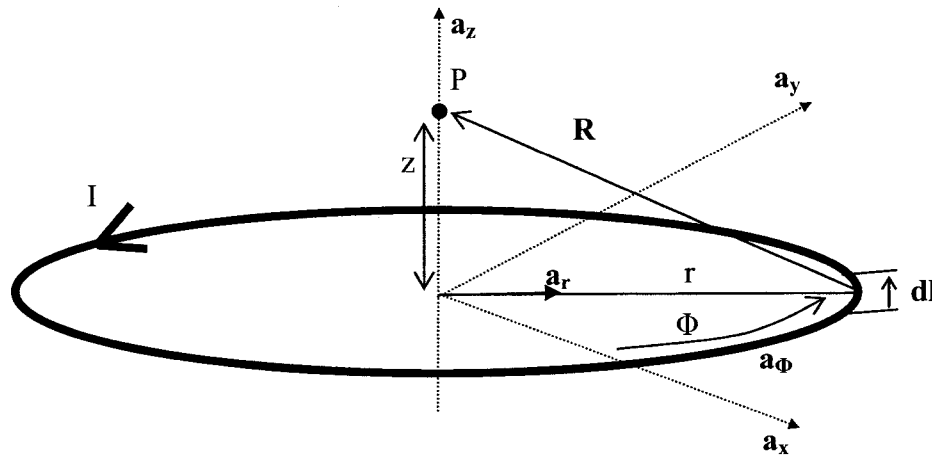


Figure 4-1: A single coil carrying current I , with specified on-axis point P

The simplest magnetic field model for a wire coil pair is one that provides the magnetic field strength at the midpoint between the coils. This fundamental model is very useful in

electromagnetic applications. The following derivation for the on-axis magnetic field produced at the midpoint between a coil pair is adapted from Cheng [140].

As shown in figure 4-1, the magnetic field at the on-axis point P from a single loop of wire of radius r, can be calculated according to the Biot-Savart Law (equation 4-1).

$$\begin{aligned} \mathbf{B} &= \frac{\mu I}{4\pi} \oint_C \frac{d\mathbf{l} \times \mathbf{R}}{R^3} \\ &= \frac{\mu I}{4\pi} \int_0^{2\pi} \frac{(\mathbf{a}_\phi r d\phi) \times (\mathbf{a}_z z - \mathbf{a}_r r)}{(z^2 + r^2)^{3/2}} = \frac{\mu I}{4\pi} \int_0^{2\pi} \frac{(\mathbf{a}_r r z d\phi - \mathbf{a}_z r^2 d\phi)}{(z^2 + r^2)^{3/2}} \end{aligned} \quad (4-1)$$

$$\text{where } \mu = 4\pi * 10^{-7}$$

The circular wire possesses cylindrical symmetry. Therefore the \mathbf{a}_r component of equation 4-1 is cancelled due to the element located diametrically opposite to $d\mathbf{l}$. Assuming an average radius of r, an approximation can be made for a wire coil with N turns. The resulting magnetic field can be approximated as the magnetic field from a single-turn coil, of average radius r, multiplied by turn factor N. It is also assumed that the coil has an infinitely small thickness so all the coil turns are located on the same horizontal plane. This horizontal plane is located in the middle of the coil. The result is the on-axis magnetic field strength for a single wire coil (equation 4-2). In reality, the radius of the coil will vary slightly depending upon the selected coil turn and the horizontal location of the turn within in the coil will also vary depending upon the coil thickness.

$$\begin{aligned} \mathbf{B} &= \frac{\mu I N}{4\pi} \int_0^{2\pi} \frac{(\mathbf{a}_z r^2 d\phi)}{(z^2 + r^2)^{3/2}} \\ &= \mathbf{a}_z \frac{\mu I r^2 N}{2(z^2 + r^2)^{3/2}} \end{aligned} \quad (4-2)$$

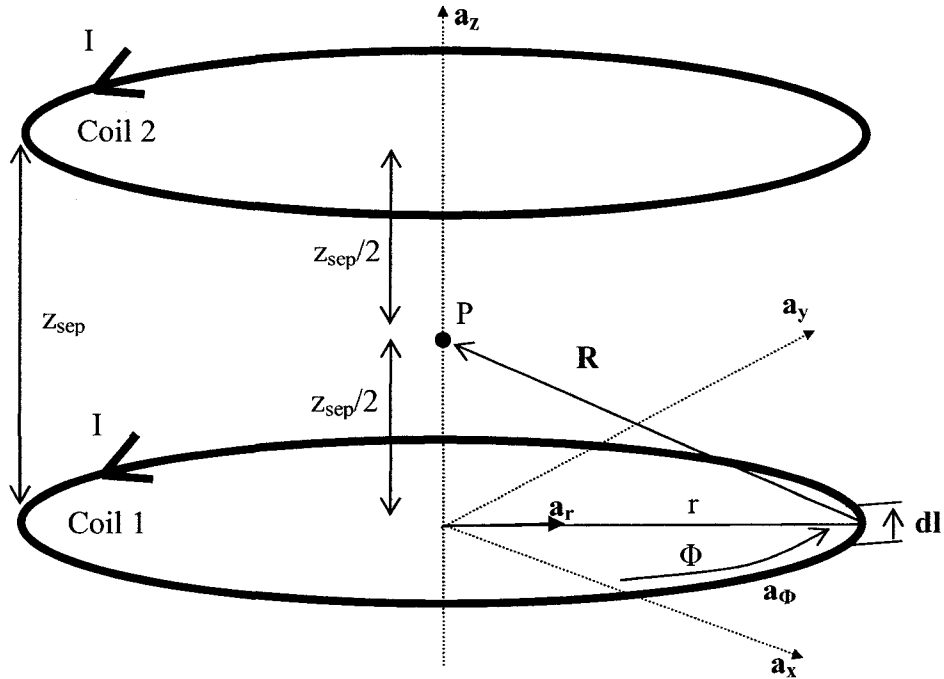


Figure 4-2: A coil pair carrying current I, with specified on-axis point P

This single coil model can be extended to a coil pair separated by distance z_{sep} . As shown in figure 4-2, the midpoint between the coils at which the magnetic field is to be calculated corresponds to a vertical distance of $z_{sep}/2$ from the bottom and top coil. This location is desired because during laboratory studies a chondrocyte culture dish will be placed at this location and exposed to electromagnetic fields. Theoretically, the resulting magnetic field at the midpoint between a coil pair is twice the magnetic field produced from a single coil. The on-axis magnetic field midpoint between a coil pair of N turns is thus modeled by equation 4-3.

$$\mathbf{B}_{total} = \mathbf{a}_z \frac{\mu I N}{r} \frac{1}{\left(1 + \left(\frac{z_{sep}/2}{r}\right)^2\right)^{3/2}} \quad (4-3)$$

Experimental validation showed that the magnetic field was less than doubled when moving from the single coil to coil pair situation. In fact, experimental results demonstrated an 85% increase in the measured magnetic field. This discrepancy can be

explained by both theoretical and experimental errors. Theoretically, the current applied to this model did not incorporate effects of self and mutual coil inductance. Self inductance increases the coil impedance with the frequency of the current waveform. Mutual inductance is the ability for a changing current flow through one coil to induce a voltage in a neighbouring coil. Since the measured magnetic field was less than expected, self and mutual inductance reduced the effective current flow through the coil set. As previously mentioned, this model also makes assumptions regarding the coil dimensions, which will degrade the accuracy of the resulting magnetic field. In terms of experimental errors, the two coils may not be exactly aligned, as specified in the model. A slightly different alignment of the coils will affect the resulting magnetic field. As well the use of the magnetic field sensor will affect the experimental validation. The placement of the sensor within the coil set, although versatile, will have some variability compared to theoretical calculations. Lastly, although its sensitivity is pre-specified, the calibration of the sensor may deviate depending upon its integration with external circuits and the ambient temperature. All of these above factors contribute to the discrepancy between theoretical and experimentally measured magnetic fields.

4.2. *Off-Axis Magnetic Field Produced by Two Coils*

The previously described on-axis magnetic field model, though useful in its simplicity does have its limitations. The model output is only valid for locations along the center axis of the coil pair. A more robust model, as developed by Smythe [141] calculates the magnetic field strength at all locations within the coil set. As with the previous model, this model assumes that a coil of N turns has an average radius of r , of which all coil turns are located on the same horizontal plane in the middle of the coil. In addition, this model assumes that current flow is known and effects of inductance, due to waveform frequency, are incorporated into the effective current strength.

The development of a magnetic field model encompassing the entire void between a pair of wire coils requires the use of the magnetic vector potential for a single coil (equation 4-4). As previously noted, the number of turns in each coil will increase the magnetic field strength by a factor of N , corresponding to the number of turns in each coil.

$$\mathbf{A} = \frac{\mu I N}{4\pi} \oint_C \frac{d\mathbf{l}}{R} \quad (4-4)$$

As shown in figure 4-3, the circular loop possesses symmetry in the cylindrical coordinate system. Hence the magnetic field at P is independent of the angle Φ at P . For convenience P was aligned with the x -axis ($\Phi = 0$). Source element $d\mathbf{l}$ acts in the \mathbf{a}_Φ direction but for computational simplifications will be defined in the Cartesian coordinate system (equation 4-5).

$$d\mathbf{l} = (-\mathbf{a}_x \sin \phi + \mathbf{a}_y \cos \phi) r d\phi \quad (4-5)$$

Examination of figure 4-3 shows that each source element $d\mathbf{l}$ at Φ has another symmetrically located element across the x -axis at $-\Phi$. When these symmetrical elements are paired they provide an equal contribution to the \mathbf{a}_y direction but cancel the contribution to the \mathbf{a}_x direction.

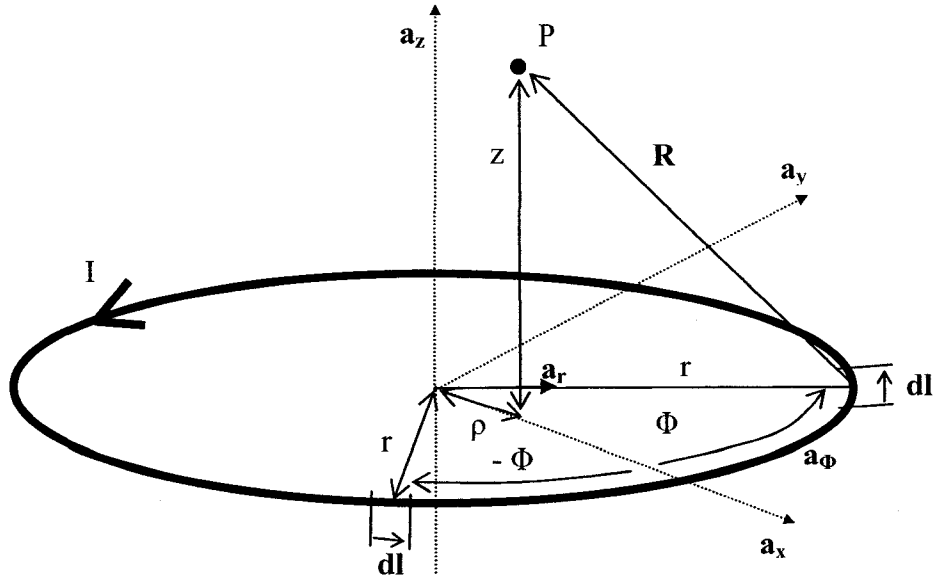


Figure 4-3: Off-axis magnetic field modeling of a single coil

Furthermore R can be defined using the law of cosines as the vector from point P to source element dl (equation 4-6).

$$R = (z^2 + r^2 + \rho^2 - 2r\rho \cos\phi)^{1/2} \quad (4-6)$$

Thus at any location P , the vector potential from a single turn of wire as shown in figure 4-2 can be computed (equation 4-7).

$$\mathbf{A} = \mathbf{a}_\phi \frac{\mu I N}{2\pi} \int_0^\pi \frac{r \cos\phi}{(r^2 + \rho^2 + z^2 - 2r\rho \cos\phi)^{1/2}} d\phi \quad (4-7)$$

In order to compute the integral component of the magnetic vector potential several substitutions are required. Using the following algebraic substitutions, $\phi = \pi + 2\theta$ and $\cos\phi = 2\sin^2\theta - 1$, prepares the magnetic vector potential for expression with elliptical integrals (equation 4-8). As previously mentioned, the magnetic field is independent of Φ , due to symmetry in the cylindrical polar coordinates. Therefore, since the exact value

of Φ , is not required, θ can be introduced for algebraic purposes. It is not a directly measurable quantity and as a result does not appear in figure 4-3.

$$\mathbf{A} = \mathbf{a}_\phi \frac{\mu INr}{\pi} \int_0^{\pi/2} \frac{(2 \sin^2 \theta - 1)}{[(r + \rho)^2 + z^2 - 4r\rho \sin^2 \theta]^{1/2}} d\theta \quad (4-8)$$

Formulas for complete elliptical integrals of the 1st and 2nd kind are provided as equations 4-9a, and 4-9b respectively. Notice that these equations are integrated over predefined limits for θ , therefore removing this variable from the resulting model. Elliptical integrals are beneficial to the computation of equation 4-8 since they are built into many kinds of mathematical software as easy to use functions.

$$K(k) = \int_0^{\pi/2} \frac{d\theta}{\sqrt{1 - k^2 \sin^2 \theta}} \quad (4-9a) \quad E(k) = \int_0^{\pi/2} \sqrt{1 - k^2 \sin^2 \theta} d\theta \quad (4-9b)$$

$$\text{where } k^2 = \frac{4r\rho}{(r + \rho)^2 + z^2} \quad (4-10)$$

Smythe [141] provides the solution to the vector magnetic potential using complete elliptical integrals (equation 4-11).

$$\mathbf{A} = \mathbf{a}_\phi \frac{\mu IN}{\pi k} \left(\frac{r}{\rho} \right)^{1/2} \left[\left(1 - \frac{k^2}{2} \right) K(k) - E(k) \right] \quad (4-11)$$

The magnetic field is defined as the curl of the vector magnetic potential (equation 4-12).

$$\mathbf{B} = \nabla \times \mathbf{A} \quad (4-12)$$

Computation of equation 4-12 in cylindrical coordinates yields the following magnetic field components (equation 4-13).

$$\begin{aligned}
\mathbf{B}_r &= -\frac{d\mathbf{A}_\phi}{dz} \\
\mathbf{B}_\phi &= 0 \\
\mathbf{B}_z &= \frac{1}{\rho} \frac{d}{d\rho} (\rho \mathbf{A}_\phi)
\end{aligned}
\tag{4-13}$$

Hence the resulting magnetic field possesses only a radial, \mathbf{B}_r , and vertical, \mathbf{B}_z , component.

Smythe completes the differentiation of equations 4-13, using four differentiation identities (equations 4-14). After the substitution of k (equation 4-10), the model for the magnetic field produced from a single wire loop is obtained (equations 4-15).

$$\begin{aligned}
\frac{dK}{dk} &= \frac{E}{k(1-k^2)} - \frac{K}{k}, & \frac{dE}{dk} &= \frac{E}{k} - \frac{K}{k} \\
\frac{dk}{dz} &= -\frac{zk^3}{4r\rho}, & \frac{dk}{d\rho} &= \frac{k}{2\rho} - \frac{k^3}{4\rho} - \frac{k^3}{4r}
\end{aligned}
\tag{4-14}$$

$$\begin{aligned}
\mathbf{B}_z &= \mathbf{a}_z \frac{\mu IN}{2\pi} \frac{1}{[(r+\rho)^2 + z^2]^{3/2}} \left[K + \frac{r^2 - \rho^2 - z^2}{(r-\rho)^2 + z^2} E \right] \\
\mathbf{B}_r &= \mathbf{a}_r \frac{\mu IN}{2\pi} \frac{z}{\rho[(r+\rho)^2 + z^2]^{3/2}} \left[-K + \frac{r^2 + \rho^2 + z^2}{(r-\rho)^2 + z^2} E \right]
\end{aligned}
\tag{4-15}$$

Equations 4-15 can be extended to the case of a coil pair separated by a distance z_{sep} , as shown in figure 4-4.

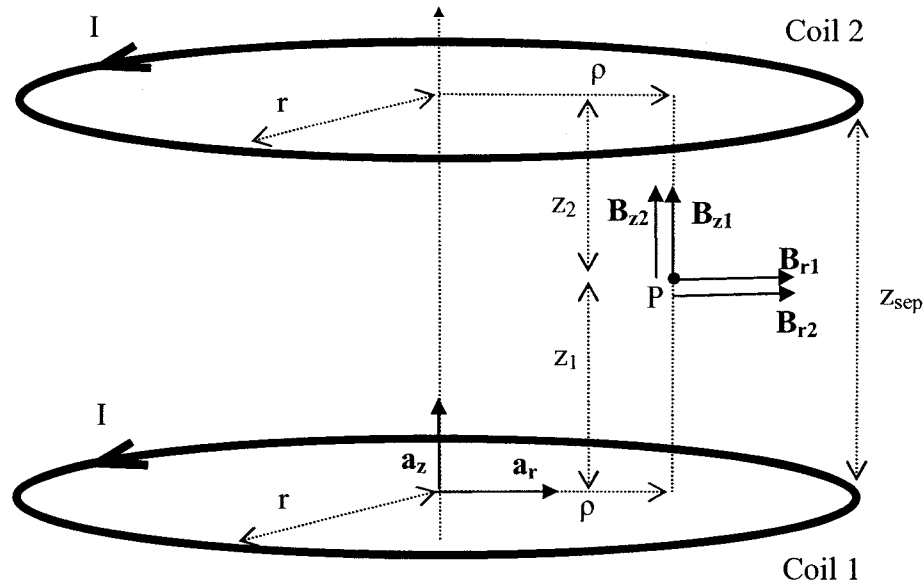


Figure 4-4: Off-axis magnetic field modeling of a coil pair

The magnetic field produced at location P by coil 1 and coil 2 can be computed by applying equation 4-15 to the arrangement of figure 4-4. When computing the magnetic field intensity at a location P between the coil pair, the resulting magnetic field is the vector sum of the magnetic field produced by each coil (equation 4-16). Notice that z_2 has negative intensity since we are investigating a region below coil 2.

$$\begin{aligned} \mathbf{B}_{rtotal} &= \mathbf{B}_{r1} + \mathbf{B}_{r2} \\ \mathbf{B}_{ztotal} &= \mathbf{B}_{z1} + \mathbf{B}_{z2} \end{aligned} \quad (4-16)$$

Application of equation 4-16 demonstrates the uniformity of the magnetic field throughout a vertical plane of the coil set. In this modeling situation, a coil pair of radius 6.5cm, 230turns, and separation of 7.5cm was delivered a current of $0.48A_{peak}$. Theoretically, the magnetic field across this vertical plane is represented in figure 4-5. An analysis of the field uniformity covered a spatial void in the middle in the coil set large enough to allow the stacking of three culture dishes. The area ranged from $x = -0.02m$ to $x = 0.02m$, and $z = -0.0135m$ to $z = 0.0175m$. Referring to a vertical slice at $x = 0m$, the magnetic field strength varied by 1.4%. Further from the middle of the coil set, along the

vertical slice at $x = 0.02\text{m}$ the magnetic field strength varied by 4%. These theoretical values were also validated experimentally. Actual measured magnetic fields demonstrated a variability of 1.4% and 3.2% along vertical slices at $x = 0\text{m}$ and $x = 0.02\text{m}$ respectively. The uniformity of the magnetic field was also assessed along horizontal slices. Both theoretical and experimental analyses demonstrate improved uniformity across horizontal slices. Theoretically, the variability in the magnetic field was 0.9% across horizontal slices in the area of interest for the coil set; experimentally, this value was 0.7%.

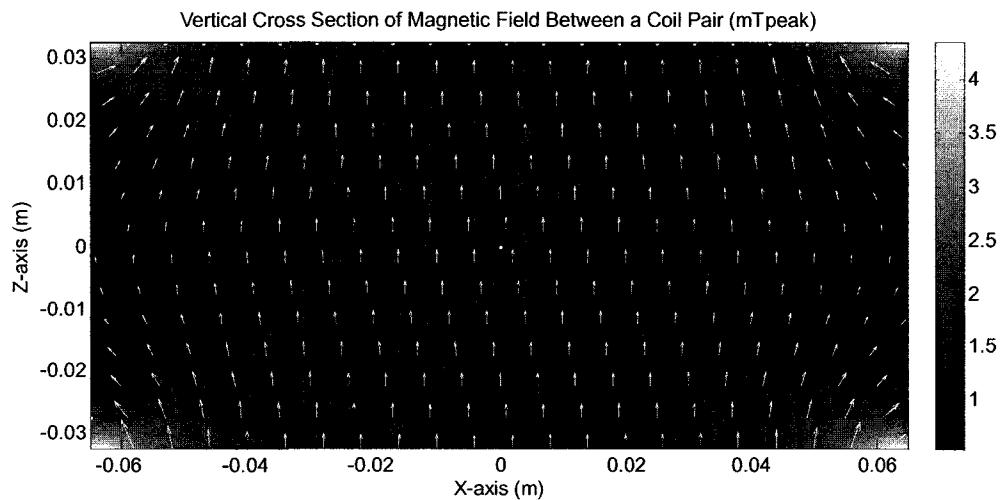


Figure 4-5: Theoretical magnetic field strength throughout a vertical plane of a coil pair. In this modelling situation, a coil pair of radius 6.5cm, 230turns, and separation of 7.5cm was delivered a current of $0.48A_{\text{peak}}$

In the above modeling situation, the variability of the magnetic field across a culture dish placed in the middle of the coil set was less than 1%. However, the uniformity of the magnetic field degraded significantly beyond the radius of a culture dish. For instance, if a vertical slice were obtained at $x = 0.04\text{m}$, theoretically the variability in the magnetic field increased to 18%; experimental results demonstrated 11.7%. This degradation in magnetic field uniformity also translated to horizontal slices across the void of the coil set. If the length of a horizontal slice was increased to $x = \pm 0.04\text{m}$, theoretically the variability in the magnetic field increases to 6.2%; experimental results demonstrated 4.5%.

In an experimental lab setting, a chondrocyte culture dish will be placed in a horizontal plane midpoint to the coil pair, since the magnetic field is most uniform at this location. In order to understand the exposure conditions it is vital to model the magnetic field across this horizontal plane. Hence, $z_1 = -z_2 = z_{sep}/2$ allowing for several simplifications to equations 4-16. Since $\mathbf{B}_{r1} = -\mathbf{B}_{r2}$, the resultant magnetic field in the \mathbf{a}_r direction is cancelled. The only remaining magnetic field is in the \mathbf{a}_z direction. Since $\mathbf{B}_{z1} = \mathbf{B}_{z2}$, the resultant magnetic field in the \mathbf{a}_z direction is twice that produced by a single coil. Hence, a model that determines the magnetic field strength across a horizontal plane midpoint to a coil pair has been developed (equation 4-17).

$$\mathbf{B}_{total} = 2\mathbf{B}_z = \mathbf{a}_z \frac{\mu IN}{\pi} \frac{1}{[(r + \rho)^2 + (z_{sep}/2)^2]^{3/2}} \left[K + \frac{r^2 - \rho^2 - (z_{sep}/2)^2}{(r - \rho)^2 + (z_{sep}/2)^2} E \right] \quad (4-17)$$

Application of equation 4-17 is demonstrated in figure 3-2a. In this modeling situation, a coil pair of radius 4.25cm, 120turns, and separation of 6.25cm was delivered a current of 1.81A_{peak}. The magnetic field in the horizontal plane located midpoint to the coil pair is thus represented by figure 3-2a. Theoretical modeling shows that the magnetic field strength decreases in a radial fashion from a maximum value of 3.1mT_{peak} in the center of the coil to approximately 1.3mT_{peak} at $x = 0.0425\text{m}$ corresponding to the edge of the coil set. Experimental validation demonstrated that actual magnetic field strengths were less than theoretical values. As previously discussed, this discrepancy in experimental and actual values could be due to a variety of factors in both the theoretical modelling and experimental validation. However despite these shortcomings, the radial decrease in magnetic field strength, as predicted by theoretical modeling, was confirmed in experimental validation.

4.3. *Electric Field Induced by On-Axis Magnetic Field Model*

The magnetic field employed in the PEMF studies is a time-varying ramp signal. This type of magnetic field will produce a constant electric field. There will only be points of discontinuity during the interval in which the magnetic field ramp is being reset. To solve for the electric field induced by a time-varying magnetic field use the integral form of Faraday's Law. (equation 4-18)

$$\oint_C \mathbf{E} \cdot d\mathbf{l} = -\frac{d}{dt} \int_S \mathbf{B} \cdot d\mathbf{s} \quad (4-18)$$

In the case of using the on-axis magnetic field model, it is assumed for the electric field calculation that the magnetic field is uniform across the entire radius of the coil. As previously noted, $\frac{d\mathbf{B}}{dt}$ is a constant due to a linearly changing magnetic field. Therefore the induced electric field strength is also constant. To determine the direction of the electric field use the right-hand rule. From this convention, if the magnetic field is oriented along the positive z-axis, the electric field will form concentric circles directed clockwise in the x-y plane. The induced electric field has a constant magnitude around a circle of specified radius. Using this knowledge, equation 4-18 can be rearranged to give the magnitude of the electric field induced from a ramp magnetic field. (equation 4-19)

$$E = \frac{dB}{dt} \cdot \frac{\rho}{2} \quad (4-19)$$

For each experimental protocol, the maximum magnetic field strength and pulse width of the waveform should be specified. Hence, a more practical calculation of the electric field is given in equation 4-20.

$$E[V/cm] = \frac{B_{total}[mT] \times radius[m]}{2 \times Pulse\ Width[msec]} \times \frac{1[m]}{100[cm]} \quad (4-20)$$

4.4. *Electric Field Induced by Off-Axis Magnetic Field Model*

Faraday's Law can also be used to solve for the induced electric field as determined from the off-axis magnetic field model. Contrary to the previous technique, it is not assumed that the magnetic field is constant across the x-y plane. As a result, this technique is more computationally intensive, however provides a more accurate representation of the induced electric fields. The following model computes the induced electric field in the x-y plane at the midpoint of the coil pair.

In the off-axis magnetic field modeling, the magnetic field strength was not uniform across the radius of the coil; it varied with ρ . As a result, an integration of the magnetic field must be performed using the results from the off-axis magnetic field model (equation 4-17). Using this knowledge, the induced electric field strength can be specified according to equation 4-21.

$$E_{field} = \frac{\int_0^{\rho} B_{total} r dr}{\rho \times Pulse\ Width} \quad (4-21)$$

This electric field model was simulated using a coil pair of radius 4.25cm, producing a ramp magnetic field of 3.1mT_{peak} at a frequency of 100Hz. The induced electric field at the plane midpoint to the coil set is shown in figure 3-2b. The electric field lines formed concentric circles around the central axis of the coil pair. Theoretically, the electric field strength was zero at the center of the coil and increased to a maximum of 0.048mV/cm at the edge of the coil. Unfortunately, experimental validation could not be performed on the electric field model. Since the induced electric fields are extremely small, insufficient SNR corrupted measurements by an electric field sensor.

Chapter 5

5. System Design

This chapter describes the design of a programmable PEMF generation system. This system will become a useful tool in future experiments exposing cultured chondrocytes to PEMFs. This system will allow the user to customize both the magnitude and timing aspects of the magnetic field, by specifying the AC and DC magnetic field strength, pulse width, duty cycle and pulse train of the ramp waveform. The operating range of this system is based upon a literature review of therapeutic devices using PEMF exposure for bone fractures and osteoarthritis, and experiments exposing *in vitro* cultured chondrocytes to PEMFs. As a result, this system has several requirements. It must be easy to configure the PEMF settings into the system, and it must produce a reliable output magnetic field according to these settings. The system should also be configurable over a range of PEMF settings appropriate for exposing cultured chondrocytes. Lastly, the system should be designed in a modular fashion to allow for the implementation of future improvements and recommendations.

5.1. Literature Review

Establishment of the operating range for the programmable PEMF generation system was based upon existing therapeutic devices using PEMF exposure for bone fractures and osteoarthritis, as well as experiments exposing *in vitro* chondrocytes to PEMFs. One bone healing system (EBI) uses a ramping AC magnetic field of $1.25\text{mT}_{\text{PP}}$, a DC magnetic field of 0.75mT , a pulse width of 0.23msec , a 7% duty cycle, and a pulse train containing seven ramp pulses. In regards to the treatment of osteoarthritis, PST has demonstrated therapeutic success using a quasi-rectangular magnetic field waveform of 1.25mT . PST uses a frequency range of 1Hz to 30Hz with a duty cycle greater than 50% [10]; corresponding to pulse width of 16.5ms to 1000ms . PEMF conditions that reduce the symptoms of osteoarthritis are not limited to the above settings. Clinical trials have been reported in literature using a quasi-rectangular or otherwise pulsating waveform with a wide parameter range for pulse width (0.25msec to 80msec), AC magnetic field

magnitude (0.04mT to 2.5mT) and duty cycle (15% to 80%). These clinical trials also reported the use of trains up to 20 pulses to deliver the electromagnetic signal [22,96,98,99].

Various animal studies have examined cartilage after exposure to ramp magnetic fields with reported improvements in morphology and expression of proteoglycan and type II collagen. [102-104]. These studies utilized AC magnetic field magnitudes from 0.1mT to 1.6mT, pulse widths from 1.3msec to 30msec, and duty cycles from 5% to 10%.

Many researchers have exposed *in vitro* cultured chondrocytes to a PEMF with reported changes in matrix synthesis and cell proliferation [105-108]. These *in vitro* cultured chondrocytes were exposed to either quasi-rectangular or otherwise pulsating electromagnetic fields with a wide range of pulse width (0.2msec to 1.3msec), AC magnetic field magnitude (0.2mT to 3.5mT) and duty cycle (3% to 68%). The electromagnetic parameters from this literature review established the operating range of the programmable PEMF generation system.

5.2. System Overview

The programmable PEMF generation system has been designed to generate a ramp magnetic field over a range of settings appropriate for the exposure of cultured chondrocytes. The ramping AC magnetic field strength ranges from 0.5mT_{PP} to 2.5mT_{PP} . The user can add a DC magnetic field bias ranging from 0mT to 1.25mT . The width of a single ramp pulse can range from 1msec to 35msec . The waveform can either be a continuous pulse train with 100% duty cycle, or be divided into packets ranging from 1 to 25 pulses with 10% to 95% duty cycle. A ramp magnetic field was chosen because it was used by a bone healing system (EBI), as well as several animal studies exposing cartilage to PEMFs.

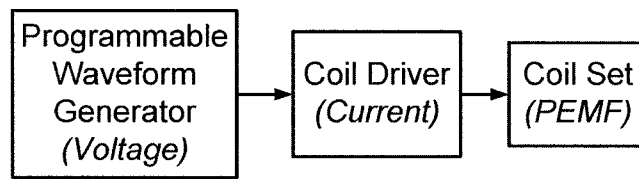


Figure 5-1: Block diagram of the programmable PEMF generation system

The generation of the PEMF signal requires three main modules: a programmable waveform generator, a coil driver and a coil set. A block diagram of this system is shown in figure 5-1. Each of these modules provides a vital role to the generation of the desired pulsed electromagnetic field and their design will be explained throughout this chapter. The programmable waveform generator requires both hardware and software design strategies to produce the initial voltage signal. This voltage signal is converted into a high output current by the coil driver. Delivering this current through the coil set will produce the user-specified PEMF.

5.3. Coil Set

This chapter provides justification for the coil set that best achieved the desired range of electromagnetic fields. The coil sets were evaluated for their current to magnetic field ratio, spatial uniformity and ability for their current flow to maintain a ramp waveform across the operational pulse width range of the programmable PEMF generation system. In the laboratory, there were two sizes of coils readily available for use with the programmable PEMF generation system (figure 5-2). These two coil sets, referred to as small and large, possess the following characteristics. The small coil set has an average radius of 4.25cm, 120 turns of 22 gauge copper wire, a measured resistance of 2.3 Ω , and inductance of 2.15mH. The large coil set has an average radius of 6.5cm, 230 turns of 22 gauge copper wire, a measured resistance of 5.6 Ω , and inductance of 13.3mH. In terms of dimensions, the large coil set is practical for the exposure of human limbs to electromagnetic fields. However, the small coil set is still sufficiently large for the exposure of culture dishes to an electromagnetic field. As will be explained, the small coil set was selected for use in the programmable PEMF generation system.

5.3.1. Magnetic Field Limitation

A vital component of choosing a coil set is determining its maximum magnetic field and spatial uniformity. The maximum magnetic field that can be produced by each coil set is restricted by two external factors. These two factors are the separation distance between the coil pair and the maximum current that can be delivered to each coil. As shown in equation 4-3, the magnetic field is also affected by the coil radius and number of coil turns. However, these are physical properties of the coil that can not be changed after fabrication.

The coil separation distance is regulated by a custom made Plexiglas stand. This stand supports a single culture dish at the mid-vertical distance between the coils. The separation distance for a coil set that will provide the most uniform magnetic field across the spatial void is specified as the coil radius; this special case defines a Helmholtz coil. The Plexiglas stand provides a separation distance of 6.25cm; just less than the Helmholtz separation for the large coil. Although this distance is larger than optimal for

the small coil set, as shown in figure 5-3, a relatively uniform magnetic field can still be achieved. Also, a larger separation distance allows easier access to the culture dish when it is positioned on the Plexiglas stand.

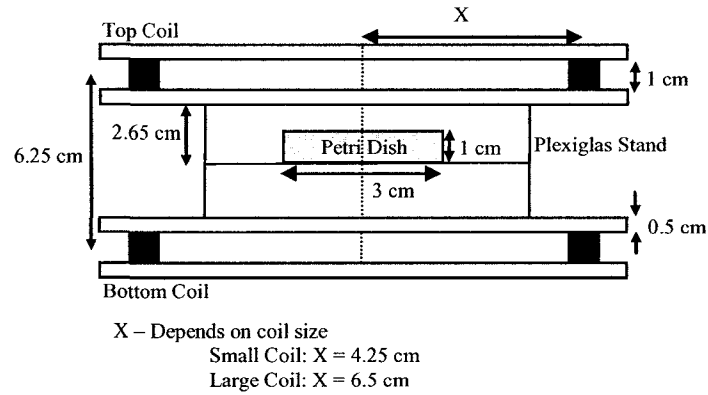


Figure 5-2: Arrangement of the coil set with the culture dish

The maximum current that can be delivered to each coil is $1.5A_{RMS}$; restricted by the $3A_{RMS}$ rating of the external power supply used for the coil driver. The larger the current that is delivered to the coil set the larger the power consumption. To prevent excessive coil heating, power consumption by the coil set will be limited to $1.5 W_{RMS}$. This rating was based upon the output characteristics of the EBI Bone Healing System. As a result, this power consumption corresponds to a maximum current rating of $1.4A_{peak}$ and $0.9A_{peak}$, for the small and large coil sets respectively, when a ramp signal is applied. Previous experimental investigations have demonstrated that excessive coil heating occurs at power consumptions larger than $6W_{RMS}$. The heat released by the coils undesirably warms the culture dish placed in the coil set. As a result, the culture medium temperature increases from the incubated temperature of $37^{\circ}C$; thereby killing the cell culture.

Using the limited power consumption and equation 4-3, the maximum magnetic field that can be achieved by the small and large coil sets is $2.6mT_{pp}$ and $2.9mT_{pp}$ respectively. As a result, both coil sizes can produce the magnetic field strength required by the programmable PEMF generation system. However, the large coil set requires less current to achieve the same magnetic field strength as the small coil set.

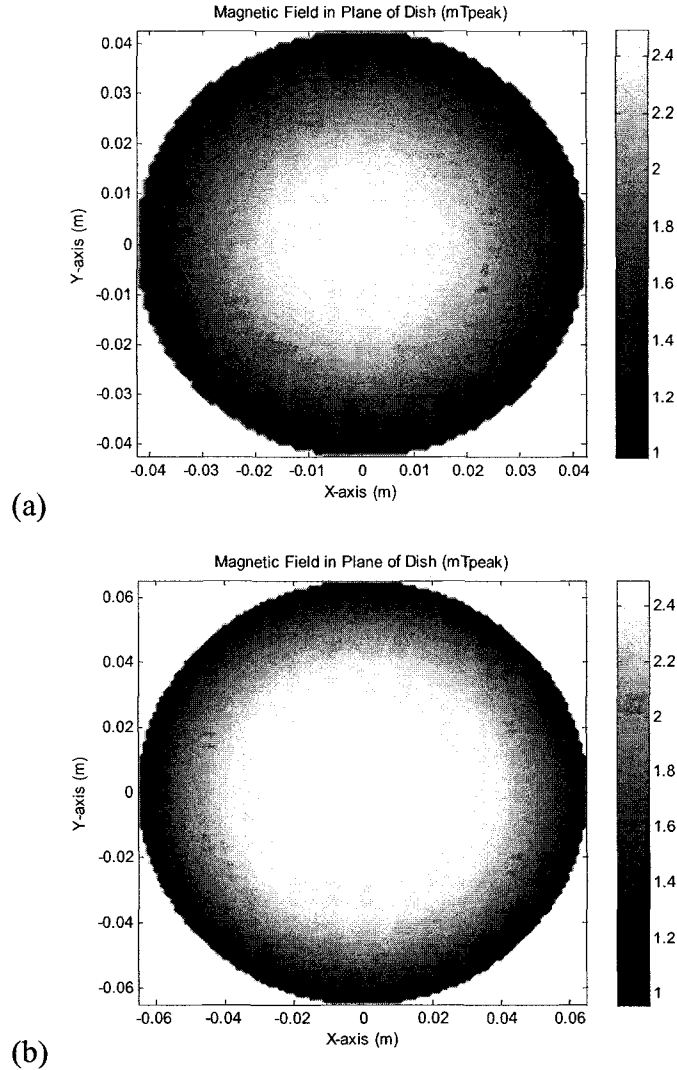


Figure 5-3: Magnetic field in the plane of the culture dish for the (a) small and (b) large coil set

Limiting to the operating range of the programmable PEMF generation system, a 2.5mT_{PP} magnetic field can be modeled in MATLAB using equation 4-17. Generation of this magnetic field using the small or large coil set requires a current of 1.35A_{PP} or 0.77A_{PP} respectively. The output of this simulation, shown in figure 5-3, demonstrated the uniformity of the magnetic field in the plane of the culture dish for the two sizes of coil set. As predicted, the magnetic field strength was less uniform for the small coil than the large coil. The magnetic field strength was strongest at the center of the coil set and

decreased at an increased radial location. Limiting to a 1.5 cm radius in the center of the coil, corresponding to the radius of the culture dish, the magnetic field strength decreased by 5% in the small coil set but remained constant for the large coil set.

5.3.2. Simulation of Current Flow through a Coil Set

According to the analysis performed so far, it would appear that the large coil set is the better choice since it can generate the required magnetic field strength with a reduced current demand. However the large coil has a greater inductance than the small coil. Inductance will reduce the maximum rate of current change possible through the coil as well as increase the impedance of the coil set.

In order to evaluate the waveform performance of the coil sets, the output characteristics of the coil driver are required. Although the coil driver will be fully explained in chapter 5-4, for the purposes of this simulation, it is necessary to know the output resistance (1Ω and 4Ω) and capacitance ($0.22\mu\text{F}$) that is associated with the driver circuit. A PSPICE simulation was created, according to the schematic of figure 5-4, to assess the transient behaviour of the coil set connected to the coil driver. As a result, the effect of coil inductance on the ability of the coil current to match the desired ramp waveform was assessed at the minimum and maximum pulse width settings of the programmable PEMF generation system.

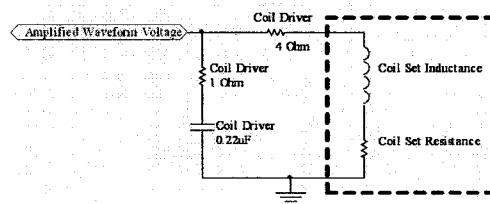


Figure 5-4: Circuit model of the coil driver connected to a coil set

The stimulation voltage for this circuit was a ramp waveform of variable pulse width. The magnitude of this voltage was selected so that if the effect of inductance were ignored, the current through the coil set would establish a $1A_{PP}$ ramp signal. This corresponds to a stimulation voltage of $6.3V_{PP}$ and $9.6V_{PP}$, for the small and large coil set respectively.

Simulations were performed using pulse widths of 1msec and 35msec to represent the operating limits of the programmable PEMF generation system. As will be discussed in chapter 5-5, a reset time corresponding to 5% of the ramp time is required for the programmable waveform generator to initialize for the next ramp signal. Incorporation of this reset time into the simulation results in a waveform period of 1.05msec and 36.75msec, for pulse widths of 1msec and 35msec respectively.

Simulations were first performed using the maximum pulse width of 35msec for the small and large coil set. Large pulse widths correspond to a low operating frequency, which in turn minimizes the effect of inductance on circuit impedance. Large pulse widths also provide more time for the current to flow through the coil, as to not be restricted by the coil inductance. As shown in figure 5-5, the current flow through both the small and large coil set was able to maintain the overall ramp waveform. For the small coil set, the current established an effective ramp signal of approximately 960mA_{pp}; for the large coil set, the current established an effective ramp signal of approximately 854mA_{pp}. Ideally, if coil inductance was not affecting impedance, the ramp signal would have a strength of 1A_{pp}. In terms of waveform period, both coil sets exhibited a time of 36.75msec. However, for the small coil set, the effective reset time was 8% of the ramp time; for the large coil set, the effective reset time was 17% of the ramp time. Compared to the ideal values, the performance of the small coil set was better than the large coil set at a pulse width of 35msec. Yet, the performance of the large coil set was still acceptable.

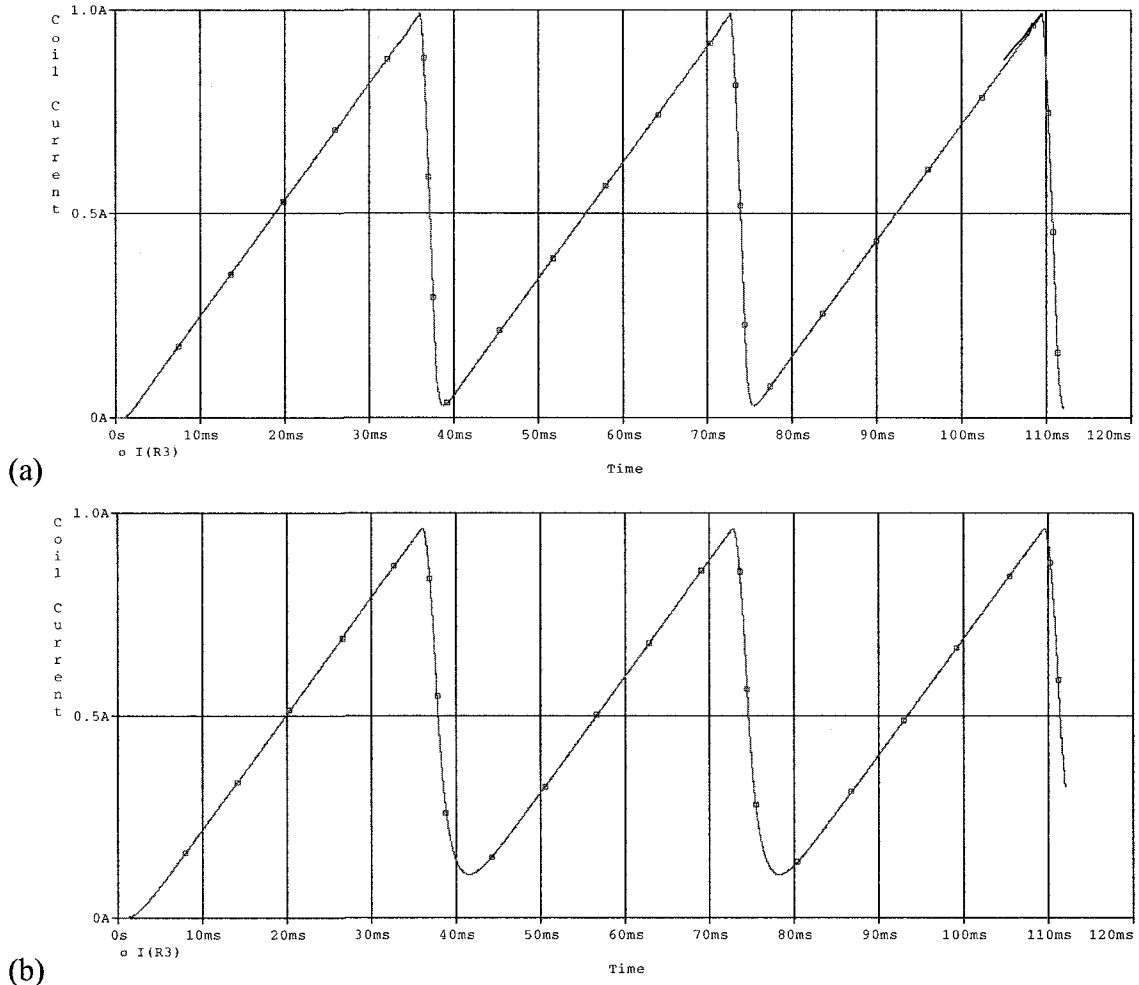


Figure 5-5: Coil simulation using a 35msec ramp pulse width for (a) the small coil and (b) the large coil

Simulations were also performed using the minimum operating pulse width of 1msec for the small and large coil set. Small pulse widths correspond to a high operating frequency. Due to the inductance of the coil, the effective impedance of the small coil increased to 13.7Ω and the large coil to 83.7Ω . This increase in impedance reduces the coil current and the resulting magnetic field strength that can be achieved by the coil set. Using a short pulse width also reduces the allotted time for the current to ramp and reset in the coil, increasing the likelihood of restriction by the coil inductance. As shown in figure 5-6, the performance of both the small and large coil set was reduced when using a 1msec pulse width. This effect was most evident in the large coil simulation since the current was unable to maintain the ramp waveform. The allotted reset time for the coil current

was too short, causing the development of a staircase waveform rather than a ramp waveform. The effective magnitude of this staircase waveform was 147.5mA_{pp} , with a reset time of 48%. On the other hand, the effect of coil inductance was reduced in the small coil simulation, but still evident. The small coil set was able to maintain the overall ramp waveform, but with a reduced magnitude. The current through the small coil established an effective ramp signal of approximately 349mA_{pp} , with a reset time of 63%.

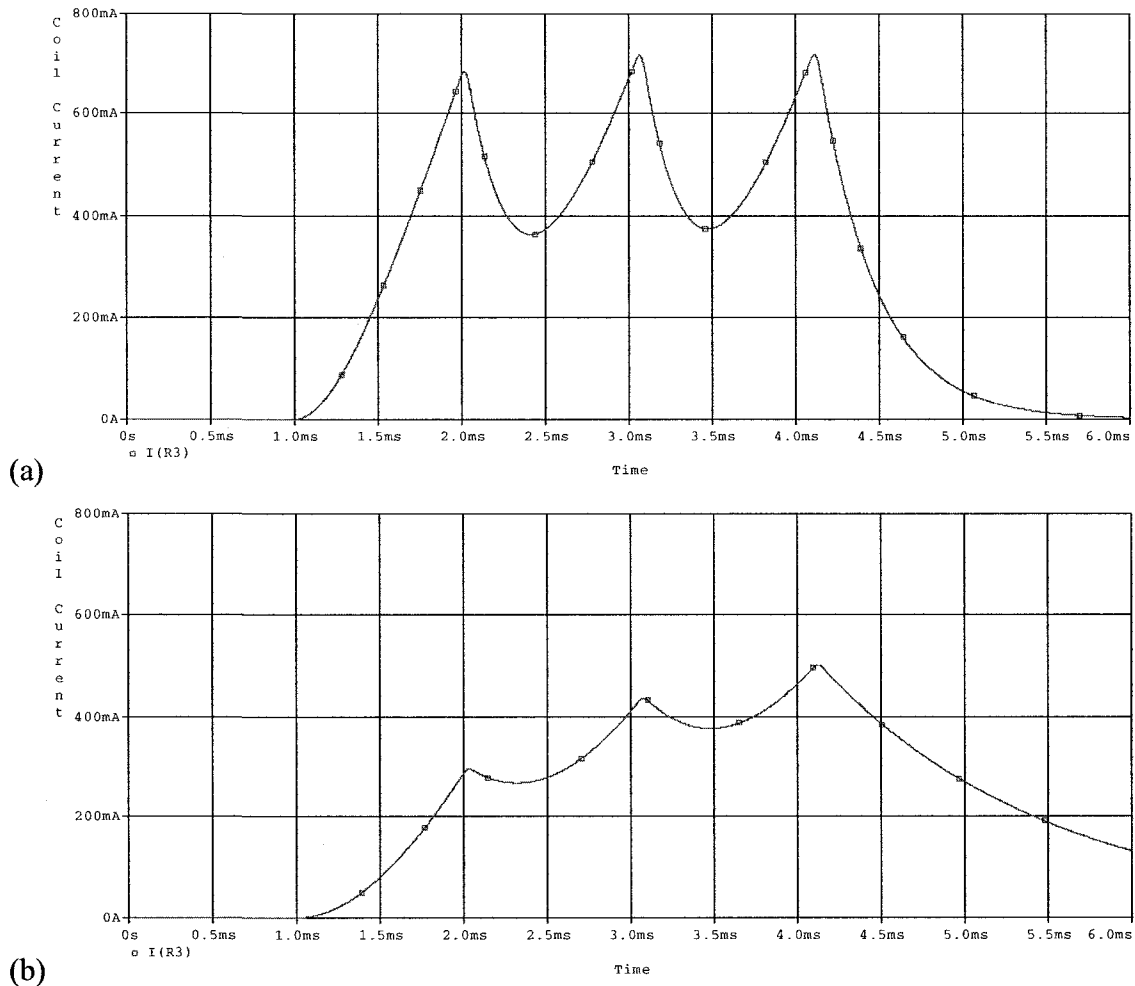


Figure 5-6: Coil simulation using a 1msec ramp pulse width for (a) the small coil and (b) the large coil

From these simulations, it is evident that the small coil set exhibits better timing performance than the large coil set. For this reason, the small coil will be selected over the large coil for use in the programmable PEMF generation system. The small coil can

maintain current flow as a ramp waveform over the operational pulse width of the proposed system. Although the altered ramp-reset ratio of the current signal can not be accommodated for, the effect of reduced ramp amplitude at small pulse widths can be accommodated for by scaling the magnitude of the output current to the coil set.

In summary, the coil set chosen for the programmable PEMF generation system had an average radius of 4.25cm, containing 120 turns of 22 gauge copper wire wrapped around a high density plastic spool. When this coil set is connected to the PEMF generating system, it will produce ramping magnetic fields ranging in strength from $0.5mT_{pp}$ to $2.5mT_{pp}$. Although the performance of this coil set does degrade at shorter pulse widths, it was the best choice of the two available coil sets. Testing of the programmable PEMF generation system in chapter 6, indicated that for the small coil set, coil inductance significantly decreased the performance of the system at pulse widths less than 5msec.

5.4. *Coil Driver*

The coil driver converts the output voltage signal from the programmable waveform generator into a current that can be used by the coil set. As a result, the current flow through the coil set will resemble the voltage signal produced by the programmable waveform generator. The coil driver consists of two sections: the power management module and the voltage-to-current conversion circuit. The power management module produces the supply rails required for the cooling fan and high current operational amplifiers. The voltage-to-current conversion circuit converts the voltage signal from the programmable waveform generator into a high output current for the coil set. Schematics for this coil driver circuit can be found in appendix A.

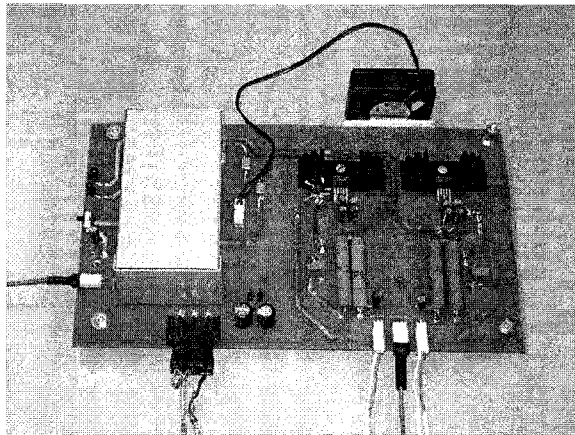


Figure 5-7: The coil driver

Shown in figure 5-7, the coil driver has not been enclosed in a case to maximize heat dispersion from the components. However, the onboard power management module is enclosed by an aluminum casing to shield the analog conversion circuitry from its electromagnetic interference. The coil driver measures approximately 6" x 10" x 2".

5.4.1. Power Management Module

The onboard power management module is designed to produce the required $\pm 12\text{V}$ and $+5\text{V}$ supply rails for the coil driver, as outlined by figure 5-8. Fuses have been incorporated into the $\pm 12\text{V}$ supply rails to prevent overloading of the circuit beyond maximum specifications. Visual confirmation that the $\pm 12\text{V}$ supply rails are active is provided by two light emitting diodes (LEDs). An external power supply is used to provide an input voltage, in the range of $+8\text{V}$ to $+15\text{V}$, to this module. The power cable used to connect the external supply to the coil driver is filtered using large capacitors to remove electromagnetic interference from the external environment. As will be discussed in chapter 5-7, the maximum current demand for the coil driver is approximately $1.77\text{A}_{\text{RMS}}$. This requirement is satisfied by the 3A_{RMS} rating of the external power supply.

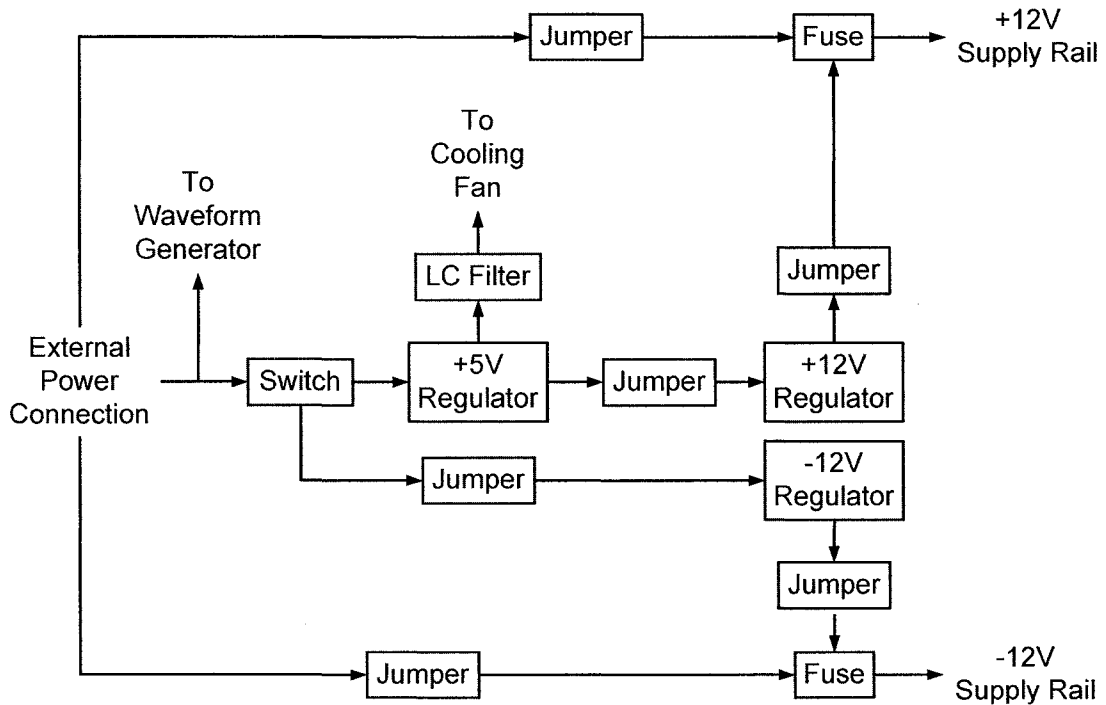


Figure 5-8: Overview of the coil driver power management module

The $\pm 12\text{V}$ supply rail is required for the power operational amplifiers in the voltage-to-current conversion circuit. Unfortunately the selected $+12\text{V}$ regulator (PT6674, Texas

Instruments) and -12V regulator (PT6643, Texas Instruments) do not have a common input voltage range. Therefore an additional +5V supply rail provides the input voltage to the +12V regulator. This +5V supply rail also powers the cooling fan for the conversion circuit.

The +5V supply rail is produced using a low-dropout voltage regulator (KA278R51, Fairchild Semiconductor). High current capability is required for this regulator because it serves as the supply rail to the +12V regulator. As a result, it sources up to $2A_{RMS}$ of current for the coil set. The operation of this regulator requires large capacitors to filter the input and output supply rail.

Since the voltage-to-current conversion circuit, needs to produce up to $0.78A_{RMS}$ of current per coil, proper air flow across the heat sinks and resistors are required to prevent overheating. Unfortunately, this fan produces high frequency noise on the +5V supply rail which could be coupled onto the analog input signal of the coil driver. For this reason, a low-pass inductor-capacitor filter (LC), with a cut-off frequency of 300kHz, is used to condition the +5V supply rail used by the fan.

The power management module uses Integrated Switching Regulators to produce the +12V (PT6674, Texas Instruments) and -12V (PT6643, Texas Instruments) supply rails from a positive input voltage. These integrated regulators only require input and output supply rail capacitors to stabilize operation. These regulators are also capable of sourcing $2A_{RMS}$ of current, at an efficiency of 85%. When the programmable PEMF generation system is configured for the maximum ramp magnetic field of $2.5mT_{PP}$, each coil consumes a current of $1.35A_{PP}$. Since total current consumption of the coil set is split between the $\pm 12V$ supply rails, regulator output current is only $0.78A_{RMS}$ per rail.

During the implementation of this power management module, the $\pm 12V$ onboard regulators did not perform to specifications. Fortunately, a bypass system was incorporated into the design, as shown in figure 5-8, using jumpers to select whether the $\pm 12V$ supply rails are sourced from the onboard regulators or from the external supply. As a result, the $\pm 12V$ supply rail can be delivered directly from an external power supply.

5.4.2. Voltage-to-Current Conversion

The voltage-to-current conversion circuit converts the input voltage signal from the programmable waveform generator into an output current that can be used by the coil set to generate a magnetic field. There are two channels on the conversion circuit, each with the same design, to power the two coils.

This design is based on the use of a power operational amplifier (LM675, National Semiconductor). Although there are several power amplifiers available, the chosen device must be compatible with a maximum operating current of $1.35A_{PP}$, a peak output voltage of 8.5V and minimum ramp pulse width of 1msec. The power operational amplifier also has thermal protection circuitry to power-down the integrated circuit (IC) while die temperatures exceed the designated limits.

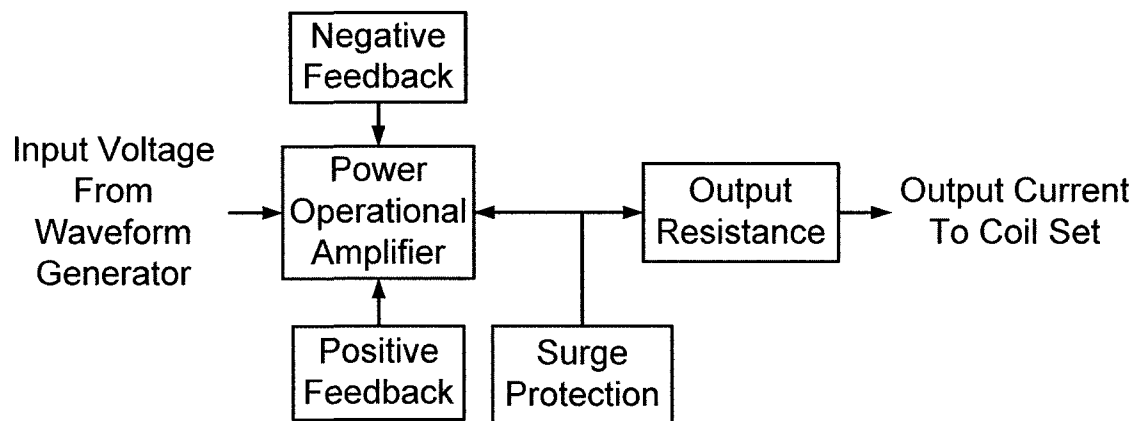


Figure 5-9: Overview of the coil driver voltage-to-current conversion circuit

To prevent extremely high die temperatures requires the use of a heat sink. Under the maximum output conditions, power consumption by the power operational amplifiers is approximately 12W. For this design, a horizontal mounted heat sink, compatible with the TO-220 packaging of the LM675, was chosen with a thermal resistivity of $9^{\circ}C/W$. A cooling fan is positioned to provide air circulation across the fins of the heat sink. As well, the other resistive components of this conversion circuit are positioned on the printed circuit board to take advantage of the air circulation provided by the cooling fan.

The $\pm 12\text{V}$ supply rails are filtered prior to their use by the power operational amplifiers. A large and small capacitor is used in parallel for each supply pin to filter out low and high frequency interference respectively.

The voltage-to-current conversion circuit, shown in figure 5-9, uses both negative and positive feedback. The use of negative feedback produces an inverting amplifier with ten times gain. Amplification of the input voltage signal is necessary to develop large output currents for the coil set. The use of positive feedback adds hysteresis to the circuit for improved noise immunity. Positive feedback can also improve the response time of the voltage-to-current conversion circuit and its effectiveness with rapidly changing input signals.

The output pin of the power operational amplifier is provided with start-up surge protection. When an input signal is first applied to the voltage-to-current conversion circuit, start-up transients could exist on the output pin. Allowing a resistor-capacitor arrangement to quickly charge and discharge will remove these transients and stabilize the resulting signal on the output pin.

The final component of the voltage-to-current conversion circuit is the establishment of a large output current for the coil set, as predicted by equation 5-1. Illustrated in figure 5-4, the total output resistance is the series addition of the onboard 4Ω resistor and the connected coil set resistance of 2.3Ω ; therefore $R_{out} = 6.3\Omega$. Lastly, the output voltage can be related to the input voltage according to the theoretical gain of the inverting amplifier circuit.

$$I_{out} = \frac{V_{out}}{R_{out}} \approx 1.6[A/V] \times V_{in} \quad (5-1)$$

Application of the above equation to the operating conditions of the programmable PEMF generation system yields the following requirements for the input voltage signal.

According to equation 4-3 the theoretical output current delivered to the coil set ranges from $0.27A_{PP}$ to $1.35A_{PP}$, for an AC magnetic field of $0.5mT_{PP}$ and $2.5mT_{PP}$ respectively. Relating to equation 5-1, this corresponds to a theoretical input voltage range of $169mV_{PP}$ to $844mV_{PP}$ respectively. As a result, a theoretical relationship between the input voltage and magnetic field is determined as in equation 5-2.

$$V_{in} = 337.6[mV / mT] \times \text{Magnetic Field} \quad (5-2)$$

As will be discussed in chapter 5-8, preliminary testing of the coil driver connected to the coil set yielded a different relationship between the input voltage and output magnetic field. The relation of equation 5-3 was experimentally obtained and will be used as the basis for the design of the programmable waveform generator.

$$V_{in} = 181.6[mV / mT] \times \text{Magnetic Field} \quad (5-3)$$

Equation 5-3 implies that an AC magnetic field range of $0.5mT_{PP}$ to $2.5mT_{PP}$ requires an input voltage range of $91mV_{PP}$ to $454mV_{PP}$ to the coil driver.

5.5. Programmable Waveform Generator

The design of the programmable waveform generator to create the user-specified signal involved both hardware and firmware strategies.

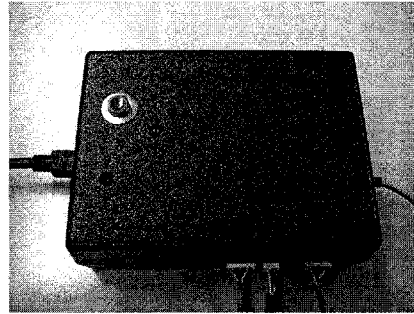


Figure 5-10: The programmable waveform generator

5.5.1. Hardware

The programmable waveform generator consists of six main modules to regulate characteristics of the voltage signal representative of the user-specified magnetic waveform. These modules are the universal serial bus (USB) interface, power regulation, microcontroller, AC signal generation, DC signal generation, and dual channel voltage output. A block diagram of this system is represented in figure 5-11. Schematics for all of the circuits comprising the programmable waveform generator can be found in appendix B. The programmable waveform generator is contained within a plastic case measuring 3.25" x 4.38" x 1.5", shown in figure 5-10, modified to allow LEDs, push buttons, switches and connection ports to be externally accessed.

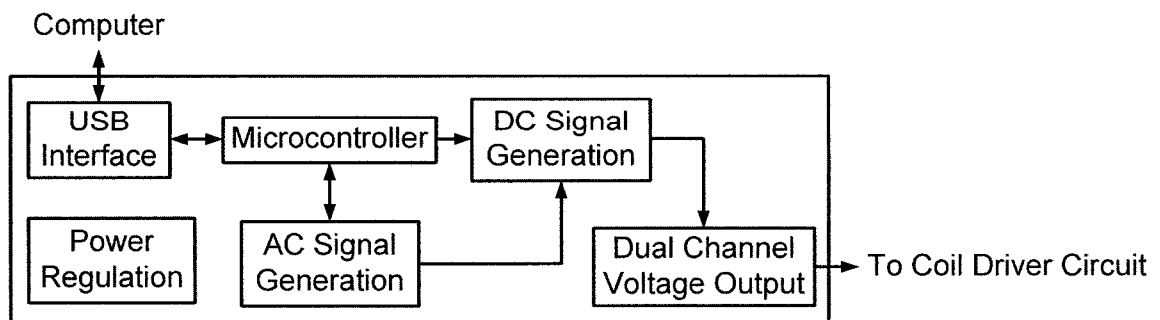


Figure 5-11: Block diagram of the programmable waveform generator

5.5.1.1. USB Interface

Communication using the USB was chosen because it is a common interface with computers. A USB-UART converter IC (FT232R, FTDI) translates the information sent and received between an external computer and the microcontroller onboard the programmable waveform generator. As a result, the user can easily program their desired PEMF characteristics into the programmable waveform generator. As a safety feature, an LED is used to indicate when communication is present on the USB port, so the system is not unplugged during a data transfer. This USB-UART converter IC also provides a control signal to the microcontroller indicating when the system is connected to a computer. This allows the microcontroller to swap between program modes depending upon the status of the USB port connection.

The USB circuit is self powered at +5V, the standard voltage of a USB port. This raw USB port power is conditioned by an LC low-pass filter before it is used by the circuit. A small inductor is used for noise filtering and prevention of high frequency current spikes, while the capacitor removes the voltage spikes.

Although the FT232R itself is powered from a +5V supply, it does provide an onboard +3.3V supply rail. When the system is connected to the USB, the rest of the programmable waveform generator circuit can be powered by this +3.3V supply rail. Hence, communication can exist between the FT232R and the microcontroller. The USB port can source a maximum of 500mA_{RMS}. As will be shown by the current analysis of chapter 5-7, the programmable waveform generator only sinks 41.8mA_{RMS}. This low current requirement is important if the system is connected to a 4-port USB hub, whereby the current source is reduced to 125mA_{RMS}.

5.5.1.2. Power Regulation

The programmable waveform generator is designed for a $\pm 3.3\text{V}$ supply. Using a low supply voltage reduces the power consumption of the system. The power regulation module can be sourced by two methods; either from the USB-UART converter IC or from an external power supply. The external power supply could either be a battery pack or a feed from the coil driver. The latter configuration, as shown in figure 5-12, limits the transmission of large current through cabling. As a result, the coil driver receives the main power feed from the external supply, and delivers a low power feed to the programmable waveform generator. In the future, a battery pack could be installed to self-power the programmable waveform generator. Whenever a signal is delivered across a cable, it is likely to be coupled with 60Hz noise from the surrounding environment; therefore a capacitor is used to filter out noise at the power connection.

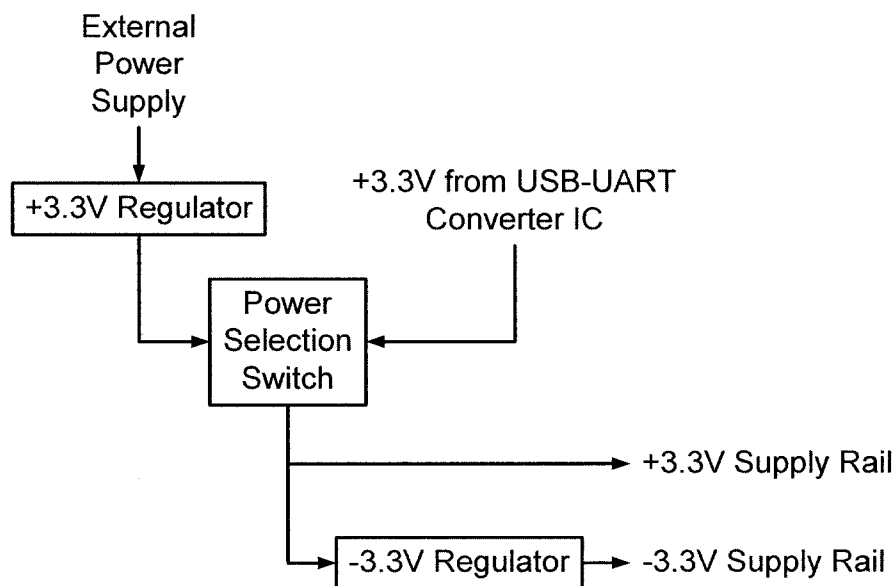


Figure 5-12: Overview of programmable waveform generator power regulation

The external supply voltage is regulated to $+3.3\text{V}$ using a linear voltage regulator (TPS76133, Texas Instruments). This regulator can provide up to $100\text{mA}_{\text{RMS}}$ of current; sufficient for the $26.8\text{mA}_{\text{RMS}}$ demand of the programmable waveform generator, when it

is not connected to a computer. Lastly, the output voltage noise is specified to be less than $190\mu\text{V}_{\text{RMS}}$. Low power supply noise is important in the design of digital circuits for the protection of the digital components. The operation of this regulator requires a capacitor on the input pin to filter out high frequency components that could damage the regulator electronics. A capacitor is also required on the output pin to stabilize the internal control loop regulating the output voltage.

The power source selection for the programmable waveform generator is performed using a power switch (TPS2105, Texas Instruments). As shown in figure 5-12, this power switch can choose from two input sources: the +3.3V supply from the USB-UART converter IC or the external +3.3V regulated power supply. The system is configured to use power from the USB port whenever it is present; otherwise the system will use the external +3.3V supply. In case switching occurs between input signals with a large differential, a large capacitor stabilizes the surge on the output pin. During application of the programmable PEMF generation system, the USB port power will only be present when the user is updating the configuration settings. When the programmable PEMF generation system is producing an electromagnetic field, the programmable waveform generator will not be connected to a computer, so the external +3.3V power supply is required. Regardless of the power source used, an LED connected to the output of the power switch visually indicates whether the +3.3V supply rail is active.

To implement the full functionality of the programmable waveform generator, a charge pump voltage inverter (TPS60401, Texas Instruments) generates a -3.3V supply rail from the +3.3V output of the power switch (figure 5-12). The implementation of the charge pump principle for the voltage inversion requires three external capacitors. Although this voltage inverter can only source 60mA_{RMS} , it is sufficient to meet the current consumption of the programmable waveform generator. Similar to the +3.3V supply rail, a LED provides visual confirmation that the -3.3V supply rail is active.

5.5.1.3. *Microcontroller*

A microcontroller (ATmega168V, Atmel) was used to control the functionality of the programmable waveform generator. Outlined in figure 5-13, this microcontroller provides a large selection of input/output (I/O) pins and onboard features to interface with external components. These external components are the clock, microcontroller programmer, USB-UART converter IC, and the AC and DC signal generation circuits.

Microcontroller	
USART	Interrupts
EEPROM	Flash Memory
SRAM	SPI
16-bit Timer	I/O Pins

Figure 5-13: Overview of programmable waveform generator microcontroller

In terms of memory allocation, this microcontroller features 512 bytes of onboard electrically erasable programmable read-only memory (EEPROM) to allow the user to save configuration data, 16kbytes of flash program memory, and 1kbyte of static random access memory (SRAM) data memory.

The microcontroller has several external interfaces to regulate its functionality. First, the microcontroller is run by an external clock oscillator at a frequency of 3.6864MHz. Second, the microcontroller can be programmed using the serial peripheral interface (SPI) with an external programming module that interfaces with a computer. Rather than being overwhelmed by instruction based code, the ATmega168V can be programmed using the C programming language. This system also uses external pin interrupts to control the execution of firmware within the microcontroller.

The microcontroller also has several external interfaces to regulate other devices. The microcontroller uses USART to interface with the USB-UART converter IC. In order to control the AC and DC signal generation circuits, the microcontroller must control

several digital potentiometers, a 3-to-8 multiplexer, and an analog bus switch. It also must provide the input voltages to the AC and DC signal generation circuits. The control of the digital potentiometers is via the SPI. The regulation of a 3-to-8 multiplexer requires three control signals sourced from I/O pins on the microcontroller. The microcontroller also requires an onboard 16-bit timer with pulse width modulation to control I/O pins for the analog bus switch and input voltages to the AC and DC generation circuits. The programmable waveform generator currently uses 18 of the 23 available I/O pins on this microcontroller. There are also 8 analog-to-digital converter (ADC) pins to allow for electric or magnetic field probe interaction in future designs.

5.5.1.4. AC Signal Generation Circuit

The AC signal generation circuit produces the user-specified voltage ramp. This module consists of two sections, as shown in figure 5-14. The first section establishes the input voltage to the active integrator. The second section is an active integrator circuit that produces the AC component of the ramp waveform. According to equation 5-3, if the AC magnetic field ranges from $0.5mT_{PP}$ to $2.5mT_{PP}$, the output voltage of the programmable waveform generator must vary from $91mV_{PP}$ to $454mV_{PP}$. This ramp voltage signal must also have a selectable pulse width ranging from 1msec to 35msec.

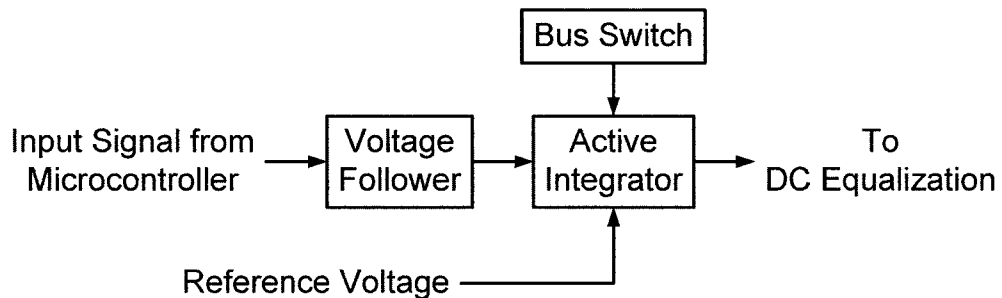


Figure 5-14: Overview of programmable waveform generator AC signal generation circuit

The input voltage to the active integrator is regulated by the microcontroller to toggle between 0V and +2.0V in order for the system to achieve its specifications for the AC waveform. After the establishment of this input voltage, a voltage follower isolates the

resistance required in the active integrator. As well, this buffer protects the delicate I/O pins of microcontroller from the activity of integrator circuit.

The active integrator is designed around an operational amplifier (LMC6482, National Semiconductor). The selected operational amplifier (op-amp) must handle, during maximum operating conditions, an output ramp voltage of magnitude 454mV_{pp} with a 1msec pulse width. Hence, the op-amp only requires a 0.454V/msec slew rate to meet charging requirements. However, as is the case with the LMC6482, a slew rate three orders of magnitude faster will ensure the ability for a sharp reset characteristic in the ramp signal.

The active integrator produces a linear voltage ramp, as governed by equation 5-4. The charging characteristic of the active integrator relies upon the differential voltage applied to its input terminals. When a negative differential voltage is applied to the input terminals of the op-amp, the output voltage linearly increases in a positive direction for the duration of the pulse width.

$$V_{out} = \int_0^t \frac{-V_{diff}}{RC} + V_{out}(0) \quad (5-4)$$

where:

$$V_{diff} = V_{in} - V_{ref}$$

R is the effective integration resistance

C is the effective integration capacitance

In order for the programmable waveform generator to comply with the criterion for pulse width and magnitude of the ramp waveform, a specific combination of capacitance, resistance, and differential input voltage is required. This design uses a fixed $1\mu\text{F}$ capacitor in the active integrator circuit because preliminary testing demonstrated a very linear charging characteristic for the ramp output voltage. A large variable resistance from $4\text{k}\Omega$ to $814\text{k}\Omega$ was established for the active integrator. This range of resistance also limits the integrator current to reduce power consumption. Using this range of resistance, a differential input voltage of -2.0V is required to meet the AC operating characteristics

of the programmable PEMF generation system. If the reference voltage to this integrator is set at +2.0V, the required differential input voltage is obtained by toggling the input signal from the microcontroller to 0V during the integration period and +2.0V during the reset period. As a result, the output voltage signal of the AC signal generation circuit will ramp from +2.0V to +2.454V when configured for the maximum 2.5mT_{PP} magnetic field.

In this design, resistance is the variable used to modify the charging characteristic of the linear ramp signal. As shown in figure 5-15, to implement a selectable resistance range from 4k Ω to 814k Ω requires two digital potentiometers and one 3-to-8 multiplexer. The active integrator uses both a 100k Ω (MCP41100, Microchip) and 10k Ω (MCP42010, Microchip) potentiometer that can be programmed using the SPI. These two digital potentiometers are implemented in series using the rheostat mode of operation to provide up to 110k Ω of variable resistance with a resolution of 39 Ω . An effective way to increase the programmable resistance of the active integrator was through the development of selectable resistor banks. These resistor banks are selected using a 3-to-8 multiplexer (CD4051BC, Fairchild Semiconductor). Each of the multiplexer outputs is connected to a static resistance ranging in 100k Ω increments from 0 Ω to 700k Ω . The combined contribution from the resistor bank and the digital potentiometers allows the active integrator circuit to achieve a resistance range of 4k Ω to 814k Ω with an effective resolution of 39 Ω . Assuming a 100% duty cycle, if a 454mV_{PP} ramp waveform was being generated with a 1msec pulse width, to maintain a 10Hz frequency resolution requires a resistance resolution of 39 Ω . In the event that the resistor bank and digital potentiometers are set to a very low resistance, a fixed resistor is placed in series with the digital potentiometers to limit the maximum current to 1mA in the active integrator.

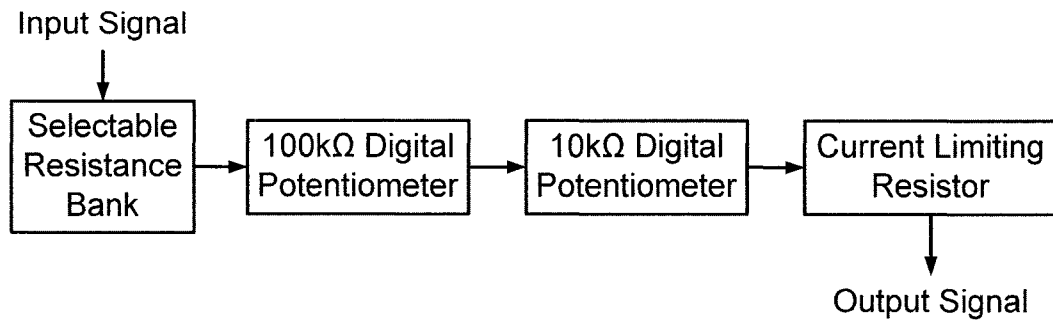


Figure 5-15: Overview of AC signal generation circuit resistance selection

The programmable waveform generator delivers the ramp waveform as a pulse train. To initiate a new ramp pulse the integrator circuit uses an analog bus switch (NC7SZ66, Fairchild Semiconductor) as the reset mechanism, placed in parallel with the integrating capacitor. When the integrator circuit is actively producing a ramp signal the bus switch is turned off. When the integrator circuit is in reset the bus switch is turned on, producing a short circuit across the integrating capacitor, discharging it to the reference voltage. When discharging a capacitor charged to 0.454V, the peak current through the bus switch is approximately 91mA, due to the on-state resistance.

The time required for the integration circuit to reset to within 1% of the reference voltage is 23μsec. During this reset period, the resistance is the 5Ω resistance of the bus switch, rather than the resistance of the resistance bank and digital potentiometers. Since the charging periods for the capacitor range from 1msec to 30msec, the reset times are less than 2.5% of the pulse width. Hence the resulting waveform should have a very sharp reset characteristic.

The last component of the AC signal generation circuit is a push button interrupt to start and stop signal generation. This push button also restarts the PEMF configuration procedure when the system is connected to a computer, so the user can specify their desired settings. By configuring the interrupt on the microcontroller for activation during a rising signal edge, the firmware routine will be executed when the push button is

released. Standard procedure with all push buttons, low pass filtering removes the high frequency harmonics generated on the signal line.

5.5.1.5. DC Signal Generation Circuit

The DC signal generation circuit biases the previously generated AC signal to meet the specifications of the user. It consists of two main sections as shown in figure 5-16. The first section initializes the AC waveform so concepts of a DC bias can be applied. The second section regulates the user-specified DC bias of the overall waveform.

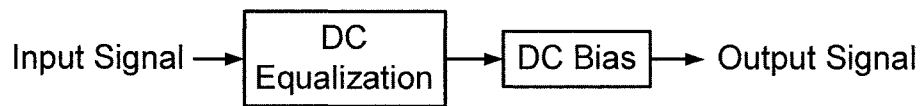


Figure 5-16: Overview of DC signal generation circuit

The DC equalization circuit only affects AC signals that are less than 100% duty cycle. In these situations, there will be an extended reset period in the AC signal when the ramp waveform is not present. When the AC signal is produced by the active integrator, the voltage increases linearly from the +2.0V reference voltage. The DC signal generation circuit shifts the reset value of the ramp waveform to the midpoint of the AC signal. An example of an original AC waveform with a 50% duty cycle is shown in figure 5-17a. When the shift is performed, as shown in figure 5-17b, the ramp waveform will have a constant DC value regardless of the duty cycle imposed to the signal.

The DC equalization module uses a summation circuit to shift the reset component of the waveform to the midpoint of the AC signal. A pulsed DC waveform of half the AC signal magnitude is regulated by the microcontroller's 16-bit timer to pulse high during waveform reset and low during waveform integration. Since the circuit must handle AC signals with a maximum magnitude of 454mV_{PP}, a digital potentiometer (MCP41100, Microchip) controls the output of a voltage divider circuit to range from 0mV to 300mV. A buffer stage is required to separate the resistances of this voltage divider from the resistances of the proceeding summation circuit. In the summation circuit, the pulsed

rectangular waveform and the AC signal are added in equal proportions to create the equalized signal. As to not amplify the equalized signal, the summation circuit is designed as an inverter. Since the input signal ranged from +2.0V to +2.454V, the output signal will range from -2.0V to -2.454V.

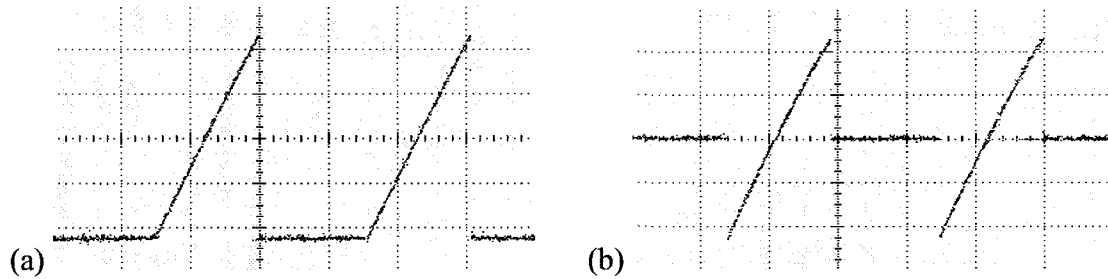


Figure 5-17: Comparison of (a) the original ramp waveform and (b) the DC equalized waveform

It is now feasible to regulate the overall DC bias of the waveform, as specified by the user. The equalized signal is delivered through a high-pass filter with a cut-off frequency ranging from 0.67Hz to 0.74Hz. Although the cut-off frequency is dependent upon the resistance of the digital potentiometer, the AC waveform will pass unattenuated. The resistance component of this filter is also associated with a voltage divider circuit. The user-specified DC bias is created using a voltage divider circuit regulated by a digital potentiometer (MCP42010, Microchip). In previous applications, the voltage divider circuits were restricted to 0V and +3.3V supply rails; however this voltage divider circuit uses $\pm 3.3V$ supply rails. As a result, this circuit produces an output voltage ranging from -0.344V to 0V because the input waveform was previously inverted by the DC equalization circuit, locating it on the negative supply rail. Due to specifications of the MCP42010, the voltage divider must use additional resistors to ensure that terminal voltages on the digital potentiometer remain positive. This bias voltage allows the DC component of the waveform to meet the specifications of the programmable PEMF generation system; a DC magnetic field range of 0mT to 1.25mT.

5.5.1.6. Dual Channel Voltage Output

The last module of the programmable waveform generator produces a dual channel voltage output to be delivered to the coil driver. Immediately following the DC signal generation circuit, the resulting ramp waveform is buffered to prevent the signal from being altered by the proceeding circuit stages. The output from this buffer stage, located in the negative supply rail, is sent to one channel of the coil driver. The other channel signal is created by inverting this buffered ramp waveform. Hence, the other channel of the coil driver is delivered a signal located in the positive supply rail. Inverted signals are used for the two channels of the coil driver to evenly split the current requirement for the coil set between the two supply rails. The current demands of the coil driver will be discussed further in chapter 5-7.

When using the onboard power supplies, preliminary testing indicated that the start-up surge current was too large for the system. Therefore, a manual switch disconnects the signal from one of the output coils. This allows the coils to initialize separately at the start of PEMF generation, limiting the start-up surge current.

5.5.2. Firmware

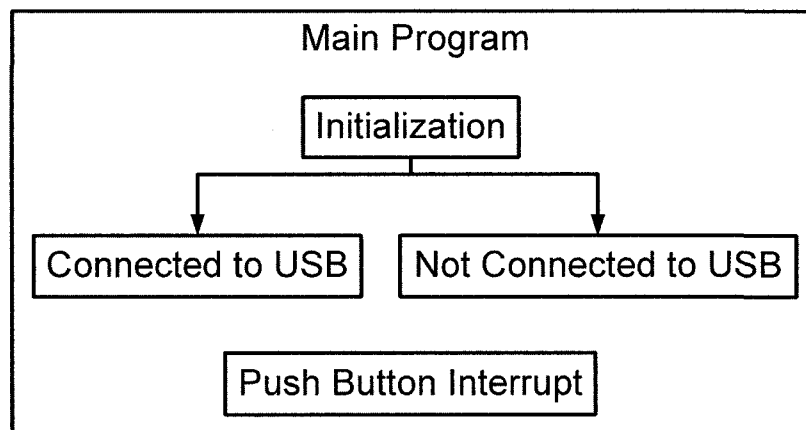


Figure 5-18: Overview of main program firmware

Firmware was written for the microcontroller that provides the required functionality to the programmable waveform generator. This firmware was written in the C programming language. As shown in figure 5-18, the main program starts with an initialization routine from which it branches to a subprogram based upon whether the programmable waveform generator is connected to a USB port. Also, the main program utilizes an interrupt routine, which is hardware activated by a push button.

5.5.2.1. *Main Program Initialization*

The “Main Program Initialization” routine prepares the microcontroller for its control of the programmable waveform generator. This initialization routine disables USART communication since the system may not be connected to a computer, and also disables waveform generation by the system. The push button interrupt is enabled and configured so that the detection of a rising edge will generate a request. Global constants and variables are defined during this initialization routine for their use in any subprogram.

A delay of approximately seven seconds provides sufficient time for the USB circuit to initialize if the programmable PEMF generation system is connected to a computer. Based upon the control signal received by the microcontroller from the USB-UART converter IC, the program will branch to the appropriate subprogram.

5.5.2.2. *Connected to USB Subprogram*

When the microcontroller detects that the system is connected to a computer, it branches to the “Connected to USB” subprogram, outlined in figure 5-19. This subprogram allows the microcontroller to obtain new user settings and calculate the corresponding values for the components of the AC and DC signal generation circuits. This subprogram consists of four modules: EEPROM Access, USART Communication, Calculate Timer Values, and Calculate Resistor Values.

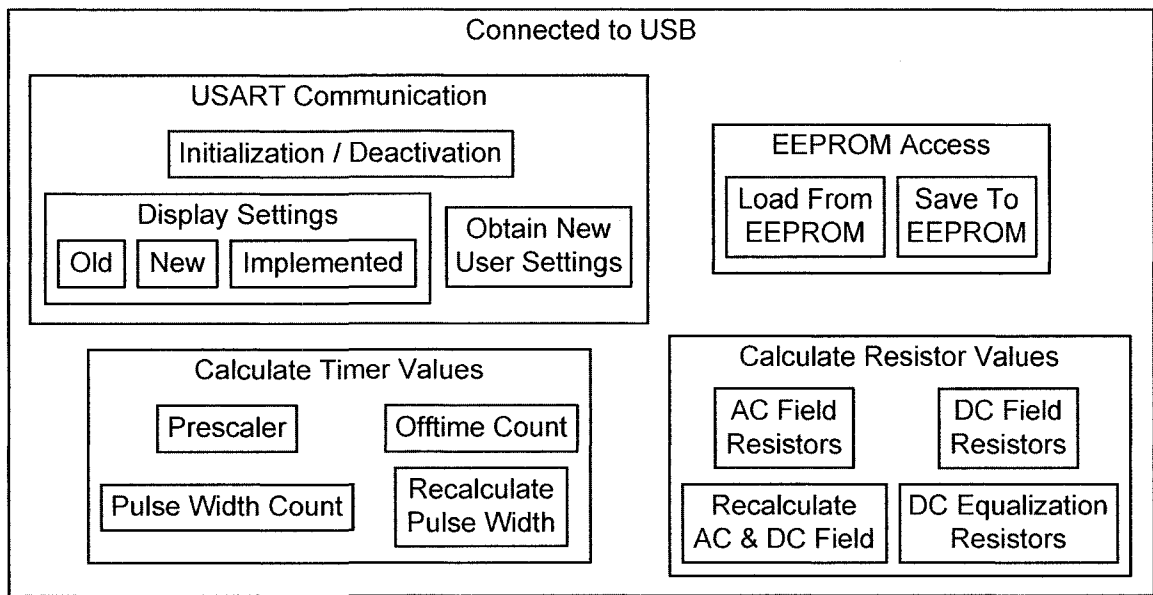


Figure 5-19: Overview of “Connected to USB” subprogram firmware

5.5.2.2.1. EEPROM Access Module

The “EEPROM Access” module loads and saves fifteen settings from the EEPROM. The EEPROM is used rather than FLASH because it retains its memory after the power is cycled. The fifteen settings stored within the EEPROM can be divided into three categories: PEMF User Settings, Resistor Settings and Timer Settings. The specific settings stored within each of these categories are outlined in table 5-1.

Two macros are used to read and write information on the EEPROM. Any information that is transferred should be initialized as a global variable associated with the EEPROM. During EEPROM access it is important that interrupts routines are disabled as to prevent the corruption of data.

PEMF User Settings	Resistor Settings	Timer Settings
<i>B Field AC</i>	<i>Resistor AC Bank</i>	<i>Timer Speed</i>
<i>B Field DC</i>	<i>Resistor DC Bias</i>	<i>Offtime Count</i>
<i>Pulse Width</i>	<i>Resistor AC 10k</i>	<i>Offtime Half Count</i>
<i>Pulse Train</i>	<i>Resistor AC 100k</i>	<i>Pulse Width Count</i>
<i>Duty Cycle</i>	<i>Resistor DC Equalization</i>	<i>Pulse Width Reset Count</i>

Table 5-1: Categorized listing of the settings stored within the EEPROM

5.5.2.2.2. USART Communication Module

Communication using the microcontroller USART allows the user to view the previous PEMF settings and configure new PEMF settings using a computer keyboard and monitor.

The USART must be initialized by the microcontroller before it can be used as a communication module. As was the case with EEPROM access, interrupt routines should be disabled when communicating over the USART, as to not interfere with the transfer of information. This application with the USB-UART converter IC requires asynchronous USART communication. The USART is configured to use an odd parity, a data length of 8 bits, 2 stop bits and a communication baud rate of 115200bits/sec. Once these parameters have been configured, the microcontroller can enable communication across the USART. Communication over the USART should be disabled when it is no longer required. If the system is disconnected from a computer, the USB-UART converter IC is not powered and voltage signals could damage its communication pins.

Upon enabling communication with a computer, the user is greeted and displayed the five PEMF user settings that were saved in the EEPROM from previous usage of the programmable PEMF generation system. The five PEMF user settings are listed in table 5-1.

The user has the option to reconfigure the programmable waveform generator from these current settings. This process prompts the user to enter their desired settings in a predetermined order. These new values are checked to ensure they are within the range of the programmable PEMF generation system. Invalid responses are rejected and the user is prompted to re-enter the value. If at any time the user wants to restart the configuration process, they can do so by entering 'r'. The range of acceptable values for the five PEMF user settings is outlined in table 5-2. The gathering of this information from the user is intuitive except for the *Duty Cycle* and *Pulse Train* settings. The configuration program will ask the user whether they want a 100% duty cycle signal. If the user accepts, they are

not asked for a pulse train setting because the waveform will be continuous. On the other hand, if the user declines, they can choose a duty cycle ranging from 1% to 95%. In situations when the waveform is not continuous, there is the option for a pulse train. The user can select a pulse train ranging from 1 to 25 pulses per train which is present during the active portion of the waveform duty cycle.

User Settings	Range
<i>B Field AC</i>	[0.5 to 2.5] mT _{pp}
<i>B Field DC</i>	[0 to 1.25] mT
<i>Pulse Width</i>	[1 to 35] msec
<i>Duty Cycle</i>	[1 to 95] or 100 %
<i>Pulse Train</i>	[1 to 25] pulses per train

Table 5-2: Valid range for the five PEMF user settings

After the user has configured their new PEMF settings, they are redisplayed to the monitor. If the user declines these settings, they are asked to enter new PEMF settings. If accepted, these settings are used to calculate appropriate values for the timer and resistor modules of the programmable waveform generator. As a result of these calculations, the system may have implemented settings for the AC and DC magnetic fields that are different from the original user request. Therefore these implemented settings are displayed back to the user. If the user accepts the configuration, these settings are saved in EEPROM and the microcontroller deactivates USART communication. The system enters a standby mode of operation allowing the push button interrupt to restart the user configuration procedure. On the other hand, if the user rejects the implemented settings, the program restarts the configuration procedure and asks the user to enter new PEMF settings.

5.5.2.2.3. Calculate Timer Values Module

The microcontroller uses a 16-bit timer configured for a fast pulse width modulation (fast PWM) to regulate the occurrence of events within the programmable waveform generator. The fast PWM is based upon a single-slope operation counting from the *bottom* to *top* value, then restarting the timer cycle at the *bottom* value. The *bottom* value is zero; the *top* value is set as the value in timer register A. As well, this design incorporates timer register B as an intermediate count value between *bottom* and *top*, providing additional functionality to the programmable waveform generator. The integration of two distinct timer modes during waveform generation requires timer registers A and B to be double buffered. These two timer modes use different values for timer registers A and B, which can be set in advance, but will not be updated in the timer configuration until the start of a new count cycle. Timer mode 0 designates the time period when a pulse train is not present, also known as the off-time portion of the waveform duty cycle. Timer mode 1 designates the time period when a pulse train is present, also known as the active portion of the waveform duty cycle.

To initialize the timer module during application of the programmable PEMF generation system, a suitable prescaler value must be established for the timer resolution. Using a 16-bit timer, at a system clock frequency of 3.6MHz, with a unity prescaler corresponds to a maximum time of 17.7msec. However, this time can be exceeded by the operating range of the system when using large pulse width or small duty cycle settings. As a result, using a minimum prescaler value of eight allows the timer to count for 142.2msec, which is larger than the maximum pulse width. However, when using a duty cycle less than 100%, the selection of a timer prescaler is dependant upon the desired pulse width, duty cycle, and pulse train. These three values affect the calculation of *Offtime Count* (equation 5-5), during which no ramping pulse train is present. In order to determine an appropriate timer prescaler, *Offtime Count* is initially calculated using a unity timer prescaler. This resulting timer count is compared to the maximum allowed count for each prescaler value, as outlined in table 5-3. From this comparison, an optimal prescaler value

can be determined for the current PEMF settings which will maximize the timer resolution.

$$Offtime\ Count = \frac{Pulse\ Width \times Pulse\ Train \times \left(\frac{100}{Duty\ Cycle} - 1\right)}{Timer\ Resolution \times 1000} \quad (5-5)$$

Prescaler	Maximum Timer Count	Timer Resolution (μsec)
1	65,536	0.271
8	524,288	2.17
64	4,194,304	17.4
256	16,777,216	69.4
1024	67,108,864	278

Table 5-3: Effect of prescaler on maximum timer count and resolution

Using the optimal prescaler, the firmware calculates a pulse width count and off-time count for the timer registers. *Pulse Width Count* (equation 5-6) only accounts for the time period during which the integrator circuit is actively producing a single ramp signal. Since the timer has varying resolution depending upon the selected prescaler (table 5-3), the implemented pulse width is determined from a back-calculation of equation 5-6. The largest discrepancy occurs when using a 1024 prescaler. To enter this prescaler mode, a pulse width of at least 20.2msec is required. Although a resolution of 0.278msec corresponds to only 1.3% of the pulse width, it is significant when considering 5% reset times for the ramp signal. Also, *Offtime Count* (equation 5-5) corresponding to the total time period of the off-time portion of the waveform duty cycle is recalculated using the implemented pulse width.

$$Pulse\ Width\ Count = \frac{Pulse\ Width}{Timer\ Resolution \times 1000} \quad (5-6)$$

Lastly, *Offtime Half Count* (equation 5-7) and *Pulse Width Reset Count* (equation 5-8) are calculated by the microcontroller to complete the configuration of the timer. *Offtime Half Count* is used in timer mode 0, to provide the opportunity to initialize timer registers A and B for a switch to mode 1. *Pulse Width Reset Count* is used in timer mode 1, and

includes both the active and reset time duration for the development of the ramp waveform by the integrator circuit. Although theoretical calculations determined a 2.5% reset time, the firmware will be configured with a 5% reset time to discharge the integration capacitor.

$$\text{Offtime Half Count} = \frac{\text{Offtime Count}}{2.0} \quad (5-7)$$

$$\text{Pulse Width Reset Count} = \text{Pulse Width Count} \times 1.05 \quad (5-8)$$

The microcontroller firmware has calculated the four count values required for the operation of the timer in the programmable waveform generator. Depending upon the timer mode, these count values are configured into timer registers A and B according to table 5-4.

Timer Register	Timer Mode	
	Mode 0	Mode 1
A	<i>Offtime Count</i>	<i>Pulse Width Reset Count</i>
B	<i>Offtime Half Count</i>	<i>Pulse Width Count</i>

Table 5-4: Configuration of the timer registers for mode 0 and mode 1

5.5.2.2.4. Calculate Resister Values Module

The microcontroller is responsible for the calculation of all the resistor values configured in the programmable waveform generator. These resistor calculations are divided into three main categories: AC field resistors, DC field resistors and DC equalization resistors. These resistors will regulate the magnitude of the AC and DC magnetic field components as specified by the user.

The resolution of the 8-bit digital potentiometers can be determined according to equation 5-9. The accuracy of this calculation is improved by taking into account the residual wiper resistance of the potentiometer.

$$\text{Resistor Resolution} = \frac{\text{Resistance}_{\max} - \text{Resistance}_{\text{wiper}}}{255} \quad (5-9)$$

Settings are calculated for the resistor bank and digital potentiometers in the AC signal generation circuit. A maximum ramp voltage (V_{\max}) for the integrator circuit is calculated using equation 5-3, corresponding to the user-specified AC magnetic field. The integrator circuit can be tuned to achieve V_{\max} by varying its effective total resistance. Rearrangement of the characteristic equation for an active integrator circuit (equation 5-4), yields a relation for the required resistance (equation 5-10) to achieve the user-specified pulse width and maximum ramp magnitude. This equation also incorporates fixed aspects of the active integrator circuit such as the capacitance and differential input voltage (V_{int}). Obtaining these implemented values is discussed in chapter 5-8. Although valid user settings should already limit the range of $\text{Resistance}_{\text{Total}}$, the software will limit this value between 3.56k Ω and 782.594k Ω , according to the capability of the implemented circuit.

$$\text{Resistance}_{\text{Total}} = \frac{V_{\text{int}} \times \text{Pulse Width}}{V_{\max} \times \text{Capacitance} \times 1000} \quad (5-10)$$

To achieve this value of $Resistance_{Total}$ requires the selection of an appropriate resistor bank ($Resistor_{AC\ Bank}$) in the integrator circuit. The resistor bank algorithm selects the largest resistor bank such that $Resistance_{Total}$ is less than the combined resistance from the resistor bank, maximum output of the digital potentiometers and residual resistance in the integrator circuit. The residual resistance ($Resistance_{Residual}$) in the integrator circuit is accounted for by the current limiting resistor and the wiper resistance of the digital resistors.

Using the selected resistor bank, the total resistance required from the 10kΩ and 100kΩ digital resistors in the integrator circuit can be calculated with equation 5-11.

$$Resistance_{Digital} = Resistance_{Total} - Resistor_{AC\ Bank} - Resistance_{Residual} \quad (5-11)$$

As mentioned, there are two digital potentiometers to be programmed by the microcontroller. The setting for the 100kΩ potentiometer is calculated first, followed by the calculation of the 10kΩ potentiometer setting. The 100kΩ potentiometer provides the greatest variability in resistance, and will be set as the value nearest to the required digital resistance according to equation 5-12. When the resistor bank was implemented, some of the spacings were slightly more or less than 100kΩ, due to the accuracy of the surface mount resistors. In the case that the 100kΩ digital potentiometer is not large enough to satisfy the required resistance, it will be set to its maximum data setting of 255. The additional resistance required will be obtained from the 10kΩ digital resistor.

$$Resistor_{AC\ 100k} = \frac{Resistance_{Digital}}{Resistor\ Resolution_{AC\ 100k}} \quad (5-12)$$

To improve the accuracy of the implemented digital resistance requires the use of a 10kΩ digital potentiometer. An appropriate setting for the 10kΩ potentiometer will be calculated according to equation 5-13.

$$Resistor_{AC\ 10k} = \frac{Resistance_{Digital} - (Resistor_{AC\ 100k} \times Resistor\ Resolution_{AC\ 100k})}{Resistor\ Resolution_{AC\ 10k}} \quad (5-13)$$

All of the settings for the resistors within the integrator circuit have been calculated. These settings will be programmed to the resistive elements prior to waveform generation, to ensure the functionality of the AC signal generation circuit.

Since the digital hardware used for AC signal generation has limited resolution, in regards to resistance, it may not be able to exactly meet the specifications desired by the user. Using the implemented value of resistance in the integrator circuit, the firmware will calculate the implemented ramp waveform magnitude by a rearrangement of equation 5-10. Thus, the microcontroller can calculate the implemented AC magnetic field, via equation 5-3, corresponding to this implemented ramp waveform.

The DC signal generation is divided into two voltage divider networks, each containing a digital potentiometer. The following calculations require the implemented values of the +3.3V supply rail (V_{CC}) and the -3.3V supply rail (V_{EE}) for optimal accuracy. The microcontroller calculates the DC equalization resistance setting for the 100k Ω digital potentiometer (equation 5-14) required to produce an equalization voltage ($V_{DC_Equalization}$) half the magnitude of the AC ramp voltage.

$$Resistor_{DC\ Equalization} = \frac{\frac{(996500 \times (V_{DC\ Equalization}))}{V_{CC} - V_{DC\ Equalization}} - Resistance_{DC\ Equalization\ wiper}}{Resistor\ Resolution_{DC\ Equalization}} \quad (5-14)$$

The microcontroller also calculates the required resistance for the generation of the DC magnetic field. As was the case with the AC signal, the desired DC magnetic field is associated with a DC voltage (V_{DC}) to be achieved by the programmable waveform generator. However in this situation the applied DC voltage is negative because the AC signal, that was originally positive, has been inverted by the DC equalization circuit. This voltage corresponds to a setting for a 10k Ω digital potentiometer (equation 5-15) that regulates a voltage divider circuit.

$$R_{DC\ Bias} = \frac{(43000 \times (V_{CC} - V_{DC})) - (43000 \times (V_{EE} + V_{DC})) - R_{DC\ Bias} \tan \theta}{V_{DC} + V_{EE}} \quad (5-15)$$

Although the implemented DC magnetic field should be very close to the user-specified value, it could vary due to the digital components of the programmable waveform generator. As a result, the implemented DC voltage from the digital voltage divider is back-calculated from equation 5-15, followed by the calculation of the implemented DC magnetic field.

5.5.2.3. *Disconnected from USB Subprogram*

If the programmable PEMF generation system is not connected to a computer, the firmware branches to the “Disconnected from USB” subprogram. Outlined in figure 5-20, this subprogram consists of two modules, system initialization and waveform generation, that allow the programmable PEMF generation system to produce the user-specified ramp magnetic field.

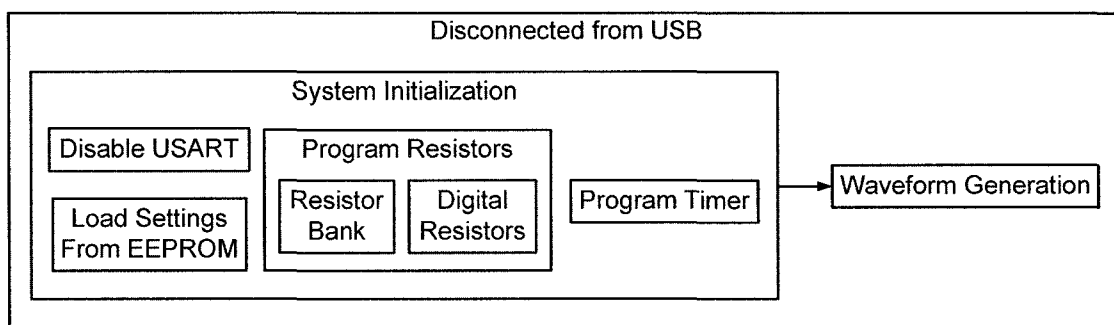


Figure 5-20: Overview of “Disconnected from USB” subprogram firmware

5.5.2.3.1. **System Initialization Module**

The “System Initialization” module prepares the programmable waveform generator for the output of the user-specified ramp waveform. Since the system is not connected to a computer, the firmware disables USART communication, preventing undesired signals on the communication lines that could damage the unpowered and therefore unprotected USB-UART conversion circuit. As well, the timer and resistor settings, as outlined in table 5-1, are loaded from EEPROM to be programmed into their respective digital components by the microcontroller.

The microcontroller will program the onboard 16-bit timer with the appropriate settings for waveform generation. The timer is configured to operate in the fast PWM mode with the *top* count specified by the content of timer register A. The timer will start when prompted by the push button interrupt on the programmable waveform generator. Rather than using timer interrupts, custom firmware has been developed to guide waveform generation based upon the status of the timer flags A and B. These flags, cleared during

initialization, indicate when the timer has reached the count specified by their respective registers. Lastly, as specified by table 5-4, the timer registers A and B are initialized with their value required for mode 1 of the timer operation.

The microcontroller also programs the resistive elements of the programmable waveform generator. The resistive elements to be programmed are the resistor bank and four digital potentiometers. The resistor bank, located in the AC signal generation circuit, is programmed through the control of a 3-to-8 multiplexer using three I/O pins on the microcontroller. The digital potentiometers are programmed by the microcontroller using the SPI. In this design, the programming of the four required potentiometers is executed using two distinct modules. The first module programs the 100k Ω potentiometer for the DC bias circuit. The second module programs the three remaining potentiometers for the AC signal generation circuit and the DC equalization circuit. This second module programs three resistors because they are daisy chained together in the hardware, due to the serial out on the MCP42010.

Communication across the SPI is from the master device (microcontroller) to the slave device (digital potentiometer). Although the digital potentiometers can perform at a maximum SPI clock frequency of 10MHz, the clock rate will be configured at 230kHz to improve the reliability of communication. Successful communication with the digital potentiometers requires a clock polarity such that a leading edge is a falling signal and a trailing edge is a rising signal. As well, the clock phase is established so the data is sampled on the trailing edge of the clock signal. Once the SPI communication pins and control registers are initialized, the chip select for the desired potentiometers can be activated to begin programming. The digital potentiometers require both a command and data byte to successfully configure their settings.

The programming of the 100k Ω potentiometer in the DC bias circuit starts by activating the corresponding chip select. Once activated, a command byte is sent to the digital potentiometer informing that data will be written to potentiometer 0. In single potentiometer ICs (MCP41100, Microchip), there is only potentiometer 0; however, in

dual potentiometer ICs (MCP42010, Microchip), there is potentiometer 0 and potentiometer 1. Following this command byte is the data byte containing the setting $Resistor_{DC\ Bias}$. Upon receipt of this data, the chip select is deactivated to complete the programming of this potentiometer for the DC bias circuit.

To program the daisy chain network, information is first delivered for the 100k Ω potentiometer since it is at the end of the serial communication line. Immediately following, the information for the dual 10k Ω potentiometer is delivered from the microcontroller. All of the potentiometers in this daisy chain network use the same chip select signal from the microcontroller. During programming of the 100k Ω potentiometer in the integrator circuit, its command byte informs that data will be written to potentiometer 0; its data byte contains the value $Resistor_{AC\ 100k}$. Although this information is initially delivered to the MCP42010, it will be transferred to the MCP41100 when the MCP42010, receives the next command and data byte from the microcontroller. The microcontroller now programs one of the resistors in the MCP42010. In this design, the command byte indicates that data will be written to potentiometer 0, corresponding to the 10k Ω potentiometer in the integrator circuit. As a result, its corresponding data byte contains the value $Resistor_{AC\ 10k}$. The chip select corresponding to these two potentiometers is deactivated to complete this programming. It is not possible to program both resistors of the MCP42010 in a single programming cycle.

This chip select is reactivated so the microcontroller can program the remaining 10k Ω potentiometer in the MCP42010. The microcontroller sends a single command and data byte over the SPI that writes the value of $Resistor_{DC\ Equalization}$ into potentiometer 1 of the MCP42010. Deactivation of the chip select completes the programming of this resistor in the DC equalization module; thereby not affecting the programming of the proceeding 100k Ω potentiometer.

The “System Initialization” routine has completed programming for the microcontroller timer and resistive elements of the programmable waveform generator. Prior to the enabling of interrupts, their flags are cleared to remove any impending interrupt request.

Once the interrupts are enabled, the push button interrupt can start and stop waveform generation.

5.5.2.3.2. Waveform Generation Module

The “Waveform Generation” module uses the onboard 16-bit timer to produce an output waveform with the desired user specifications. This module is executed by the microcontroller once the timer and resistor elements have been initialized in the programmable waveform generator. As shown in figure 5-21, the functionality of the “Waveform Generation” module depends upon whether *Waveform Status* has been activated by the push button interrupt.

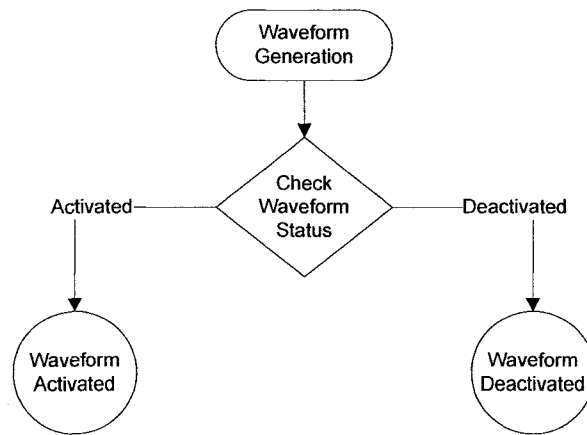


Figure 5-21: Overview of the “Waveform Generation” subroutine

Waveform Status is deactivated upon first entering the “Waveform Generation” subroutine, allowing the system to be initialized as shown in figure 5-22. The system is prepared for waveform generation, but not yet activated. In this initialized state the timer is stopped and the system remains in this state until the push button is pressed. This activates *Waveform Status* allowing the programmable waveform generator to output the desired user-specified ramp waveform.

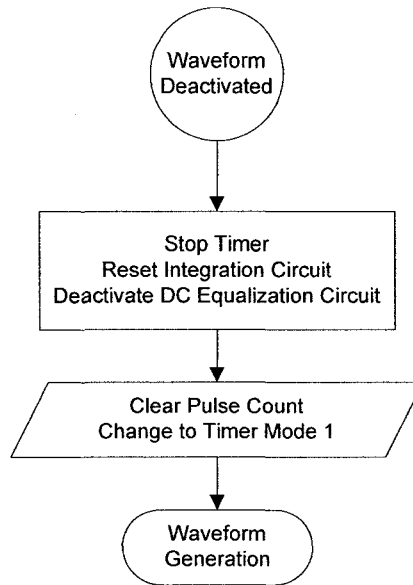


Figure 5-22: Overview of the “Waveform Deactivated” subroutine

When *Waveform Status* is activated, the firmware branches to the “Waveform Activated” subroutine. This subroutine starts the operation of the timer, according to the predetermined timer prescaler stored in *Timer Speed*. Timer flags A and B are set as the timer runs through its count. Based on the flag set and the operational mode of the timer, the firmware will control the integration and DC equalization circuits, as indicated by figure 5-23, in order to create the user-specified ramp waveform. Timer flags are cleared upon return to the start of the “Waveform Generation” subroutine. The firmware also increments the variable *Pulse Count*, each time a single ramp pulse is generated for the pulse train.

The variable *Pulse Count* is monitored by the “Pulse Train Regulation” subroutine (figure 5-24). If *Pulse Count* is less than the user-specified pulse train length, the firmware proceeds to develop another ramp pulse. Once *Pulse Count* equals the desired pulse train length, the firmware checks the user-specified duty cycle. Based upon this duty cycle, the timer may change its mode of operation to produce the off-time portion of the waveform. As a result, the microcontroller can regulate all timing aspects of the desired ramp waveform.

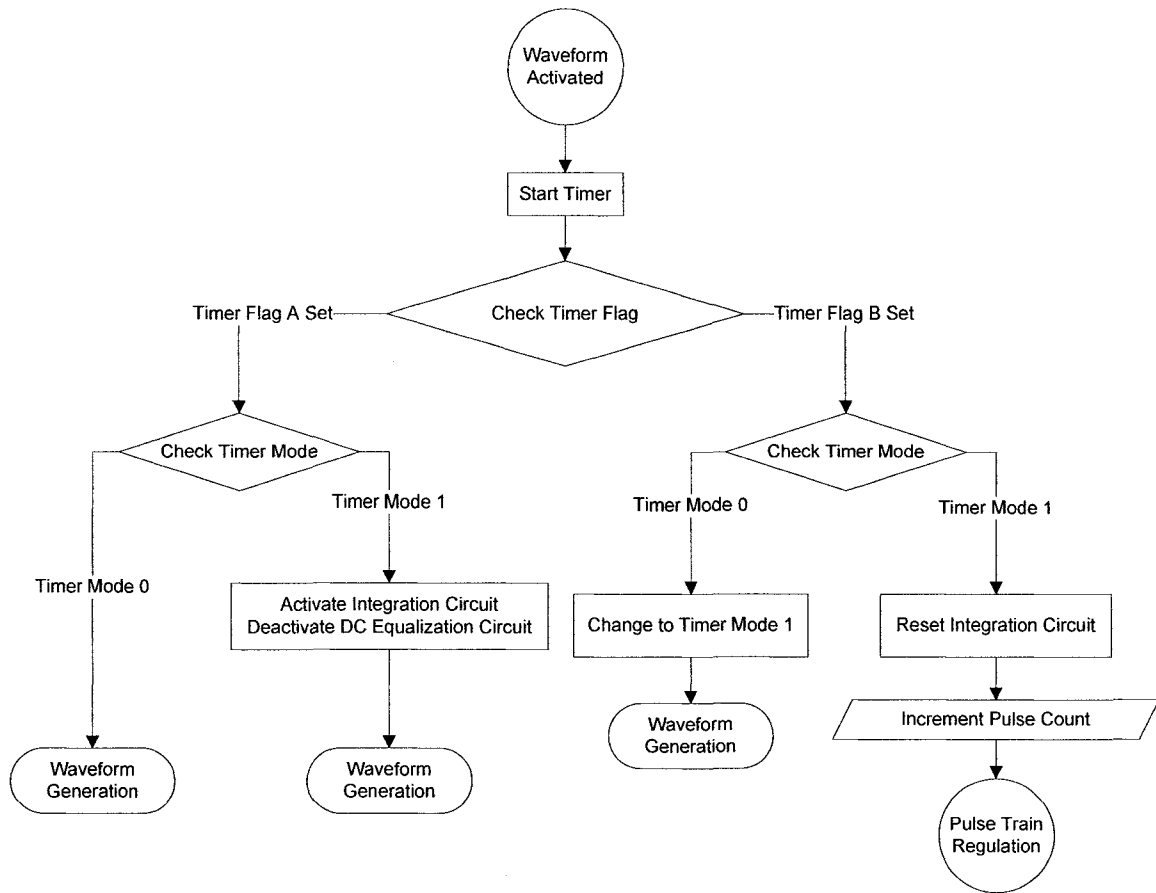


Figure 5-23: Overview of the “Waveform Activated” subroutine

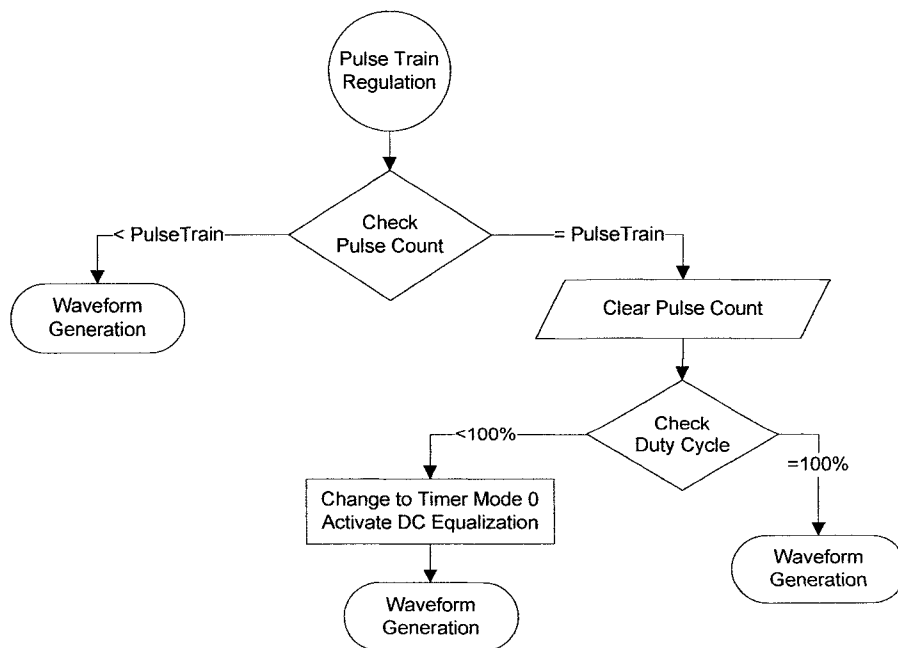


Figure 5-24: Overview of the “Pulse Train Regulation” subroutine

5.5.2.4. Interrupt Service Routine

An interrupt service routine has been developed, which is requested whenever the push button is pressed. If the system is connected to a computer, the interrupt routine allows the user to restart the PEMF configuration procedure, by toggling the updated settings status in firmware. If the system is not connected to a computer, the interrupt routine starts and stops waveform generation for the programmable PEMF generation system, by toggling *Waveform Status* in firmware.

5.6. *Magnetic Field Sensor*

A magnetic field sensor system was developed for the programmable PEMF generation system so the user can verify the produced magnetic field. A schematic of this circuit can be found in appendix C. This system consists of a magnetic field sensor and an instrumentation amplifier. The magnetic field sensor was an external component with a cabling interface to the instrumentation amplifier. The instrumentation amplifier was placed on the printed circuit board containing the programmable waveform generator.

The magnetic field sensor chosen for this system is the Allegro A1395 because it is one of the few sensors that can operate from a supply voltage of +3.3V. This sensor has a specified sensitivity of 100mV/mT while operating at a nominal supply voltage of +3V. Since the implemented supply voltage is an increase of 10% from the nominal value, the sensitivity of the sensor should also increase by 10%. Therefore the actual sensitivity is predicted to be 110mV/mT.

The magnetic field sensor is attached to a 2m long cable. The use of an external cable allows freedom to the positioning of the sensor in specific environments. This cable connects the sensor to the instrumentation amplifier circuit within the casing of the programmable waveform generator. This cable delivers 0 and +3.3V supply rails and a sleep command to the sensor, and receives the output signal from the sensor. The A1395 magnetic field sensor also has the ability to enter shutdown mode for reduced current consumption. This functionality is implemented through a manual switch, onboard the programmable waveform generator, that sends a sleep command to the sensor.

To maximize swing on the output signal, the reference voltage is tied to the supply voltage since the quiescent output voltage of the sensor is half the reference voltage. During experimental conditions, the maximum magnetic field will be $2.5\text{mT}_{\text{peak}}$, corresponding to a voltage swing of $0.275V_{\text{peak}}$ on the sensor output. This output signal can be amplified to improve the SNR. Signal amplification is performed using an instrumentation amplifier (MAX4194, Maxim). This instrumentation amplifier is

provided a reference output voltage of +1.65V to maximize the voltage swing capability. This reference voltage also corresponds to the quiescent output voltage of the magnetic field sensor. Hence, the inverting input on the amplifier is also set at this reference voltage, to maximize the common mode signal. The instrumentation amplifier will be designed with a gain of 4.33, corresponding to an output swing of $1.2V_{\text{peak}}$ during maximum loading conditions.

This amplified output signal can be monitored through an external connection with an oscilloscope. The measured peak-to-peak voltage signal can be converted to a magnetic field strength according to equation 5-16.

$$B_{\text{measured}} [mT_{PP}] = \frac{V_{\text{measured}} [mV_{PP}]}{\text{Gain} \times \text{Sensitivity}} \quad (5-16)$$

$$B_{\text{measured}} [mT_{PP}] = \frac{V_{\text{measured}} [mV_{PP}]}{476 [mV / mT]}$$

When the magnetic field sensor was implemented, the resulting magnetic field strength after amplification of the sensor signal was reduced on average by 2% as compared to the raw signal. This discrepancy can be accounted for by the noise present on the sensor signal and the 1% tolerance rating of the surface mount resistor used to establish amplifier gain.

5.7. Current Consumption Analysis

The current consumption by the programmable PEMF generation system is separated into two divisions: the programmable waveform generator and the coil driver.

5.7.1. Programmable Waveform Generator

The current analysis for the programmable waveform generator module is divided into the digital and analog circuits for waveform generation, as well as the onboard magnetic field sensor.

The programmable waveform generator uses both digital ICs, and analog circuits to produce the user-specified signal. In regards to the digital component of waveform generation, there are thirteen ICs that, when fully activated, demand a total current supply of $32.2\text{mA}_{\text{RMS}}$. Of this total, 15mA_{RMS} of current is required by the USB-UART converter IC. The microcontroller requires a supply current of $3.5\text{mA}_{\text{RMS}}$ to control the functionality of the system. The analog circuits associated with waveform generation only require a supply current of $6.2\text{mA}_{\text{RMS}}$.

The onboard magnetic field sensor consumes approximately $3.4\text{mA}_{\text{RMS}}$ of current when activated. This system can also be toggled into a sleep mode, when not in use, thereby reducing current consumption to $0.2\text{mA}_{\text{RMS}}$.

When connected to a computer, the programmable waveform generator requires a total supply current of $41.8\text{mA}_{\text{RMS}}$. In the situation that the system is connected to a 4-port hub, the available current of $125\text{mA}_{\text{RMS}}$ is able to meet the requirements of the programmable waveform generator.

If the system is not connected to a computer, the current consumption by the programmable waveform generator is reduced to $26.8\text{mA}_{\text{RMS}}$. This is because the USB-UART converter IC is not activated. As an alternative to an external power supply, the programmable waveform generator could be powered by a battery. Using a lithium ion

rechargeable battery with a voltage range from +3V to +4.2V and a capacity of 6.1Ahr, the programmable waveform generator could operate for over 200 hours on a single charge cycle.

5.7.2. Coil Driver

The majority of the current required for the programmable PEMF generation system is consumed by the coil driver. This analysis is divided into two sections: the current required for coil driver itself and the connected coil set.

In regards to the coil driver itself, a total of 209.5mA_{RMS} of current is consumed. Of this consumption, 46mA_{RMS} is consumed by the three ICs, 160mA_{RMS} is consumed by the cooling fan, and the remaining 3.5mA_{RMS} is consumed by analog circuits.

The majority of the current supplied to the coil driver is consumed by the coil set for generation of the magnetic field. The maximum current will be delivered to the coil set when the programmable PEMF generation system is configured for the maximum AC magnetic field of 2.5mT_{PP} and the maximum DC magnetic field of 1.25mT. During this configuration, each coil will require a current of 1.35A_{peak} or 0.78A_{RMS}.

Taking this all into account, the coil driver requires a supply current of 1.773A_{RMS}. Unlike the programmable waveform generator, it is not practical to power the coil driver module with a battery pack. Using a lithium ion rechargeable battery pack with a capacity of 6.1Ahr, the coil driver could only function for only 3 hours on a single charge cycle.

5.8. System Verification

The purpose of system verification is to test the functionality of the subsystems required in the programmable PEMF generation system. The two main subsystems are the coil driver and the programmable waveform generator. During system verification these subsystems are calibrated according to the implemented circuit conditions.

5.8.1. Coil Driver

There were a few issues during the coil driver verification such as the gain of the coil driver and the resulting magnetic field strength.

Measurement of the input ramp voltage applied to the coil driver and the output magnetic field detected from a magnetic field sensor, yielded the implemented relationship of equation 5-3. Comparison to the theoretical analysis (equation 5-2) yielded an error of 86% between values. Some of the discrepancy between theoretical and experimental magnetic fields was accounted for by the implemented gain of coil driver. If the coil driver performed according to the design specifications, it should amplify the input voltage by a factor of 10. However, measurement of the input and output voltage from the coil driver revealed an approximate 15 times gain; an increase of 50% from the designed value. It is apparent that there are unaccounted for resistance, capacitance and inductance characteristics in the coil driver; however, the implemented resistance for the amplifier gain was equal to design specifications. As a result, the implemented relation for the voltage to current conversion of the coil driver is stated in equation 5-17.

$$I = 2.4 \times V_{in} \quad (5-17)$$

Using this new relation for theoretical calculations reduces the error between the implemented and theoretical magnetic field-to-voltage conversion factor to 24%. The remaining error could be attributed to the calibration of the magnetic field sensor, assumptions made in magnetic field modelling, alignment of the coil set, and placement of the magnetic field sensor.

5.8.2. Programmable Waveform Generator

The programmable waveform generator has several modules such as the computer interface and 16-bit timer that must work properly before the entire programmable PEMF generation system can be verified according to its specifications. As well, the calibration procedure updated the firmware with the implemented circuit conditions involved in the generation of the user-specified waveform.

5.8.2.1. *Verification of Computer Interface*

The computer interface allows the user to program their desired PEMF settings into the system. The functionality of the computer interface can be verified through the testing of (1) the PEMF configuration menu and (2) the user input.

1) The PEMF Configuration Menu

After the programmable waveform generator system was connected to a PC, a menu was displayed in the following order:

- a. Display welcome screen
- b. Display current PEMF settings
- c. Prompt for new AC magnetic field
- d. Prompt for new DC magnetic field
- e. Prompt for new ramp pulse width
- f. Prompt for new waveform duty cycle
- g. Prompt for new pulse train count
- h. Display user-specified settings
- i. Display implemented settings

Additional information on how the firmware advances through the PEMF configuration menu is provided in chapter 5-5. Referring to this design, the implemented system functioned according to specifications.

2) The User Input

The user input was verified so PEMF settings are properly limited to the operating range of the system, the user can restart the configuration process and the user can accept or decline PEMF settings. User-specified PEMF settings were only accepted by the system if they were within the limits of table 5-2. The user could restart the configuration process either with the push button interrupt or a keyboard command. As well, the user could accept or decline the PEMF configuration when the firmware displayed the settings retrieved from the EEPROM, the new settings as specified by the user, and the implemented settings for the programmable PEMF generation system.

5.8.2.2. Verification of 16-bit Timer

Verification of the 16-bit timer involved three objectives. The first objective was to determine whether the timer can operate in the 100% duty cycle mode. The second objective was to determine whether the timer can switch to a higher prescaler mode when required by register limitations. Lastly, the third objective was to determine whether timer operation can be started and stopped by the push button interrupt.

The system was verified for its operation in the 100% duty cycle mode using the minimum and maximum pulse widths. The minimum pulse width of 1msec allowed the least amount of time for events to occur in both the firmware and hardware. The maximum pulse width of 35msec ensured that the timer can operate in the 100% duty cycle mode without violating register count restrictions. When using the minimum pulse width, there was less than 0.4% error in the ramp time. Since the allocated reset time was 50 μ sec when using the minimum pulse width and the timer resolution was 2 μ sec, the error increased to 12%. However, because reset times are designated as 5% of the ramp time, the effect of this error on the overall waveform was negligible.

The system was also validated for its operation in each timer prescaler mode. Sample settings for pulse width, pulse train, and duty cycle that allow the system to enter each timer prescaler mode are provided in table 5-5. Measurements indicated that the timing

accuracy degrades when using a larger prescaler mode, due to a decreased timer resolution. Although the error in reset times was a maximum of 5%, all other timing errors were less than 1%; indicating good performance of the system.

Prescaler	Pulse Width (msec)	Pulse Train (pulses / train)	Duty Cycle (%)
8	35	25	90
64	35	25	75
256	35	25	15
1024	35	25	10

Table 5-5: Programmable waveform generator temporal settings for the four timer prescaler modes

Lastly, the use of the push button interrupt confirmed that it could start and stop the operation of the 16-bit timer and therefore waveform generation.

5.8.2.3. Implemented Circuit Conditions

The objective of this procedure was to calibrate the firmware according to the implemented circuit conditions. These updated circuit conditions will affect the outcome of firmware calculations.

Calibration was first performed on the resistor calculations for the AC signal generation circuit. The calibration procedure measured the implemented capacitance, static resistance and input voltage of the integration circuit. The resistor bank algorithm was also updated with implemented values. Although the implemented resistance varied from the designed values, the maximum spacing was less than 100k Ω as required for the digital potentiometers. Lastly, the maximum obtainable resistance of the digital potentiometers was measured and updated in firmware, since their specifications allow a range of 20%.

Calibration was also performed on the resistor calculations for the DC signal generation circuit. The calibration procedure measured the implemented $\pm 3.3V$ supply rails and static resistances present in the voltage divider circuits. As well, the maximum obtainable resistance of these digital potentiometers was measured and updated in the firmware.

Chapter 6

6. System Testing and Results

This chapter discusses the testing of the programmable PEMF generation system. The system was verified according to its design specifications for the AC and DC magnetic field strengths, pulse width, duty cycle and pulse train. As well, a calibration procedure was performed on the AC waveform component to align theoretical and experimental results.

6.1. Objectives

The testing procedure was to satisfy two main objectives:

- 1) Calibration of the system to align theoretical and experimental waveforms
- 2) Verification of the programmable PEMF generation system operating range

6.2. Methodology

The methodology used to calibrate and verify the operational range of the programmable PEMF generation system was separated into the testing of the AC and DC signal. Using this approach, each procedure progressed through three stages:

- 1) Approval of implemented settings specified by microcontroller
- 2) Approval of voltage waveform produced by programmable waveform generator
- 3) Approval of magnetic waveform produced by coil set

6.2.1. Calibration of AC Waveform

The testing procedure began with the calibration of the AC signal. The experimental measurements were compared with the implemented settings based on theoretical calculations. Before the calibration, the firmware was programmed with a magnetic field-to-voltage conversion factor based upon the coil driver relation of equation 5-17, and the original magnetic field model of equation 4-3. Large pulse widths of 15msec and 35msec were used to prevent the inductance of the coil set from altering the resulting magnetic field. The magnitude of the AC magnetic field was set at $0.5mT_{PP}$, $1.5mT_{PP}$ and $2.5mT_{PP}$, allowing calibration over a range of operating conditions. Lastly, the DC bias was set to

zero and the system was specified for a 100% duty cycle waveform. Both the programmable waveform generator output voltage and the resulting magnetic field strength were measured and compared with theoretical values. The same results (table 6-1) were achieved for both the 35msec and 15msec pulse width settings and were used to align the theoretical and experimental waveforms.

Implemented Settings based on Theoretical Calculations		Experimental Measurements		Error	
AC Magnetic Field (mT _{PP})	Calculated Voltage Signal (mV _{PP})	AC Magnetic Field (mT _{PP})	Voltage Signal (mV _{PP})	AC Magnetic Field	Voltage Signal
0.5	113	0.7	135	45.5%	19.5%
1.5	340	2.0	397.5	36.4%	16.9%
2.5	566	3.3	645	32.7%	14.0%

Table 6-1: Experimental results before calibration using pulse widths of 35msec and 15msec

The average error in the voltage waveform generation was 16.8% in the performed trials. As a result, the calculation for the voltage waveform generation was adjusted by a factor of 16.5% in the microcontroller firmware. Although this adjustment was slightly less than the average error, it provided a bias towards the generation of larger magnetic fields.

From the results of table 6-1, the experimentally measured magnetic field yields an average error of 38.2% from the desired implemented settings. However, if there was no error in the voltage signal produced by the programmable waveform generator, the error for the magnetic field is reduced to 21.7%. Assuming a linear relationship, the magnetic field-to-voltage conversion factor can be adjusted to reduce this observed error. Previous experimental trials using the coil driver, such as for the experiments of chapter 3, indicate that a linear relationship should not be implemented. The 19.3% decrease made to the implemented conversion factor, as represented in equation 5-3, was actually less than that suggested by the observed error. As will be shown in post calibration results, the use of a linearly based adjustment would not have optimized the accuracy of the system.

Calibration of the voltage and magnetic field waveforms improved the accuracy of the programmable PEMF generation system. The experimental trials, using pulse widths of 35msec and 15msec, were repeated for the calibrated system and the results are shown in tables 6-2 and 6-3 respectively. Illustrated in figure 6-1 are experimental waveforms as obtained from an oscilloscope. The SNR on the 0.5mT_{PP} signal was significantly less than the 2.5mT_{PP} signal. In regards to the 91mV_{PP} and 454mV_{PP} voltage signal from the programmable waveform generator, the noise level was ±5mV. In regards to the 0.5mT_{PP} to 2.5mT_{PP} magnetic field signal, the noise level was ±0.05mT. The error in obtaining a peak-to-peak measurement from an oscilloscope was twice the signal noise level. This accounted for the inconsistent error at a 0.5mT_{PP} magnetic field setting for pulse widths of 15msec and 35msec.

Implemented Settings Based on Calibrated Calculations		Experimental Measurements		Error	
AC Magnetic Field (mT _{PP})	Calculated Voltage Signal (mV _{PP})	AC Magnetic Field (mT _{PP})	Voltage Signal (mV _{PP})	AC Magnetic Field	Voltage Signal
0.52	94	0.5	95	-3.8%	1.1%
1.5	272	1.4	275	-6.1%	1.1%
2.5	454	2.3	450	-6.9%	-0.9%

Table 6-2: Experimental results after calibration using a pulse width of 35msec

Implemented Settings Based on Calibrated Calculations		Experimental Measurements		Error	
AC Magnetic Field (mT _{PP})	Calculated Voltage Signal (mV _{PP})	AC Magnetic Field (mT _{PP})	Voltage Signal (mV _{PP})	AC Magnetic Field	Voltage Signal
0.5	91	0.5	95	0.0%	4.4%
1.5	272	1.4	275	-5.5%	1.1%
2.5	454	2.3	459	-6.9%	1.1%

Table 6-3: Experimental results after calibration using a pulse width of 15msec

After the system was calibrated, the accuracy of both the voltage signal and resulting magnetic field was improved. The actual voltage generation was within 1% of the desired ramp magnitude. The average error between the experimentally generated magnetic field and desired implemented values was approximately 5%. Prior to calibration, the magnetic field was being overestimated; after calibration, the magnetic field was being underestimated. Therefore, if a linearly based adjustment had been implemented on the

magnetic field-to-voltage conversion factor, the accuracy of the system would have been reduced.

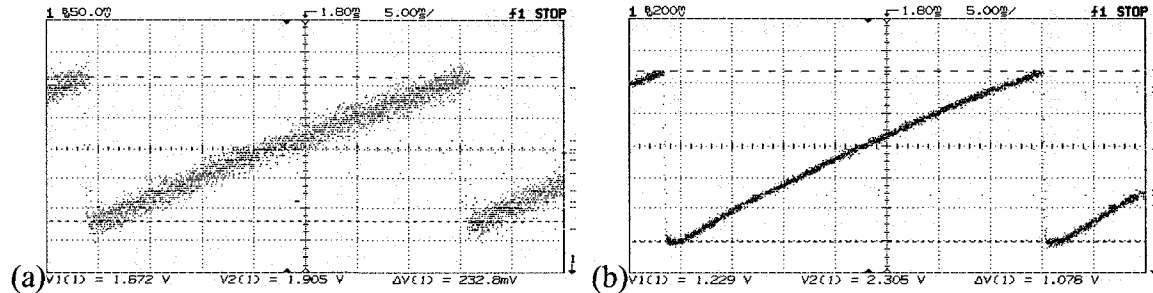


Figure 6-1: Magnetic waveform measurements for a 100% duty cycle, 35msec pulse width signal configured for an AC magnetic field strength of (a) 0.5mT_{PP} and (b) 2.5mT_{PP}

The error between measured and desired signal magnitudes was equal or less than the error involved in obtaining a measurement from the oscilloscope; therefore, the system was calibrated. As a result, the verification of the AC and DC field operating range for the programmable PEMF generation system could be performed.

6.2.2. Verification of AC Field Operating Range

The verification of the AC field operating range for the programmable PEMF generation system was separated into two sections:

- 1) Verification of an individual ramp pulse
- 2) Verification of waveform duty cycle and pulse train

Verification of an individual ramp pulse, investigated the effect of coil inductance on the accuracy of the programmable PEMF generation system. As a result, the pulse width settings were biased towards smaller values. During the calibration procedure, the system was verified at the maximum operational pulse width of 35msec and an intermediate pulse width of 15msec. The AC field verification procedure used pulse widths of 27msec, 9msec, 5msec, 4msec, 3msec, 2msec, and 1msec. For each of these pulse widths, the AC magnetic field was set at 0.5mT_{PP} , 1.5mT_{PP} and 2.5mT_{PP} to provide sufficient coverage of the operating range of the programmable PEMF generation system. The DC bias was set

to zero and the system was specified for a 100% duty cycle waveform. Throughout this procedure, both the voltage signal from the programmable waveform generator and the amplified signal from the magnetic field sensor were measured and analyzed for magnitude and timing characteristics.

Rather than being solely focused on the characteristics of an individual ramp pulse produced by the programmable PEMF generation system, an additional set of testing conditions has verified the use of different settings for pulse train and duty cycle. Using a duty cycle less than 100% allowed for the incorporation of a pulse train. The following two trials tested two extreme operating conditions of the system. The first trial produced the shortest possible waveform, without having a 100% duty cycle waveform, using a 1msec pulse width and a 95% duty cycle signal with one pulse in the pulse train. The second trial produced the longest possible waveform using a 35msec pulse width and a 10% duty cycle signal with 25 pulses in the pulse train. During these two trials, the DC bias was set to zero. Unlike the previous verification trials, the measurements pertained only to the timing characteristics of the waveform.

6.2.3. Verification of DC Field Operating Range

The verification of the DC field operating range for the programmable PEMF generation system was separated into two sections:

- 1) Verification during the off-time portion of the waveform duty cycle
- 2) Verification during the active portion of the waveform duty cycle

Verification of the DC bias during the off-time portion of the waveform duty cycle used the following procedure. The programmable PEMF generation system was configured for a pulse width of 35msec, a DC bias of zero, and a 50% duty cycle signal with one pulse in the pulse train. The ability of the system to regulate DC bias during the off-time portion of the duty cycle was verified using AC signal strengths of $0.5mT_{PP}$, $1.5mT_{PP}$ and $2.5mT_{PP}$. Both voltage and magnetic field measurements were obtained during this procedure for the AC signal magnitude and the DC bias during the off-time portion of the

waveform duty cycle. Optimally, this DC bias should be centered on the AC component of the waveform.

The DC bias during the active portion of the waveform duty cycle was verified at user-specified DC magnetic field settings of 0mT, 0.625mT and 1.25mT. This procedure used a pulse width of 35msec, an AC field strength of $2.5mT_{PP}$, and a 50% duty cycle signal with one pulse in the pulse train. For both the voltage and magnetic field signal, the measured DC bias was the difference between ground and the middle of the AC waveform.

6.3. Results

6.3.1. AC Field Operating Range

Verification results, shown in tables 6-4, 6-5, and 6-6 for AC magnetic field strengths of $0.5mT_{PP}$, $1.5mT_{PP}$, and $2.5mT_{PP}$ respectively, indicate that the accuracy of the programmable PEMF generation system was reduced at smaller pulse widths. Altering the pulse width from 35msec to 1msec, the average error in the voltage signal increased from 1% to 5% and the average error in the magnetic field increased from 7.6% to 25%.

The accuracy of the programmable waveform generator in producing the desired ramp waveform increased for large magnitude signals. When the AC signal magnitude was varied from $0.5mT_{PP}$ to $1.5mT_{PP}$ to $2.5mT_{PP}$, the average programmable waveform generator error in producing the desired voltage waveform was reduced from 7% to 3% to 1%.

On the other hand, the accuracy of the programmable PEMF generation system in producing the desired magnetic field was reduced for large magnitude signals. The average error in the measured magnetic field as compared to the desired implemented settings varied from 8% to 11% to 16%, when the AC magnetic field magnitude varied from $0.5mT_{PP}$ to $1.5mT_{PP}$ to $2.5mT_{PP}$ respectively.

The effect of coil inductance was better represented through an investigation of the temporal characteristics of the resulting magnetic field. Shown in tables 6-7, 6-8, and 6-9 are the results of the temporal analysis of the magnetic field produced by the programmable PEMF generation system. The total time required for the ramp pulse and reset still complied with ideal values; however the ratio of the ramp pulse to reset duration varied in the magnetic waveform depending upon the selected pulse width. This discrepancy was due to the inductance of the coil set, since the input signal from the programmable waveform generator met specifications. Shown in figure 6-2 is an experimentally measured magnetic waveform representative of this effect of inductance on the performance of the coil set. This investigation indicated that for pulse widths greater than or equal to 9msec, the temporal characteristics of the experimental magnetic field did not vary significantly from the ideal; a ramp waveform possessing a 5% reset duration between individual ramp pulses. When the pulse width was reduced to 5msec, timing deviations from the ideal conditions were evident in the experimental magnetic field. As the pulse width was reduced to 1msec, the observed reset period increased to 20% of the ramp pulse duration. From the results, a minimum reset time of approximately 0.25msec was required for magnetic field magnitudes of 0.5mT_{PP} and 1.5mT_{PP}, and a minimum reset time of approximately 0.31msec was required for a magnetic field magnitude of 2.5mT_{PP}.

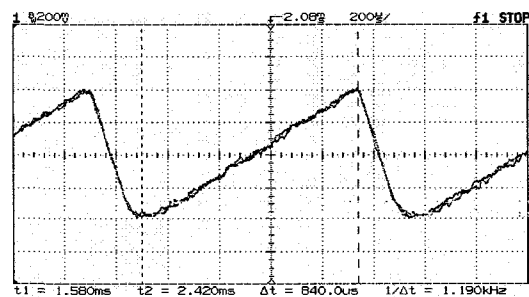


Figure 6-2: Experimental magnetic field waveform configured for a 2.5mT_{PP} AC magnetic field with a 1msec pulse width and 100% duty cycle. Notice how the measured pulse width is only 0.84msec, due to the inductance of the coil set at short pulse widths.

Implemented Settings Based on Calibrated Calculations		Experimental Measurements		Error	
Pulse Width (msec)	Calculated Voltage Signal (mV _{PP})	AC Magnetic Field (mT _{PP})	Voltage Signal (mV _{PP})	AC Magnetic Field	Voltage Signal
1	91	0.42	100	-16%	10%
2	91	0.46	99	-9%	9%
3	91	0.47	99	-7%	9%
4	91	0.47	99	-7%	9%
5	91	0.47	98	-7%	7%
9	91	0.47	98	-5%	7%
27	91	0.47	93	-5%	2%

Table 6-4: Analysis of experimental waveform magnitude configured for an AC magnetic field setting of 0.5mT_{PP}

Implemented Settings Based on Calibrated Calculations		Experimental Measurements		Error	
Pulse Width (msec)	Calculated Voltage Signal (mV _{PP})	AC Magnetic Field (mT _{PP})	Voltage Signal (mV _{PP})	AC Magnetic Field	Voltage Signal
1	273	1.12	275	-25%	1%
2	273	1.29	281	-14%	3%
3	273	1.35	283	-10%	4%
4	273	1.37	283	-9%	4%
5	272	1.39	284	-8%	4%
9	272	1.40	281	-7%	3%
27	272	1.39	278	-8%	2%

Table 6-5: Analysis of experimental waveform magnitude configured for an AC magnetic field setting of 1.5mT_{PP}

Implemented Settings Based on Calibrated Calculations		Experimental Measurements		Error	
Pulse Width (msec)	Calculated Voltage Signal (mV _{PP})	AC Magnetic Field (mT _{PP})	Voltage Signal (mV _{PP})	AC Magnetic Field	Voltage Signal
1	457	1.68	434	-33%	-5%
2	454	1.96	447	-22%	-2%
3	454	2.10	453	-16%	0%
4	454	2.16	456	-14%	0%
5	454	2.21	456	-12%	0%
9	454	2.26	456	-9%	0%
27	454	2.26	453	-10%	0%

Table 6-6: Analysis of experimental waveform magnitude configured for an AC magnetic field setting of 2.5mT_{PP}

Ideal Timing		Timing Measured on Experimental AC Magnetic Waveform	
Ramp (msec)	Reset (msec)	Ramp (msec)	Reset (msec)
1	0.05	0.92	0.13
2	0.10	1.86	0.24
3	0.15	2.90	0.25
4	0.20	3.95	0.25
5	0.25	5.00	0.25
9	0.45	9.00	0.45
27	1.35	27.00	1.35

Table 6-7: Analysis of ramp and reset times for an experimental magnetic field configured with an AC magnitude of $0.5mT_{PP}$

Ideal Timing		Timing Measured on Experimental AC Magnetic Waveform	
Ramp (msec)	Reset (msec)	Ramp (msec)	Reset (msec)
1	0.05	0.87	0.18
2	0.10	1.86	0.24
3	0.15	2.90	0.25
4	0.20	3.95	0.25
5	0.25	5.00	0.25
9	0.45	9.00	0.45
27	1.35	27.00	1.35

Table 6-8: Analysis of ramp and reset times for an experimental magnetic field configured with an AC magnitude of $1.5mT_{PP}$

Ideal Timing		Timing Measured on Experimental AC Magnetic Waveform	
Ramp (msec)	Reset (msec)	Ramp (msec)	Reset (msec)
1	0.05	0.84	0.21
2	0.10	1.82	0.28
3	0.15	2.82	0.33
4	0.20	3.90	0.30
5	0.25	4.92	0.33
9	0.45	9.00	0.45
27	1.35	27.00	1.35

Table 6-9: Analysis of ramp and reset times for an experimental magnetic field configured with an AC magnitude of $2.5mT_{PP}$

Lastly, the programmable PEMF generation system was tested for its duty cycle and pulse train capabilities. Testing the shortest and longest possible waveform, the programmable PEMF generation system achieved the desired characteristics of pulse width, reset time, off time and pulse train. The results of these two trials are shown in table 6-10. When a 95% duty cycle waveform was used by the system, as in the shortest waveform trial, the system was able to achieve the desired temporal characteristics at a pulse width of 1msec. The 95% duty cycle signal is shown in figure 6-3a. However, as previously demonstrated, if the duty cycle was increased beyond 95%, the temporal characteristics of the resulting magnetic field degrade below specifications at a pulse width of 1msec. Figure 6-3b illustrates the pulse train portion of the longest possible waveform, containing 25 pulses. Although not shown, this pulse train was followed by 7.88 seconds of inactivity, corresponding to the off-time portion of the 10% duty cycle signal.

Waveform Temporal Settings			Experimental Timing Measurements			
Pulse Width (msec)	Duty Cycle (%)	Pulse Train (pulses / train)	Pulse Width (msec)	Reset (msec)	Offtime (msec)	Pulse Train (pulses / train)
1	95	1	1	0.05	0.053	1
35	10	25	35	1.80	7880	25

Table 6-10: Experimental results for the duty cycle and pulse train verification using the shortest and longest PEMF waveforms

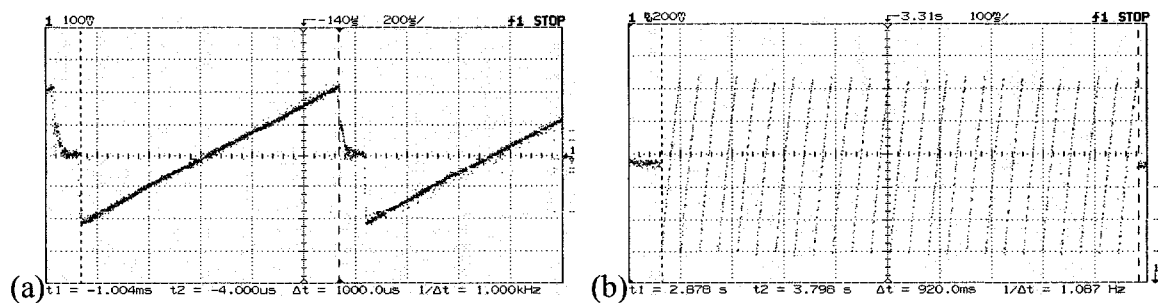


Figure 6-3: Magnetic field waveforms of (a) the shortest pulse train and (b) the longest pulse train

6.3.2. DC Field Operating Range

The programmable PEMF generation system was tested for its ability to control the DC component of both the voltage waveform and resulting magnetic field. Control of the DC waveform was divided into the off-time and active portions of the waveform duty cycle.

Implemented Settings Based on Calibrated Calculations		Experimental Measurements				DC Bias Error During Duty Cycle Off-time	
		Deviation of DC Bias from Center of AC Waveform		AC Field Magnitude			
AC Magnetic Field (mT _{PP})	Calculated AC Voltage Signal (mV _{PP})	Magnetic Field (mT)	Voltage Signal (mV)	Magnetic Field (mT _{PP})	Voltage Signal (mV _{PP})	Magnetic Field	Voltage Signal
0.5	91	-0.02	-2.5	0.47	95	-7%	-5%
1.5	272	-0.02	-1.0	1.36	270	-2%	-1%
2.5	454	-0.01	0.0	2.18	450	-1%	0%

Table 6-11: Experimental results for the DC bias produced by the programmable PEMF generation system during the off-time portion of the waveform duty cycle. The DC bias was set to zero during testing and should be centered on the AC waveform.

Testing of the DC bias during the off-time portion of the waveform duty cycle indicated good performance. The extent to which the measured DC bias deviated from the center of the AC waveform is listed in table 6-11. An error calculation relating this deviation to the peak AC field magnitude indicated an average error of 2% for the programmable waveform generator voltage and 3.5% for the resulting magnetic field. The most error occurred with an AC field setting of 0.5mT_{PP}, due to the bad SNR of the waveform. Figure 6-4 illustrates, for an AC magnetic field of 2.5mT_{PP} and a DC bias of 1.25mT, the centering of the DC magnetic field on the AC magnetic field during the off-time portion of the waveform duty cycle.

Testing of the DC bias during the active portion of the waveform duty cycle also indicated good performance, as shown in table 6-12. The average error for the DC bias was 4% for the voltage waveform and 11% for the magnetic field. No error calculation was possible for a zero DC bias setting; however the obtained values of 3mV and 0.01mT are indicative of low error. The error was larger for the magnetic field than the voltage

waveform, due to the 5% error in the magnetic field-to-voltage conversion factor previously observed in the AC magnetic field at large pulse widths. The same conversion factor was used for both the AC and DC magnetic field calculations. An example of DC bias during the active portion of the waveform duty cycle is illustrated in figure 6-4.

Implemented Settings Based on Calibrated Calculations		Experimental Measurements		Error	
Voltage Signal (mV)	DC Magnetic Field (mT)	Voltage Signal (mV)	DC Magnetic Field (mT)	Voltage Signal	DC Magnetic Field
0	0	3	-0.01	N/A	N/A
114	0.625	108	0.56	-5%	-11%
227	1.25	221	1.11	-3%	-11%

Table 6-12: Experimental results for the DC bias produced by the programmable PEMF generation system during the active portion of the waveform duty cycle

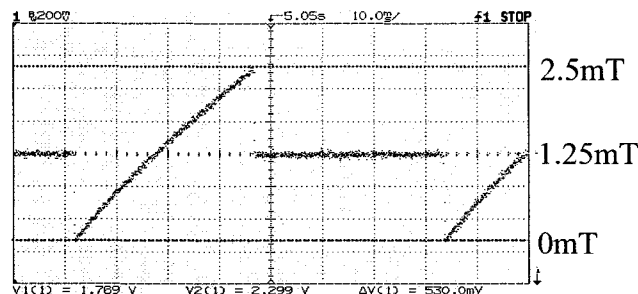


Figure 6-4: Magnetic waveform measurement showing DC bias during both the active and off-time portions of the waveform duty cycle. The signal was configured for an AC magnetic field strength of 2.5mT_{pp} and a DC component of 1.25mT.

6.4. Discussion

The testing procedure progressed through three stages: (1) the implemented settings of the programmable waveform generator were approved by the user, (2) the voltage output of the programmable waveform generator was verified with the implemented settings, and (3) the magnetic field produced by the coil set was verified with the implemented settings.

In the majority of the tested magnetic field conditions, the programmable waveform generator specified the appropriate implemented settings. Since the programmable

waveform generator is a digital instrument, it imposed a finite resolution to the settings that could be programmed. Throughout the testing procedure, there was only the occasional deviation from the user-specified settings. For example, at a 35msec pulse width, a magnetic field setting of $0.50\text{mT}_{\text{PP}}$ was reconfigured to $0.52\text{mT}_{\text{PP}}$; or at a 1msec pulse width, a magnetic field setting of $2.50\text{mT}_{\text{PP}}$ was reconfigured to $2.52\text{mT}_{\text{PP}}$. However these deviations were small and corresponded to a 4% and 0.8% change respectively.

The deviation at the large pulse width was due to two reasons. First, there was a programming error for the $10\text{k}\Omega$ digital potentiometer in the integrator circuit that occurred when the required resistance exceeded the capability of the device. After updating the firmware, the error in the implemented AC magnetic field setting, at the 35msec pulse width, was reduced to 2%. The system could still not implement the settings for a 0.5mT_{PP} AC magnetic field with a pulse width of 35msec because this configuration required an integration resistance larger than the capability of the system. As a result of the voltage signal calibration, integration resistances larger than that designed for the system are required to achieve the full operational range of the AC waveform.

At small pulse widths, deviations in the implemented settings occurred because the change in integrator resistance between pulse width settings challenged the resolution of the programmable waveform generator. Since this is the nature of the equipment, it can not be easily accommodated for without a redesign of the hardware. Fortunately, the error from this limitation was less than 1% between the user-specified and implemented AC field setting on the programmable waveform generator.

The error between the desired implemented setting and experimentally measured AC voltage magnitude was a maximum of 10%. Figure 6-5 shows the error measurements for the output voltage signal that encompassed the entire AC field range of the programmable waveform generator. Obtaining the measurements for this analysis had an error of $\pm 10\text{mV}$, due to the $\pm 5\text{mV}$ signal noise detected by the oscilloscope. This corresponds to a

2% to 11% error in the overall measurement depending on whether a 2.5mT_{PP} (454mV_{PP}) or 0.5mT_{PP} (91mV_{PP}) AC field setting was configured into the system. The error between desired settings and experimentally measured voltage waveforms can be largely accounted for by the error in obtaining the measurements with the oscilloscope. It was less than 10% for the 0.5mT_{PP} signal and less than 5% for the 2.5mT_{PP} signal.

On average, the programmable waveform generator was overestimating the required voltage magnitude throughout the operational range of the system. As the magnetic field setting was increased, so did the accuracy of the system. According to the average error, if a 3% reduction was incorporated into the AC voltage system calibration, the performance of the programmable waveform generator would improve for magnetic field settings of 0.5mT_{PP} to 1.5mT_{PP}, but decrease for 2.5mT_{PP} settings. However, since there was a significant error in obtaining the measurements for this analysis, the effectiveness of these system modifications will be investigated in future designs.

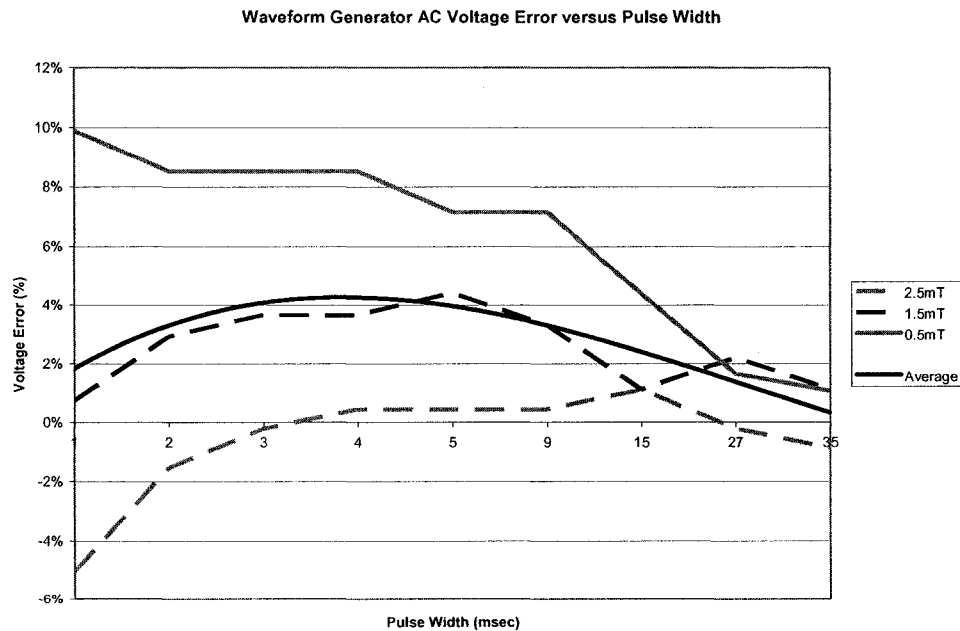


Figure 6-5: AC voltage error of the programmable waveform generator versus pulse width

The accuracy of the DC bias for the voltage waveform could be improved during the active portion of the waveform duty cycle if a 4% increase was incorporated into the DC voltage system calibration. In regards to the off-time portion of the waveform duty cycle, the system was very accurate because it took advantage of the calibration factors for the AC waveform.

The error between the desired implemented setting and experimentally measured AC magnetic field strength was a maximum of 32%. As shown in figure 6-6, the error was increased when the magnetic field strength was decreased. In all of the test conditions, the measured magnetic field was less than the desired setting. At small pulse widths, this error increased due to the inductance of the coil set. Inductance reduced the magnitude and rate of change of the current that can flow through the coil. This affected the resulting magnetic field and reduced the accuracy of the programmable PEMF generation system. At pulse widths greater than 15msec, the effect of coil inductance was no longer significant. However, there was still an average error of 5% to 7% between desired settings and measured magnetic field strengths.

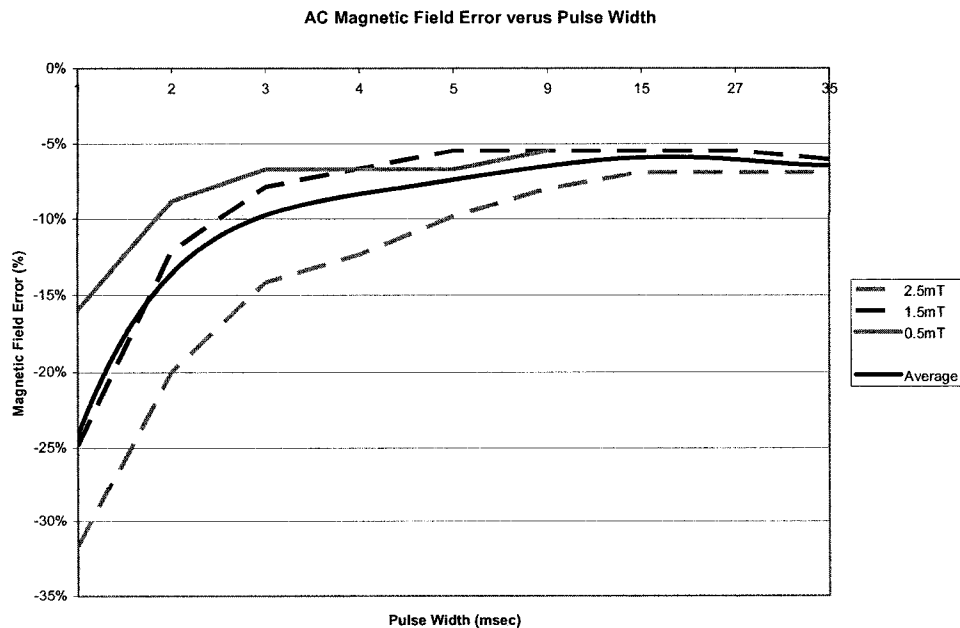


Figure 6-6: AC magnetic field error by the coil set versus pulse width

This discrepancy between the desired setting and measured magnetic field strength could be due to sensor calibration, waveform measurement, and current and magnetic field modelling. The output of the magnetic field sensor is regulated by characteristics of sensitivity, linearity and symmetry that are dependant upon the supply voltage and ambient operating temperature of the device. Since the supply voltage was increased by 10% from the nominal voltage for the sensor, if temperature effects are neglected, the ratiometric sensitivity should also increase by 10%. Unfortunately, information provided on the data sheet does not clearly explain this effect in regards to temperature and supply voltage. It is possible that the sensor sensitivity was increased by only 1.25%. As a result, the measured magnetic field strengths could be increased up to 10%, thereby greatly reducing the error when compared to the desired settings.

In regards to the amplified sensor signal, there was a noise level of approximately $\pm 25\text{mV}$ or $\pm 0.05\text{mT}$. Hence, the error in obtaining a measurement is $\pm 0.1\text{mT}$; 4% to 20% for an AC magnetic field range of 2.5mT_{PP} to 0.5mT_{PP} respectively. Although the instrumentation amplifier has DC and AC common mode rejection ratios of approximately 90dB to 110dB, it will amplify any differential input signal. Since the noise is inherently random, it will remain as part of the differential signal.

The modelling of the magnetic field used several assumptions about the coil set. In reality, each of the coil turns has a slightly different radius and vertical placement within the coil set. The coil current applied to this magnetic field model ignored the effect of mutual inductance in the coil set on the resulting current magnitude. The removal of these assumptions should increase the accuracy of the modelled magnetic field. It is possible to implement this advanced model through a reprogramming of the firmware on the programmable waveform generator. However, a simpler method to increase the AC magnetic field accuracy to within 10% of expected values is to incorporate the average error represented in figure 6-6. Based on experimental analysis, this information could skew the configuration of the magnetic field depending upon the selected pulse width of the ramp waveform.

The magnitude of the DC magnetic field during the active portion of the waveform duty cycle could be increased by 7% to improve the accuracy of the programmable PEMF generation system. This was equivalent to the error in the AC magnetic field at large pulse widths. On the other hand, the DC magnetic field measured during the off-time portion of the waveform duty cycle corresponded to the desired settings.

Chapter 7

7. Application of the Programmable PEMF Generation System

A programmable PEMF generation system has been designed and verified according to specifications. The purpose of this instrument was to reduce to the work time of laboratory technicians to set up experiments investigating how PEMFs can alter the behaviour of chondrocytes. Many experimental protocols can demonstrate the usefulness of this programmable PEMF generation system. One of these experiments, described in this thesis, investigated the role of calcium ion resonance in transmembrane channels to regulate *in vitro* cultured human chondrocyte morphology. This chapter describes the experimental setup and outcome of this investigation.

7.1. Objectives

The primary objective of this experimental protocol was to demonstrate an application of the programmable PEMF generation system as an instrument to expose cultured human chondrocytes to user-specified PEMFs.

The PEMF settings used to demonstrate this application led to the secondary objective. The secondary objective was to determine whether the resonance of calcium ions in transmembrane channels could explain the morphological changes, previously observed in chapter 3, on *in vitro* cultured human chondrocytes exposed to specific PEMFs.

7.2. Methodology

7.2.1. Previous Laboratory Evidence

The results of chapter 3 demonstrated that certain PEMF exposure conditions can alter the morphology of *in vitro* cultured human chondrocytes. While exposed to specific PEMF conditions, approximately 35% of the cultured chondrocytes adopted a spherical morphology instead of the typical stellate morphology. Calcium ions are important for the regulation of cell shape. In brief, an influx of calcium ions weakens the actin cortical

meshwork and initiates cell contraction by the actomyosin system [70]. The hypothesis is that exposing chondrocytes to PEMFs, configured by the model of ion parametric resonance, can change cell morphology by altering the flux of calcium ions across transmembrane channels. The theory of ion parametric resonance was described in chapter 2.

7.2.2. Experimental Setup

This investigation of ion parametric resonance applied three experimental PEMF conditions to *in vitro* cultured human chondrocytes. These experimental conditions were created by the programmable PEMF generation system. The primary waveform produced by this system was a ramping magnetic field. The ramping magnetic field had a 100% duty cycle, meaning that the pulse train was continuous. During these experimental trials, the magnitude of the DC magnetic field was set at 1mT. The AC magnetic field strength and the duration of the ramp pulse were varied between trials to validate equations 2-1 and 2-2 for ion parametric resonance. These equations used a q/m ratio for the Ca^{2+} ion as specified by Grande [134]. It was hypothesized that the resonance of calcium ions in transmembrane channels during PEMF exposure will change chondrocyte morphology.

As shown in table 7-1, the experimental protocol used one resonant and two non-resonant electromagnetic conditions for the calcium ion. According to equation 2-1, the resonance of calcium ions should occur at an AC magnetic field strength of $1.84mT_{PP}$ and a frequency of 769Hz. Taking into account the 5% reset time for the ramp waveform, this frequency corresponded to an implemented ramp pulse width of 1.24msec. This resonant exposure condition used for trial A should promote a change in chondrocyte morphology. The remaining two experimental trials (B & C) were non-resonant conditions that tested the validity of ion parametric resonance by varying the ramp pulse width and AC magnetic field strength respectively. The outcome of these two trials was not predicted to change chondrocyte morphology. In trial B, the duration of the ramp pulse was reduced to 1.86msec, corresponding to an effective frequency of 512Hz, while the AC magnetic field was maintained at the original strength of $1.84mT_{PP}$. This tested the validity of equation 2-1, in the model of ion parametric resonance, since the specified PEMF

corresponded to a frequency index of 1.5. In trial C, the AC magnetic field strength was reduced to $0.5mT_{PP}$, while the ramp pulse width remained at 1.24msec. This tested the validity of equation 2-2, since the reduced AC magnetic field strength corresponded to a reduced probability of calcium ion resonance. This set of three experimental PEMF conditions, as outlined in table 7-1, was repeated twice to improve the accuracy of the results.

PEMF Condition	AC Magnetic Field (mT_{PP})	DC Magnetic Field (mT)	Pulse Width (msec)
A (Resonant)	1.84	1.00	1.24
B (Non-Resonant)	1.84	1.00	1.86
C (Non-Resonant)	0.50	1.00	1.24

Table 7-1: Desired magnetic field settings for the investigation of ion parametric resonance

Chondrocyte cultures were established using the same preparation procedure as the experiments of chapter 3. Prior to applying the PEMF treatment, chondrocytes were reseeded at the desired density (100,000 cells / 30mm dish) after which they were incubated for twenty-four hours. From the same batch of cultured chondrocytes, both a control and experimental dish were created for each experimental trial. The experimental chondrocyte culture dish was placed at the center of the coil set in an incubated environment of 37°C and 5% CO₂. The programmable PEMF generation system was activated to produce the desired electromagnetic field condition and the experimental culture dish was exposed for six hours. The control chondrocyte culture dish was positioned in the corner of the same incubator as the experimental dish; however the PEMF was not detectable at this location.

Both the experimental and control cells were monitored with a light microscope at exposure times of 0hr, 3hr and 6hr. The resulting pictures were cropped to an area of 1.25mm x 1.25mm. Upon completion of the experimental trial, these microscope pictures were visually observed for significant changes in morphology between the control and experimental cultures during the six hour exposure period. If a significant change in chondrocyte morphology was visually detected, as a result of PEMF exposure, the

pictures would be further analysed using ImageJ software. Use of this software would allow an in-depth analysis of individual cells in the culture. Cells would be individually labelled, and characterized according to morphology and surface contact area. Previous experimentation, outlined in chapter 3, provided an expected change in morphology from stellate to spherical, accompanied by a decrease in surface contact area, if the cells were to be affected by the PEMF exposure.

Microscope pictures were also obtained twenty-four hours after the completion of PEMF exposure. An assessment of chondrocyte viability, based upon cell proliferation, determined whether PEMF exposure had long-term effects on biological processes.

7.3. Results

The primary objective was to demonstrate the application of the programmable PEMF generation system for exposing cultured chondrocytes to a user-specified pulsed electromagnetic field. Although the accuracy of the magnetic field generation degraded at small pulse widths, the specified electromagnetic conditions were still achieved by the system. However, the settings as specified on the system were not the same as the measured magnetic field. The programmed PEMF settings were altered from the original values until the desired measurements were obtained. Table 7-2 lists the implemented settings required to achieve the desired magnetic field conditions. The implemented settings varied the most from the original settings when defining the AC magnetic field. At short pulse widths, the inductance of the coil set reduced the current magnitude and hence the resulting AC magnetic field. In order to achieve a magnetic field strength of $1.84\text{mT}_{\text{PP}}$ at a pulse width of 1.24msec, the maximum programmable AC magnetic field strength of the programmable waveform generator had to be increased from 2.5mT_{PP} to 2.6mT_{PP} .

Regardless of the difficulty in obtaining the desired magnetic field, this experimental procedure was able to demonstrate an application of the programmable PEMF generation system. The cultured human chondrocytes could be placed within the coil set and exposed to a consistent electromagnetic field for the duration of these experiments.

PEMF Condition	Implemented Settings		
	AC Magnetic Field (mT _{pp})	DC Magnetic Field (mT)	Pulse Width (msec)
A (Resonant)	2.60	0.97	1.24
B (Non-Resonant)	2.30	1.00	1.86
C (Non-Resonant)	0.60	1.03	1.24

Table 7-2: Implemented user settings for the programmable PEMF generation system to achieve experimental conditions A, B and C

The secondary objective of these experiments was to investigate the resonance of calcium ions in transmembrane channels as the mechanism used to alter the morphology of chondrocytes. Microscope pictures obtained during the experimental exposure conditions are shown below. As a precursor, the experimental results were the same for all of the testing conditions (trials A, B and C in table 7-1). Therefore an overview of each observation time is provided which applied to all testing conditions.

The chondrocytes were monitored prior to their exposure to an electromagnetic field. As shown in figure 7-1, the overall chondrocyte morphology was stellate or spindle for both the control and experimental cultures. This morphology is typical of chondrocytes that are attached to the surface of a Petri dish, since they will extend their cellular processes.

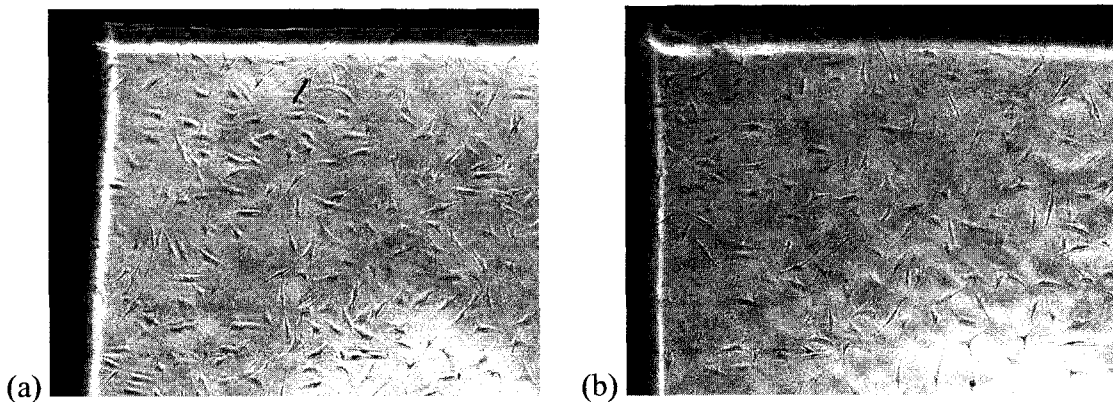


Figure 7-1: Microscope pictures of the chondrocytes prior to PEMF exposure for (a) the control dish and (b) the experimental dish

Examination of the microscope pictures obtained after three hours of PEMF exposure (figure 7-2) yielded the same observations for all three experimental conditions. Regardless of whether the experimental chondrocyte cultures were exposed to a resonant or non-resonant electromagnetic field, there was no significant morphological change when compared to the control cultures. As shown in figure 7-2, the overall morphology of both the control and experimental chondrocyte cultures was either stellate or spindle.

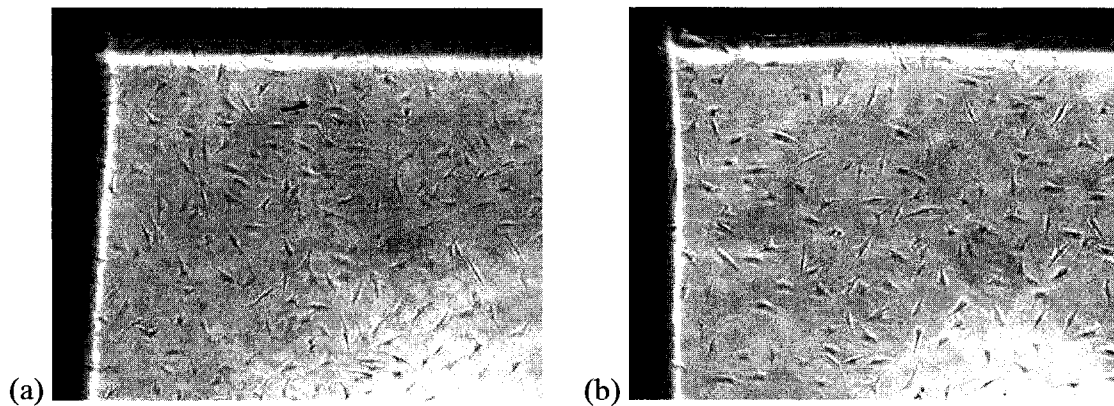


Figure 7-2: Microscope pictures of the chondrocytes after three hours of PEMF exposure for (a) the control dish and (b) the experimental dish

After six hours of PEMF exposure, the microscope pictures yielded the same observation for all three experimental conditions. As shown in figure 7-3, there was no significant change in chondrocyte morphology when the experimental cultures were compared to the control cultures. Overall, both chondrocyte cultures possessed either a stellate or spindle morphology. There was the occasional chondrocyte that possessed a spherical morphology in both the control and experimental cultures. Unfortunately this effect could not be attributed to the PEMF exposure since it was not specific to the experimental culture. Both the control and experimental chondrocyte cultures were temporarily removed from the controlled environment of the incubator to obtain microscope pictures. This also caused the concentration of CO₂ within the incubator to drop from its regulated value of 5%. Previous experimentation by this laboratory has demonstrated that a low CO₂ environment caused chondrocytes to adopt a spherical morphology.

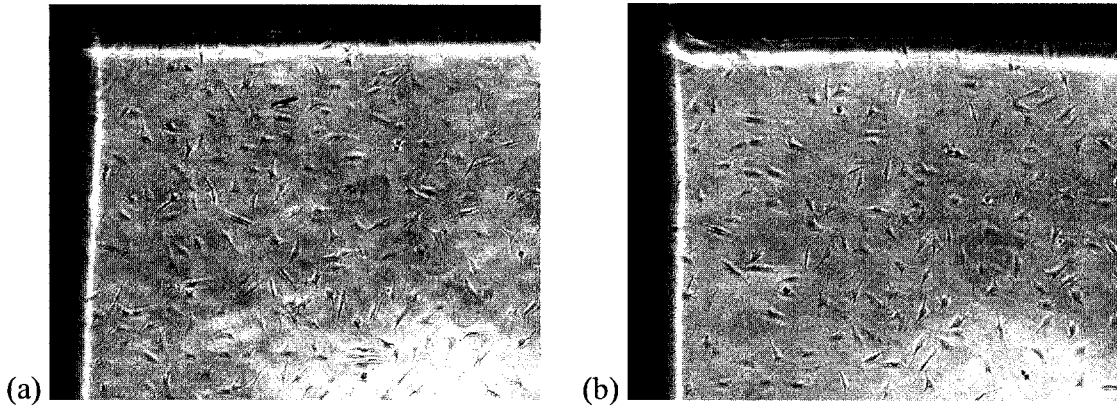


Figure 7-3: Microscope pictures of the chondrocytes after six hours of PEMF exposure for (a) the control dish and (b) the experimental dish

Lastly, the chondrocytes were observed twenty-four hours post exposure to assess cell viability. Microscope pictures for both the control and experimental cultures indicated an increase in cell density during the twenty-four hours since PEMF exposure. As shown in figure 7-4, the extent of cell proliferation in the experimental culture is approximately the same as in the control culture. As a result, PEMF exposure did not have any long-term effects on biological processes in the chondrocyte.

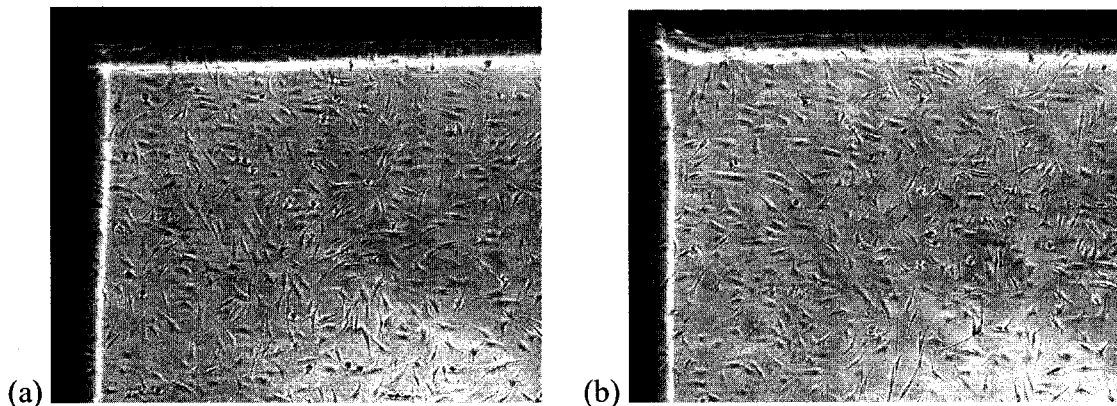


Figure 7-4: Microscope pictures of the chondrocytes twenty-four hours after removal from the PEMF exposure for (a) the control dish and (b) the experimental dish

7.4. Conclusion

Overall, the primary objective for this experiment was achieved. The programmable PEMF generation system was demonstrated to be an effective tool for exposing cultured human chondrocytes to an electromagnetic field. The system was easy to program by the user and under the majority of settings produced the desired magnetic field without further adjustments.

In regards to the secondary objective, the morphology of *in vitro* cultured human chondrocytes was unaffected by PEMF exposure tuned to calcium channel resonance. As a result, the theory of ion parametric resonance, applied to calcium ions in transmembrane channels, could not predict the chondrocytes change to a spherical morphology during exposure to specific PEMF conditions.

Chapter 8

8. Conclusion and Future Recommendations

The objectives of this research were to explore the design and application of a programmable PEMF generation system for osteoarthritis research. This work completed the design of a microprocessor controlled PEMF system and demonstrated the use of the designed system in exposing cultured chondrocytes to a user-specified electromagnetic field. In a laboratory environment the use of this system reduced the amount of hardware required to generate the desired electromagnetic field. As well, the laboratory technician and cell biologist can focus on performing the desired chondrocytic tests with the exposed cells, rather than the configuration of the electrical components. This system receives the user specifications through a computer connection and automates the generation electromagnetic fields using custom firmware for a microcontroller that configures the hardware components.

8.1. Conclusion

This thesis introduced the issue of osteoarthritis and the need for a programmable PEMF generation system to assist studies in the research environment. A literature review encompassed human joint anatomy, cartilage repair, and cellular exposure to static electric, static magnetic and electromagnetic fields. The discussed literature provided an understanding to the physiology of cartilage and the issues of osteoarthritis. This provided justification to the current research activities underway throughout the world, in attempt to find a better non-invasive treatment for osteoarthritis.

A series of experiments were performed to investigate the effects of chondrocytes under exposure to PEMFs. The results demonstrated that under certain exposure conditions, *in vitro* cultured human chondrocytes experience a change in their morphology. The result of this study indicated a general trend from a stellate to spherical morphology and was published in the Journal of Medical and Biological Engineering and Computing [135].

To reduce the amount of time to set the electronic equipment to perform experiments, a programmable PEMF generation system was proposed that automates the generation a ramp electromagnetic field. The user can specify electromagnetic parameters within a predetermined operating range for AC magnetic field strength ($0.5mT_{PP}$ to $2.5mT_{PP}$), DC magnetic field strength (0mT to 1.25mT), pulse width (1msec to 35msec), duty cycle (10% to 100%) and pulse train (1 to 25 pulses per train).

Before the system was designed, a theoretical model was established for the electromagnetic field produced by a current flow through a coil set. The theoretical model started with a simplified on-axis single coil magnetic field model and then expanded to calculate the magnetic field within the entire spatial void of a coil pair. From this resulting model, the uniformity of the magnetic field used to expose cultured chondrocytes was assessed. Lastly, this electromagnetic field model determined the theoretically induced electric fields.

The design of the programmable PEMF generation system can be divided into three main components: coil set, coil driver and programmable waveform generator. Whereas the development of the coil set and coil driver was faced with only hardware issues, the development of the programmable waveform generator was represented in terms of both hardware and software issues.

The resulting system was tested for its ability to meet the specified operating range of the generated electromagnetic field. The programmable PEMF generation system underwent a calibration procedure to best align the theoretical and experimental results for both the programmable waveform generator output signal and the generated magnetic field. Following this calibration, the system was verified across both the AC and DC field operating ranges. Due to the decreased SNR at the minimum AC magnetic field setting of $0.5mT_{PP}$, the error between desired and measured voltage signals from the programmable waveform generator reached 10%. Considering only the measurements obtained at $1.5mT_{PP}$ and $2.5mT_{PP}$ settings reduced the error to a maximum of 5%. As a general trend,

the accuracy of the programmable waveform generator was reduced at smaller pulse widths.

In terms of the generated magnetic field, the error between desired and experimental AC magnetic field measurements reached a maximum of 32%. In all of the test conditions, the measured magnetic field was less than the theoretical value. At a small pulse width, this error became more significant due to the increased contribution from the inductance of the coil set. At pulse widths greater than 15msec, the influence from the inductance of the coil set was insignificant. However, there was still an average error of approximately 5% to 7% between desired and measured magnetic field values.

Lastly, the programmable PEMF generation system was used for its application in osteoarthritis research. The system was demonstrated as a tool to expose *in vitro* cultured human chondrocytes to user-specified pulsed electromagnetic fields. The resonance of calcium ions in transmembrane channels was suggested as a mechanism to explain the previously observed changes in chondrocyte morphology due to PEMF exposure. Unfortunately, experimental results did not support this prediction.

8.2. Future Recommendations

The design and application of the programmable PEMF generation system could be enhanced with the following recommendations. These recommendations relate to system accuracy, system portability, and the future focus of the cultured chondrocyte studies.

In terms of system accuracy, there are three general recommendations:

- 1) The accuracy of the proposed multiple-coil PEMF model can be improved by several methods. One method is to eliminate average coil dimensions and incorporate the actual coil thickness and height. The other method is to take into account the effect of coil inductance on the calculated input current to this PEMF model.
- 2) The incorporation of real-time feedback from a magnetic field sensor will permit the microcontroller to automatically adjust the settings of the connected hardware to match desired with experimental values.
- 3) A redesign of the coil set should be considered to optimize characteristics of resistance and inductance, and to maximize the performance of the programmable PEMF generation system.

In terms of system portability, there are two general recommendations:

- 1) Onboard power management should be established for the coil driver, thereby removing dependence on the proper setting of an external power supply. A power adapter for a 120V wall socket could also be established for this system. The incorporation of these features will reduce the cost and size of the system, and improve portability in a clinical setting by eliminating the need for an external power supply.

- 2) The programmable waveform generator can also be powered from a battery pack; useful for clinical applications with patients. Removing power cables between the coil driver and programmable waveform generator is a good design choice since it separates the power supplies for the digital and analog circuits.

In terms of the future focus of the *in vitro* cultured human chondrocyte studies, there are six general recommendations:

- 1) Examining the effect of PEMFs on chondrocyte morphology has limited application, since it is not clear how they are affected. Rather experiments should examine the effect of PEMF exposure on protein synthesis. Monitoring the synthesis of collagen and proteoglycan by chondrocytes can be used to establish non-invasive treatments for osteoarthritis.
- 2) Operating windows for PEMF exposure can be reinvestigated using protein analysis. The main operating windows are focused on the range of frequency, and AC and DC magnetic field strength that optimize the synthesis of proteins by chondrocytes.
- 3) Establish the minimal exposure energy to alter chondrocyte behaviour. A minimal exposure energy would investigate the waveform parameters of magnetic field strength, duty cycle and pulse train. This will assist the development of a portable system for future clinical applications.
- 4) The ability of PEMFs to control the migration of chondrocytes has not been investigated. Future experiments can establish whether the electric fields induced by the programmable PEMF generation system are sufficient for the regulation of this behaviour.
- 5) Modify the incubator environment to include a microscope viewing port. This will increase the reliability of experiments, since the cell cultures are not moved

during exposure for the purpose of obtaining pictures. As well, video microscopy could provide a time-elapsd representation of either morphological or migrational effects on chondrocytes due to PEMF exposure.

- 6) Transition from the use of *in vitro* cultured human chondrocytes grown in a monolayer to a cartilage matrix. In a pressure controlled environment, a cartilage matrix is representative *in vivo* human cartilage tissue. Success at the level of cartilage matrices will assist the transfer of PEMF experiments to clinical trials on patients with osteoarthritis in their joints.

References

- 1 NIAMS/National Institutes of Health (July 2002) Handout on Health: Osteoarthritis. NIH Publication No. 02-4617
- 2 The Arthritis Society (2006) Osteoarthritis: Quick Facts. [Online]. Available: <http://www.arthritis.ca/types%20of%20arthritis/osteoarthritis/quick%20facts/default.asp?s=1>
- 3 NHIS (2006) Data Source: 2003–2005. MMWR 55:1089-92
- 4 Lawrence RC, Helmick CG, Arnett FC, Deyo RA, Felson DT, Giannini EH, Heyse SP, Hirsch R, Hochberg MC, Hunder GG, Liang MH, Pillemer SR, Steen VD, Wolfe F (1998) Estimates of the Prevalence of Arthritis and Selected Musculoskeletal Disorders in the United States. *Arthritis & Rheumatism* 41:778-99
- 5 Arthritis Foundation (2005) Arthritis Prevalence: A Nation in Pain. [Online]. Available: http://www.arthritis.org/conditions/Fact_Sheets/Arthritis_Prev_Fact_Sheet.asp
- 6 CDC (2001) Prevalence of disabilities and associated health conditions among adults – United States, 1999. MMWR 50:120-5
- 7 CDC (2004) Update: Direct and Indirect Costs of Arthritis and Other Rheumatic Conditions – United States, 1997. MMWR 53:388-9
- 8 Bassett CAL, Mitchell SN, Gaston SR (1982) Pulsing Electromagnetic Field Treatment in Ununited Fractures and Failed Arthrodeses. *JAMA* 247:623-8
- 9 Faensen M, Breul R (2001) Prospektive multi-centric study for the treatment of Gonarthrosen (Kellgren II and III) with the PST. *Orthopedic practice* 37:701-9
- 10 Markoll R, Da Silva Ferreira D, Toohil T (2004) Pulsed Signal Therapy for the treatment of musculoskeletal conditions: a millennium paradigm. *Journal of Rheumatology* 7:292-305
- 11 Zizic TM, Hoffman KC, Holt PA, Hungerford DS, O'Dell JR, Jacobs MA, Lewis CG, Deal CL, Caldwell JR, Cholewczynski JG, Free SM (1995) The Treatment of Osteoarthritis of the Knee with Pulsed Electrical Stimulation. *Journal of Rheumatology* 22:1757-61
- 12 Mont MA, He DY, Jones LC, Hungerford DS, Hoffman DS, Zizic TM, Caldwell JR (2004 March) The Use of Pulsed Electrical Stimulation to Defer Total Knee Arthroplasty in Patients with Osteoarthritis of the Knee. presented at American Academy of Orthopaedic Surgeons
- 13 Hinsenkamp M, Bourgois R, Bassett CAL, Chiabrera A, Burny F, Ryaby J (1978) Electrical stimulation of fracture repair. *Acta Orthop Belg* 44:671
- 14 Brighton CT, Friedenber ZB, Mitchell EI (1977) Treatment of non-union with constant direct current. *Clin Orthop* 124:106-123
- 15 Hinsenkamp M, Burny F, Jedwab J, Bourgois R (1978) Corrosion of implants during electric stimulation of fracture healing. in *Stimulation of Bone Growth and Repair*, ed. F Burny, E Herbst, M Hinsenkamp. Berlin, Springer-Verlag:77-83
- 16 Hawkins D (2004, Jan) Biomechanics of Musculoskeletal Tissues. [Online]. Available: <http://www.exb.ucdavis.edu/faculty/hawkins/126site/index.htm>

- 17 Mow VC, Guo XE (2002) Mechano-Electrochemical Properties of Articular Cartilage: Their Inhomogeneities and Anisotropies. *Annu Rev Biomed Eng* 4:175-209
- 18 Stockwell R (1979) *Biology of cartilage cells*. Great Britain, Cambridge University Press
- 19 Bush P, Huntley J, Brenkel I, Hall A (2003) The shape of things to come: chondrocytes and osteoarthritis. *Clin Invest Med* 26:249-51
- 20 Frank EH, Grodzinsky AJ (1987) Cartilage electromechanics. I. Electrokinetic transduction and the effects of electrolyte pH and ionic strength. *J Biomech* 20:615-27
- 21 Frank EH, Grodzinsky AJ (1987) Cartilage electromechanics. II. A continuum model of cartilage electrokinetics and correlation with experiments. *J Biomech* 20:629-39
- 22 Trock D, Bollet A, Markoll R (1994) The Effect of Pulsed Electromagnetic Fields in the Treatment of Osteoarthritis of the Knee and Cervical Spine. Report of Randomized, Double Blind, Placebo Controlled Trials. *Journal of Rheumatology* 21:1903-11
- 23 Lai WM, Sun DD, Ateshian GA, Guo XE, Mow VC (2002) Electrical signals for chondrocytes in cartilage. *Biorheology* 39:39-45
- 24 Lai WM, Hou JS, Mow VC (1991) A triphasic theory for swelling and deformation behaviour of articular cartilage. *J Biomech Engng* 113:245-58
- 25 Meachim G, Collins DH (1962) Cell counts of normal and osteoarthritic articular cartilage in relation to the uptake of sulphate ($^{35}\text{SO}_4$) in vitro. *Ann rheum Dis* 21:45-50
- 26 Vignon E, Arlot M, Patricot LM, Vignon G (1976) The cell density of human femoral head cartilage. *Clin Orthop* 121:303-8
- 27 Stockwell RA (1967) The cell density of human articular and costal cartilage. *J Anat* 101:753-63
- 28 Mathews MB, Glagov S (1966) Acid mucopolysaccharide patterns in aging human cartilage. *J clin Invest* 45, 1103-11
- 29 Stockwell RA, Meachim G (1973) The chondrocytes. In *Adult articular cartilage*, ed. MAR Freeman. London, Pitman Medical:51-99
- 30 Barnett CH, Davies DV, MacConaill MA (1961) *Synovial joints. Their structure and mechanics*. London: Longmans, Green
- 31 Davies DV, Barnett CH, Cochrane W, Palfrey AJ (1962) Electron microscopy of articular cartilage in the young adult rabbit. *Ann rheum Dis* 21:11-22
- 32 Langelier E, Suetterlin R, Hoemann C, Aebi U, Buschmann M (2000) The Chondrocyte Cytoskeleton in Mature Articular Cartilage: Structure and Distribution of Actin, Tubulin, and Vimentin Filaments. *Journal of Histochemistry and Cytochemistry* 48:1307-20
- 33 Beneke G (1973) Cell density in cartilage and DNA content of the cartilage cells dependent on age. in *Connective tissue and ageing*, ed. HG Vogel. Amsterdam, Excerpta Medica:91-4
- 34 Stockwell, RA (1971) Cell density, cell size and cartilage thickness in adult mammalian articular cartilage. *J Anat* 108:584

- 35 Bush PG, Hall AC (2003) The volume and morphology of chondrocytes within non-degenerate and degenerate human articular cartilage. *Osteoarthritis Cartilage* 11:242-51
- 36 Mankin HJ (1964) Mitoses in articular cartilage of immature rabbits. *Clin Orthop* 34:170-83
- 37 Palfrey AJ, Davies DV (1966) The fine structure of chondrocytes. *J Anat* 100:213-26
- 38 Weiss C, Rosenberg L, Helfet AJ (1968) An ultrastructural study of normal young adult human articular cartilage. *J Bone Joint Surg* 50A:663-74
- 39 Janmey PA, Euteneuer U, Traub P, Schliwa M (1991) Viscoelastic properties of vimentin compared with other filamentous biopolymer networks. *J Cell Biol* 113:155-60
- 40 Meachim G, Roy S (1967) Intracytoplasmic filaments in the cells of adult human articular cartilage. *Ann rheum Dis* 26:50-8
- 41 Lazarides E (1980) Intermediate filaments as mechanical integrators of cellular space. *Nature* 283:249-56
- 42 Buschmann MD, Hunziker EB, Kim YJ, Grodzinsky AJ (1996) Altered aggrecan synthesis correlates with cell and nucleus structure in statically compressed cartilage. *J Cell Sci* 109:499-508
- 43 Baum H (1974) Mitochondria and peroxisomes. in *The cell in medical science*, ed. F Beck & JB Lloyd. London, Academic Press:183-272
- 44 Pritchard JJ (1952) A cytochemical and histochemical study of bone and cartilage in the rat. *J Anat* 86:259-77
- 45 Sacerdotti C (1900) Ueber das Knorpelfett. *Virchows Arch path Anat Physiol* 159:152-72
- 46 Collins DH, Ghadially FN, Meachim G (1965) Intracellular lipids of cartilage. *Ann rheum Dis* 24:123-35
- 47 Hunziker EB (1999) Articular cartilage repair: are the intrinsic biological constraints undermining this process insuperable?. *Osteoarthritis and Cartilage* 7:15-28
- 48 Shapiro F, Koide S, Glimcher MJ (1993) Cell origin and differentiation in the repair of full -thickness defects of articular cartilage. *J Bone Joint Surg [Am]* 75-A:532-53
- 49 Gobbi A, Nunag P, Malinowski K (2005) Treatment of full thickness chondral lesions of the knee with microfracture in a group of athletes. *Knee Surg Sports Traumatol Arthrosc* 13:213-21
- 50 Mankin HJ (1962) Localization of tritiated thymidine in articular cartilage of rabbits. II. Repair in immature cartilage. *J Bone Jt Surg* 44A: 688-98
- 51 Lippmann M (1968) Glycosaminoglycans and cell division. in *Epithelial-mesenchymal interactions*, ed. R Fleishmajer & RE Billingham. Baltimore, Williams & Wilkins:208-29
- 52 Meachim G (1963) The effect of scarification on articular cartilage in the rabbit. *J Bone Jt Surg* 45B:150-61
- 53 Dustmann HO, Puhl W Krempien B (1974) Das Phanomen der Cluster im Arthroseknoepel. *Arch orthop Unfallchir* 79:321-33

- 54 Palmoski M, Brandt, K, Myers S, et al (1983) In vivo effect of aspirin on canine osteoarthritic cartilage. *Arthritis Rheum* 26:994-1001
- 55 Soong HK, Parkinson WC, Bafna S, Sulik GL, Huang SC (1990) Movements of cultured corneal epithelial cells and stromal fibroblasts in electric fields. *Invest Ophthalmol Vis Sci* 31:2278-82
- 56 Pullar C, Isseroff R, Nuccitelli R (2001) Cyclic AMP-Dependent Protein Kinase A Plays a Role in the Directed Migration of Human Keratinocytes in a DC Electric Field. *Cell Motility and the Cytoskeleton* 50:207-17
- 57 Finkelstein E, Chang W, Chao PHG, Gruber D, Minden A, Hung CT, Bulinski J (2003) Roles of microtubules, cell polarity and adhesion in electric-field-mediated motility of 3T3 fibroblasts. *Journal of Cell Science* 117:1533-45
- 58 Guilak F, Sah R, Setton L (1997) Physical Regulation of Cartilage Metabolism. in *Basic Orthopaedic Biomechanics*. Philadelphia, Lippincott-Raven:179-207
- 59 Chao PHG, Roy R, Mauck RL, Liu W, Valhmu W, Hung CT (2000) Chondrocyte Translocation Response to Direct Current Electric Fields. *Journal of Biomechanical Engineering* 122:261-7
- 60 Mauck R, Jezyk M, Valhmu W, Hung CT (1999, June 16-20) Chondrocyte Shape Change and Migratory Response to DC Electric Fields. presented at ASME Bioengineering Conference, Big Sky, Montana
- 61 Chao PG, Hakakha A, Nicoll SB, Hung CT (2002) Electric-Field Induced Migration and Orientation of Ligament Fibroblasts and Chondrocytes. *Trans Annu Meet Orthop Res Soc.* 48:582
- 62 Nishimura KY, Isseroff RR, Nuccitelli R (1996) Human Keratinocytes Migrate to the Negative Pole in Direct Current Electric Fields Comparable to Those Measured in Mammalian Wounds. *J Cell Sci* 109:199-207
- 63 Hinkle L, McCaig CD, Robinson KR (1981) The direction of growth of differentiating neurones and myoblasts from frog embryos in an applied electric field *J Physiol.* 314:121-35
- 64 Luther PW, Peng HB, Lin JJC (1983) Changes in cell shape and actin distribution induced by constant electric fields. *Nature* 303: 61-4
- 65 Lin J (1983) Changes in cell shape and actin distribution induced by constant electric fields. *Nature* 303:61-4
- 66 Farboud B, Nuccitelli R, Schwab I, Isseroff R (2000) DC Electric Fields Induce Rapid Directional Migration in Cultured Human Corneal Epithelial Cells. Academic Press
- 67 Xuefeng L, Kolega J (2002) Effects of Direct Current Electric Fields on Cell Migration and Actin Filament Distribution in Bovine Vascular Endothelial Cells. *Journal of Vascular Research* 39:391-404
- 68 Nuccitelli R, Erickson C (1983) Embryonic Cell Motility Can Be Guided by Physiological Electric Fields. *Exp Cell Res* 147:195-201
- 69 Onuma E, Hui S (1988) Electric Field-directed Cell Shape Changes, Displacement, and Cytoskeletal Reorganization are Calcium Dependent. *The Journal of Cell Biology* 106:2067-75
- 70 Cooper M, Schliwa M (1985) Electrical and Ionic Controls of Tissue Cell Locomotion in DC Electric Fields. *Journal of Neuroscience Research* 13:223-244

- 71 Cooper MS, Keller RE (1984) Perpendicular orientation and directional migration of amphibian neural crest cells in dc electric fields. *Proc Natl Acad Sci USA* 81:160-4
- 72 Jaffe LF (1977) Electrophoresis along cell membranes. *Nature*: 265 600-2
- 73 Jaffe LF, Nuccitelli R (1977) Electrical controlsof development *Annu Rev Biophys Bioeng* 6:445-76
- 74 Rogachefsky R, Altman R, Markov M, Cheung H (2004) Use of a Permanent Magnetic Field to Inhibit the Development of Canine Osteoarthritis. *Bioelectromagnetics* 25:260-70
- 75 Levin M, Ernst S (1997) Applied DC Magnetic Fields Cause Alterations in the Time of Cell Divisions and Developmental Abnormalities in Early Sea Urchin Embryos. *Bioelectromagnetics* 18:255-63
- 76 Albertini M, Accorsi A, Citterio B, Burattini S, Piacentini M, Uguccioni F, Piatti E (2003) Morphological and biochemical modifications induced by a static magnetic field on *Fusarium culmorum*. *Biochimie* 85:963-70
- 77 Chionna A, Dwikat M, Panzarini E, Tenuzzo B, Carla EC, Verri T, Pagliara P, Abbro L, Dini L (2003) Cell shape and plasma membrane alterations after static magnetic fields exposure. *European Journal of Histochemistry* 47:299-308
- 78 Chionna A, Tenuzzo B, Panzarini E, Dwikat M, Abbro L, Dini L (2004) Time Dependent Modifications of Hep G2 Cells During Exposure to Static Magnetic Fields. *Bioelectromagnetics* 26:275-86
- 79 Fanelli C, Coppola S, Barone R, Colussi C, Gualandi G, Volpe P, Ghibelli L (1999) Magnetic fields increase cell survival by inhibiting apoptosis via modulation of Ca²⁺ influx. *The FASEB Journal* 13:95-102
- 80 Rosen AD (2003) Meachanism of action of moderate-intensity static magnetic fields on biological systems. *Cell Biochem Biophys* 39:163-73
- 81 Ohata R, Tomita N, Ikada Y (2004) Effect of a static magnetic field on ion transport in a cellulose membrane. *Journal of Colloid and Interface Science* 270:413-6
- 82 Higashitani K, Oshitani J (1998) Magnetic effects on thickness of adsorbed layer in aqueous solutions evaluated directly by atomic force microscope. *Journal of Colloid and Interface Science* 204: 363-368
- 83 Rosen A (1993) Membrane Response to Static Magnetic Fields: Effect of Exposure Duration. *Biochim Biophys Acta* 1148:317-20
- 84 Rosen A (2003) Effect of a 125mT Static Magnetic Field on the Kinetics of Voltage Activated Na⁺ Channels in GH3 Cells. *Bioelectromagnetics* 24:517-23
- 85 Maret G, Dransfield K (1977) Macromolecules and membranes in high magnetic fields. *Physica* 86-88B:1077-83
- 86 Rosen AD, Lubowsky J (1990) Modification of spontaneous unit discharge in the lateral geniculate body by a magnetic field. *Exp Neurol* 108:261-5
- 87 Brighton CT, Unger AS, Stambough JL (1984) In vitro growth of bovine articular cartilage chondrocytes in various capacitively coupled electrical fields. *J Orthop Res* 2:15-22
- 88 Wang W, Wang Z, Zhang G, Clark C, Brighton C (2004) Up-regulation of Chondrocyte Matrix Genes and Products by Electric Fields. *Clinical Orthopaedics & Related Research* 427S:163-73

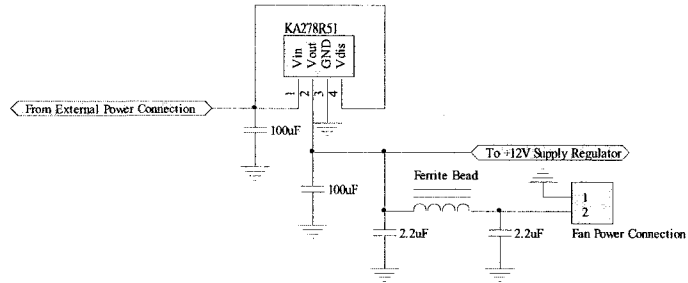
- 89 Rosenspire A, Kindzelskii A, Petty H (2001) Pulsed DC electric fields couple to natural NAD(P)H oscillations in HT-1080 fibrosarcoma cells. *Journal of Cell Science* 114:1515-20
- 90 Bassett CAL, Pilla AA, Pawluk RJ (1977) A Non-Operative Salvage of Surgically-Resistant Pseudarthroses and Non-Unions by Pulsing Electromagnetic Fields. *Clinical Orthopaedics and Related Research* 124:128-43
- 91 Chang W, Chen LT, Sun JS, Lin FH (2004) Effect of Pulse Burst Electromagnetic Field Stimulation on Osteoblast Cell Activities. *Bioelectromagnetics* 25:457-65
- 92 Sollazzo V, Traina G, DeMattei M, Pellati A, Pezzetti F, Caruso A (1997) Responses of Human MG-63 Osteosarcoma Cell Line and Human Osteoblast-Like Cells to Pulsed Electromagnetic Fields. *Bioelectromagnetics* 18:541-7
- 93 Diniz P, Shomura K, Soejima K, Ito G (2002) Effects of Pulsed Electromagnetic Field (PEMF) Stimulation on Bone Tissue Like Formation Are Dependent on the Maturation Stages of the Osteoblasts. *Bioelectromagnetics* 23:398-405
- 94 Chang K, Chang W (2003) Pulsed Electromagnetic Fields Prevent Osteoporosis in an Ovariectomized Female Rat Model: A Prostaglandin E2-Associated Process. *Bioelectromagnetics* 24:189-98
- 95 Chang K, Chang W, Shih C (2003) Effects of Different Intensities of Extremely Low Frequency Pulsed Electromagnetic Fields on Formation of Osteoclast-Like Cells. *Bioelectromagnetics* 24:431-9
- 96 Pawluk W, Turk Z, Fischer G, Kobinger W (2002, June 25-27) Treatment of Osteoarthritis with a new broadband PEMF Signal. presented at the Bioelectromagnetic Society Meeting Quebec, Canada
- 97 Thamsborg G, Florescu A, Oturai P, Fallentin E, Tritsari K, Dissing S (2005) Treatment of knee osteoarthritis with pulsed electromagnetic fields: a randomized, double-blind, placebo-controlled study. *Osteoarthritis and Cartilage* 13:575-81
- 98 Trock D, Bollet A, Dyer R, Fielding L, Miner W, Markoll R (1993) A Double-Blind Trial of the Clinical Effects of Pulsed Electromagnetic Fields in Osteoarthritis. *Journal of Rheumatology* 20:456-60
- 99 Nicolakis P, Kollmitzer J, Crevenna R, Bittner C, Erdogmus C, Nicolakis J (2002) Pulsed magnetic field therapy for osteoarthritis of the knee – a double-blind sham-controlled trial. *Wien Klin Wochenshr* 114:678-84
- 100 Fioravanti A, Nerucci F, Collodel G, Markoll R, Marcolongo R (2002) Biochemical and morphological study of human articular chondrocytes cultivated in the presence of pulsed signal therapy. *Ann Rheum Dis* 61:1032-3
- 101 Markoll R, Nerucci F, Fioravanti A, Tofi C, Righeschi K, Marcolongo R PST Enhances Proteoglycans Concentrations in Human Chondrocyte Cultures
- 102 Ciombor D, Aaron R, Wang S, Simon B (2003) Modification of osteoarthritis by pulsed electromagnetic field - a morphological study. *Osteoarthritis and Cartilage* 11:455-62
- 103 Fini M, Giavaresi G, Torricelli P, Cavani F, Setti S, Cane V, Giardino R (2005) Pulsed electromagnetic fields reduce knee osteoarthritic lesion progression in the aged Dunkin Hartley guinea pig. *Journal of Orthopaedic Research* 23:899-908
- 104 Ciombor D, Lester G, Aaron R, Neame R, Caterson B (2002) Low frequency EMF regulates chondrocyte differentiation and expression of matrix proteins. *Journal of Orthopaedic Research* 20:40-50

- 105 Pezzetti F, De Mattei M, Caruso A, Cadossi R, Zucchini P, Carinci F, Traina GC, Sollazzo V (1999) Effects of Pulsed Electromagnetic Fields on Human Chondrocytes: An In Vitro Study. *Calcified Tissue International* 65:396-401
- 106 Elliott JP, Smith RL, Block CA (1988) Time-Varying Magnetic Fields: Effects of Orientation on Chondrocyte Proliferation. *Journal of Orthopaedic Research* 6:259-64
- 107 Hiraki Y, Endo N, Takigawa M, Asada A, Takahashi H, Suzuki F (1987) Enhanced responsiveness to parathyroid hormone and induction of functional differentiation of cultured rabbit costal chondrocytes by a pulsed electromagnetic field. *Biochimica et Biophysica Acta* 931:94-100
- 108 Mattei M, Pellati A, Pasello M, Ongaro A, Setti Stefania, Massari L, Gemmati D, Caruso A (2004) Effects of physical stimulation with electromagnetic field and insulin growth factor-I treatment on proteoglycan synthesis of bovine articular cartilage. *Osteoarthritis and Cartilage* 12:793-800
- 109 Bonaventure J, Kadhon N, Cohen-Solal L, Ng KH, Bourguignon J, Lasselin C, et al. (1994) Reexpression of cartilage-specific genes by dedifferentiated human articular chondrocytes cultured in alginate beads. *Exp Cell Res* 212:97-104
- 110 Manni V, Lisi A, Pozzi D, Reiti S, Serafino A, Guiliani L, Grimaldi S (2002) Effects of Extremely Flow Frequency (50Hz) Magnetic Field on Morphological and Biochemical Properties of Human Keratinocytes. *Bioelectromagnetics* 23:298-305
- 111 Bersani F, Marinelli F, Ognibene A, Matteucci A, Cecchi S, Santi S, Squarzone S, Maraldi N (1997) Intramembrane Protein Distribution in Cell Cultures is Affected by 50Hz Pulsed Magnetic Fields. *Bioelectromagnetics* 18:463-9
- 112 Blumenthal N, Ricci J, Breger L, Zychlinsky A, Solomon H, Chen GG, Kuznetsov D, Dorfman R (1997) Effects of Low-Intensity AC and/or DC Electromagnetic Fields on Cell Attachment and Induction of Apoptosis. *Bioelectromagnetics* 18:264-72
- 113 Tenforde TS (1996) Biological Interaction of Extremely Low Frequency Electromagnetic Fields. in *Biological Effects of Magnetic and Electromagnetic Fields*, ed. S Ueno. New York, Plenum Press:23-36.
- 114 Markov M, Colbert P (2001) Magnetic and electromagnetic field therapy. *Journal of Back and Musculoskeletal Rehabilitation* 15:17-29
- 115 Blank M, Goodman R (1997) Do Electromagnetic Fields Interact Directly With DNA?. *Bioelectromagnetics* 18:111-5
- 116 Weaver JC, Astumian RD (1990) The response of living cells to very weak electric fields: The thermal noise limit. *Science* 247:459-62
- 117 Aaron R, Boyan B, Ciombor D, Schwartz Z, Simon B (2004) Stimulation of Growth Factor Synthesis by Electric and Electromagnetic Fields. *Clin Orthop* 419:30-7
- 118 Polk C (1996) Physical Mechanisms for Biological Effects of Low Field Intensity ELF Magnetic Fields. in *Biological Effects of Magnetic and Electromagnetic Fields*, ed. S Ueno. New York, Plenum Press:63-84
- 119 Adey WR (1996) A Growing Scientific Consensus on the Cell and Molecular Biology Mediating: Interactions with Environmental Electromagnetic Fields. in *Biological Effects of Magnetic and Electromagnetic Fields*, ed. S Ueno. New York, Plenum Press:45-62

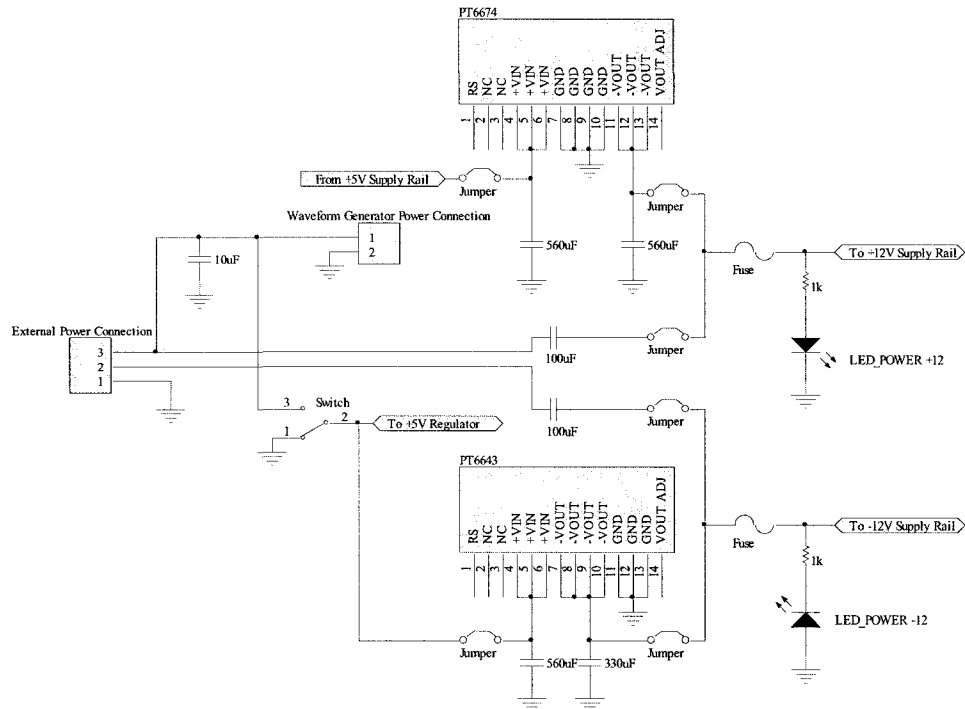
- 120 Luben RA, Hyunh D, Weinshank RL, Smith LE (1990) Molecular cloning of candidate sequences for the mouse osteoblast parathyroid hormone receptor. in Calcium Regulation and Bone Metabolism, ed. DV Cohn, FH Glorieux & TJ Martin. Amsterdam, Elsevier:39-44
- 121 Pilla AA (1972) Electrochemication information and energy transfer in vivo. Proc. 7th IECEC, Washington DC. American Chemical Society:761-4
- 122 Pilla AA (1974) Electrochemical information transfer at living cell membranes. Ann NY Acad Sci 238:149-70
- 123 Cleary SF (1994) Biophysical Aspects of Electromagnetic Field Effects on Mammalian Cells. in On the Nature of Electromagnetic Field Interactions with Biological Systems, ed. AH Frey. Austin, Armstrong Printing Co:29-42
- 124 Lednev VV (1991) Possible mechanism for influence of weak magnetic fields on biosystems. Bioelectromagnetics 12:71-5
- 125 Lednev VV (1993) Possible mechanism for the effect of weak magnetic fields on biological systems: Correction of the basic expression and its consequences. in Electricity and Magnetism in Biology and Medicine, ed. M Blank. San Francisco, San Francisco Press:550-2
- 126 Liboff RA (1985) Cyclotron resonance in membrane transport. in Interaction between Electromagnetic Fields and Cells, ed. Chiaberera, Nicolini & Schwan. London, Plenum:281-96
- 127 Liboff RA, McLeod BR (1988) Kinetics of Channelized Membrane Ions in Magnetic Fields. Bioelectromagnetics 9:39-51
- 128 Lednev VV (1994) Interference with the Vibrational Energy Sublevels of Ions Bound in Calcium-Binding Proteins as the Basis for the Interaction of Weak Magnetic Fields with Biological Systems. in On the Nature of Electromagnetic Field Interactions with Biological Systems, ed. AH Frey. Austin, Armstrong Printing Co:59-72
- 129 Durney CH, Rushforth CK, Anderson AA (1988) Resonant dc-ac magnetic fields: calculated response. Bioelectromagnetics 9:315-36
- 130 Blanchard JP, Blackman CF (1994) A Model of Magnetic Field Effects on Biological Systems with Confirming Data from a Cell Culture Preparation, in On the Nature of Electromagnetic Field Interactions with Biological Systems, ed. AH Frey. Austin, Armstrong Printing Co:43-58
- 131 Blanchard JP, Blackman CF (1994) Clarification and application of an ion parametric resonance model for magnetic field interactions with biological systems. Bioelectromagnetics 15:217-38
- 132 Barueus Koch CLM, Sommarin M, Persson BRR, Salford LF, Eberhardt JL (2003) Interaction Between Weak Low Frequency Magnetic Fields and Cell Membranes. Bioelectromagnetics 24:395-402
- 133 Smith S, McLeod B, Liboff A, Cooksey K (1987) Calcium cyclotron resonance and diatom mobility. Bioelectromagnetics 8: 215-27
- 134 Grande DA, Magee FP, Weinstein AM, McLeod BR (1991) The Effect of Low-Energy Combined AC and DC Magnetic Fields on Articular Cartilage Metabolism. Annals of the New York Academy of Sciences 635:404-7

- 135 Jahns ME, Lou E, Durdle NG, Bagnall K, Raso VJ, Cinats D, Barley RDC, Cinats J, Jomha NM (2007) The effect of pulsed electromagnetic fields on chondrocyte morphology. *Med Bio Eng Comput* 45:917-25
- 136 Czernaboj J (2006) The effects of low levels of ethanol on neural crest cell behaviour. MSc Thesis UofA
- 137 Katz B, Miledi R (1972) The statistical nature of the acetylcholine potential and its molecular components. *J Physiol* 224:665–699
- 138 Buckley IK (1981) Fine-structural and related aspects of nonmuscle-cell motility. *Cell Muscle Motil* 1:135-203
- 139 Tang Y, Tian F, Lou E, Bagnall K, Cinats F, Jomha N, Raso J Kwok D (2005, June 13-15) A microfluidic model for the growth and migration of chondrocyte under pulsed electromagnetic field. presented at draft proceedings of ICMM. Toronto, Canada
- 140 Cheng DK (1992) *Field and wave electromagnetics*, 2nd edition, New York, Addison-Wesley:234-43
- 141 Smythe WR (1968) *Static and dynamic electricity*. 3rd edition, New York, McGraw-Hill:290-91

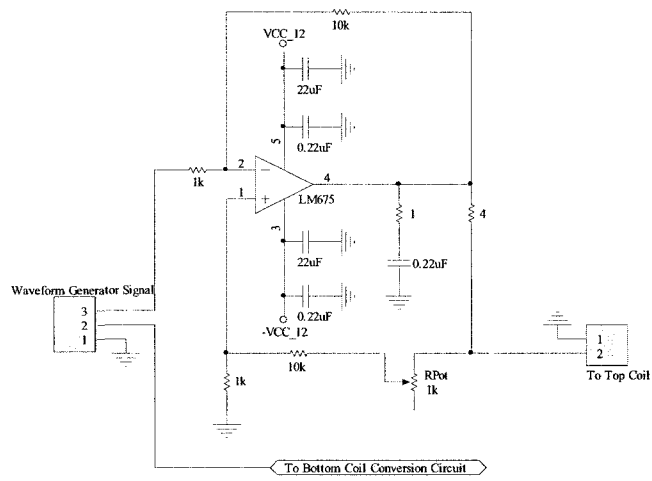
Appendix A: Coil Driver Schematics



Coil Driver +5V Power Regulation Circuit

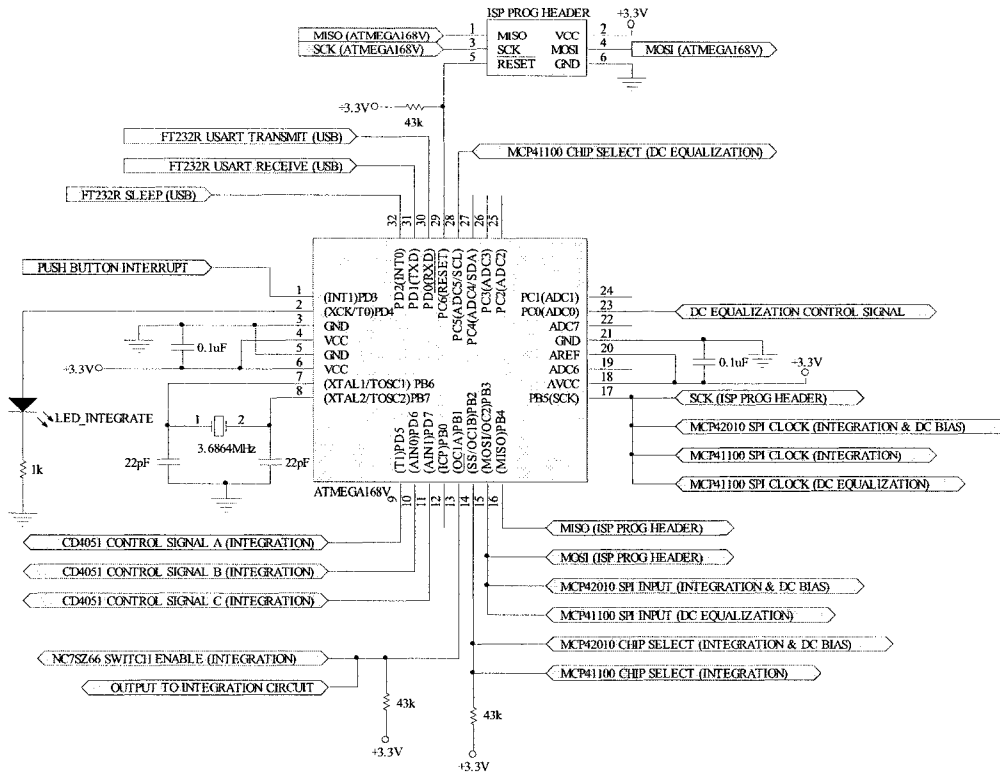


Coil Driver ±12V Power Regulation Circuit

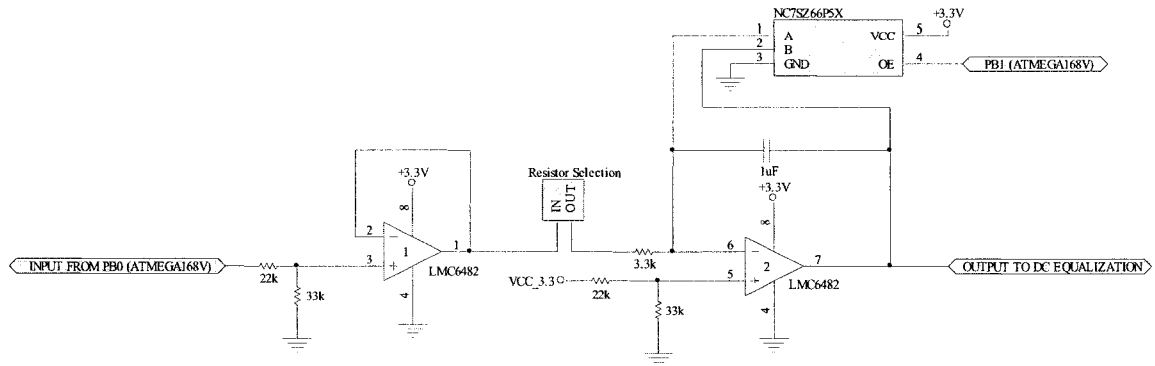


Coil Driver Voltage-to-Current Conversion Circuit

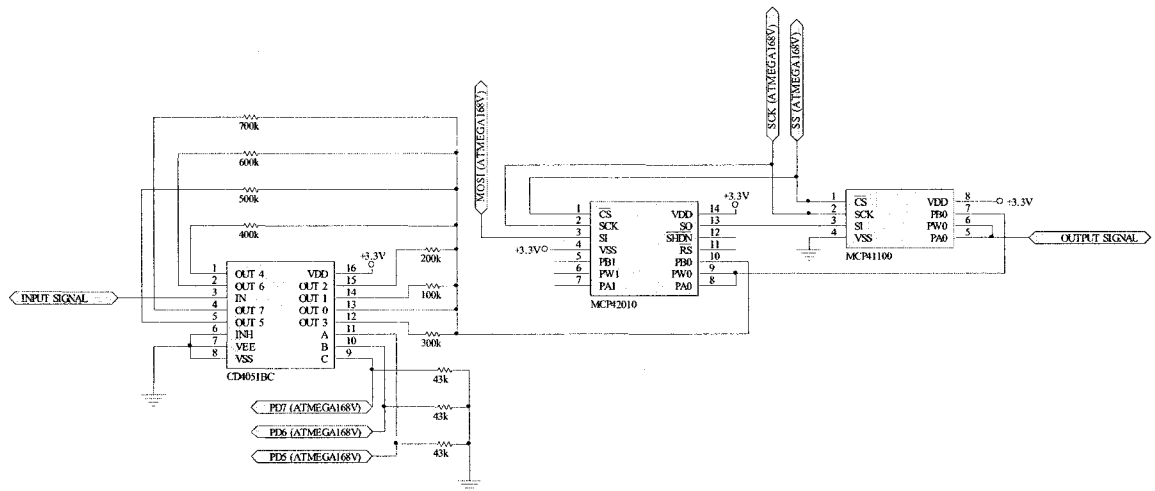
Appendix B: Programmable Waveform Generator Schematics



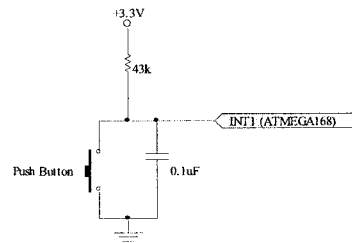
Programmable Waveform Generator Microcontroller Interface



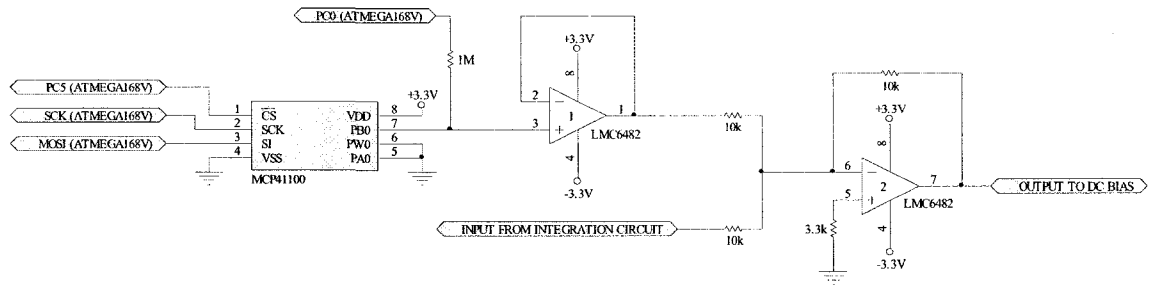
Programmable Waveform Generator AC Signal Generation Circuit



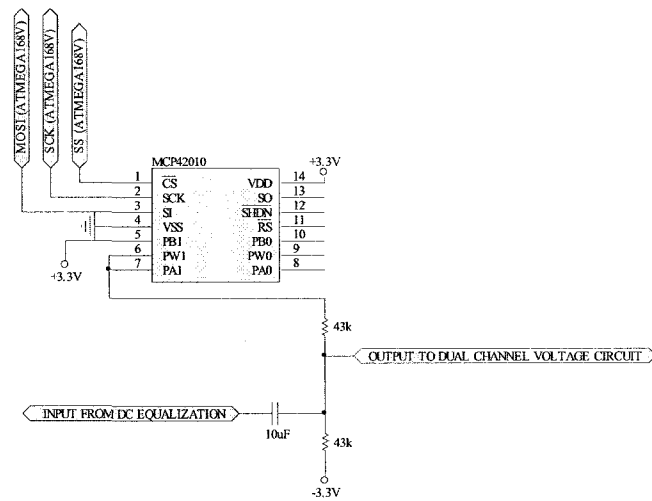
Programmable Waveform Generator AC Signal Generation Resistance Selection Circuit



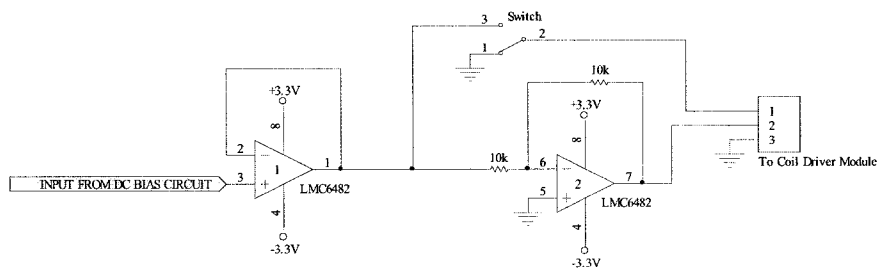
Programmable Waveform Generator Push Button Interrupt



Programmable Waveform Generator DC Equalization Circuit

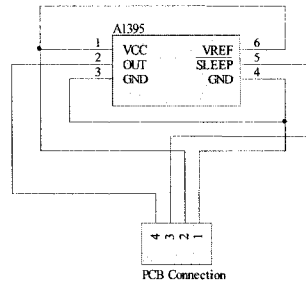


Programmable Waveform Generator DC Bias Circuit

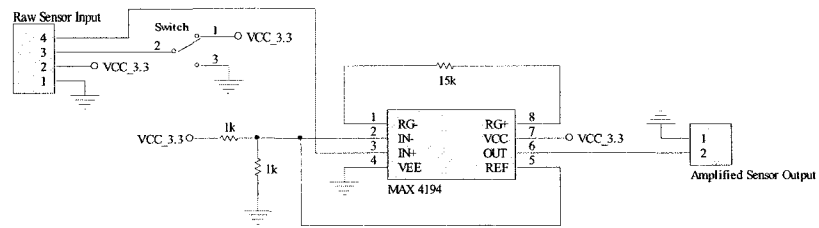


Programmable Waveform Generator Dual Channel Voltage Output Circuit

Appendix C: Magnetic Field Sensor Schematics



External Magnetic Field Sensor



Magnetic Field Sensor Interface onboard the Programmable Waveform Generator